

ADA 041493

BEST AVAILABLE COPY

Unclassified

SECURITY CLASSIFICATION OF THIS PAGE (When Data Entered)

(19) REPORT DOCUMENTATION PAGE		READ INSTRUCTIONS BEFORE COMPLETING FORM
1. REPORT NUMBER 18 AFAL TR-76-266	2. GOVT ACCESSION NO.	3. RECIPIENT'S CATALOG NUMBER
4. TITLE (and Subtitle) 6 A Technique for Determining Radar Target Scintillation (GLINT)		5. TYPE OF REPORT & PERIOD COVERED Final Technical Report, Jan. 1 1975 - July 31, 1976
6. AUTHOR(s) 10 D. G. Bodnar		7. PERFORMING ORG. REPORT NUMBER 14 GIT A-1704
8. CONTRACT OR GRANT NUMBER(s) 15 F33615-75-C-1069		9. PROGRAM ELEMENT, PROJECT, TASK AREA & WORK UNIT NUMBERS 16 7633 13 18
10. CONTROLLING OFFICE NAME AND ADDRESS 11 Air Force Avionics Laboratory (WRP) Air Force Systems Command Wright-Patterson AFB, Ohio 45433		11. REPORT DATE 17 May 1977
12. NUMBER OF PAGES 18 129		13. SECURITY CLASS. (if this report) Unclassified
14. MONITORING AGENCY NAME & ADDRESS (if different from Controlling Office)		15. DECLASSIFICATION/DOWNGRADING SCHEDULE 19a N/A

16. DISTRIBUTION STATEMENT (of this Report)

Approved for public release; distribution unlimited.

17. DISTRIBUTION STATEMENT (of the abstract entered in Block 20, if different from Report)

⑨ Final technical rept. 1 Jan 75-31 Jul 76

18. SUPPLEMENTARY NOTES

62204F

19. KEY WORDS (Continue on reverse side if necessary and identify by block number)

Near Zone	Scattering
Clint	Nonuniform Illumination
Radar Cross-Section	Nonplanar Illumination
Scintillation	Plane Wave Expansion

Modal Expansion Geometrical Theory of Diffraction

80 ABSTRACT (Continue on reverse side if necessary and identify by block number)

A technique is described for obtaining near-zone as well as far-zone GLINT data on aerospace targets based on near-field measurements of the target. A modal expansion in terms of plane wave functions is used to represent the fields scattered by the target. A similar representation is made for the tracker antenna of interest based on measurements of its near fields. The antenna and scattering characteristics are combined using equations presented in the report to predict the received signal at virtually any distance from

DD FORM 1 JAN 73 1473 EDITION OF 1 NOV 65 IS OBSOLETE

SECURITY CLASSIFICATION OF THIS PAGE (When Data Entered)

Unclassified

(over)

153 850

Unclassified

SECURITY CLASSIFICATION OF THIS PAGE(When Data Entered)

20. ABSTRACT (Cont.)

the target between the measurement plane and infinity. The technique is demonstrated on an F-105 model aircraft and a single plane monopulse tracking antenna at X-band. Excellent agreement between measured and predicted error signal is presented for various fly-bys of the monopulse antenna past the target. Also presented is a new characterization technique for near-field probes which simplifies the process of obtaining their plane wave spectrum.

X

Unclassified

SECURITY CLASSIFICATION OF THIS PAGE(When Data Entered)

AMENDMENT 07	
STL	DATA CENTER
DDO	DATA CENTER
UNARMED	
JUSTIFICATION	
DT... DISTRIBUTION/AVAILABILITY CODES	
INFO.	AVAIL. AND/OR SPECIAL
A	

FOREWORD

The research of this program was carried out by personnel of the Advanced Technical Area of the Applied Engineering Laboratory, Engineering Experiment Station, Georgia Institute of Technology, Atlanta, Georgia 30332, with Dr. D. G. Bodnar serving as Project Director. The program, which was sponsored by the Air Force Avionics Laboratory, Air Force Systems Command, Wright-Patterson Air Force Base, Ohio 45433, under Contract No. F33615-75-C-1069, Project No. 7633, was designated by Georgia Tech as Project A-1704. This technical report covers the work which was performed between January 1, 1975 and July 31, 1976.

The author of this report is Dr. D. G. Bodnar. The work performed was made possible by the combined efforts of many people at the Air Force Avionics Laboratory and at Georgia Tech. Specifically, the author would like to thank Dr. C. A. Mentzer, Project Engineer, Mr. R. A. Simons, who served first as Project Engineer and then as Acting Technical Manager of AFAL/WRP-3, and Mr. W. F. Bahret, who served first as Technical Manager of WRP-3 and then as Acting Chief of WRP. Dr. J. L. Edwards served as Technical Manager at Georgia Tech. Special thanks go to Mr. W. J. Storey, who performed the measurements reported in this document and to Mr. E. C. Burdette, who performed the work reported in the Appendix.

D D C
REPORT
JUL 11 1977
RESULTS
D.

TABLE OF CONTENTS

<u>Section</u>		<u>Page</u>
I	INTRODUCTION.	1
II	PLANE WAVE SPECTRUM REPRESENTATION OF FIELDS.	4
III	CORRECTION FOR PROBE EFFECTS.	7
IV	A CHARACTERIZATION TECHNIQUE FOR NEAR-FIELD PROBES.	20
	A. Description of Technique.	20
	B. Discussion of Results	23
V	GLINT MEASUREMENTS.	63
	A. Tracker Measurements.	65
	B. Target Measurements	65
	C. Data Reduction Techniques	105
VI	CONCLUSIONS AND RECOMMENDATIONS	109
	APPENDIX.	112
	REFERENCES.	129

LIST OF FIGURES

<u>Figure</u>	<u>Page</u>
1. Probe measurement of target or antenna.	8
2. Location of points in k-space used in characterizing probe spectrum.	21
3. Photograph of X-band probe horns PX-6 on left and PX-5 on right	24
4. Amplitude of vertical (parallel) component of measured voltage obtained using one PX-5 as the probe and another PX-5 as a transmitter.	25
5. Amplitude of horizontal (cross) component of measured voltage obtained using one PX-5 as the probe and another PX-5 as a transmitter.	26
6. Amplitude of vertical (parallel) component of measured plane wave spectrum obtained using one PX-5 as the probe and another PX-5 as a transmitter	27
7. Phase of vertical (parallel) component of measured plane wave spectrum obtained using one PX-5 as the probe and another PX-5 as a transmitter	28
8. Amplitude of horizontal (cross) component of measured plane wave spectrum obtained using one PX-5 as the probe and another PX-5 as a transmitter	29
9. Phase of horizontal (cross) component of measured plane wave spectrum obtained using one PX-5 as the probe and another PX-5 as a transmitter	30
10. Amplitude of x-component of plane wave spectrum for Probe PX-5 at 9 GHz	31
11. Phase of x-component of plane wave spectrum for Probe PX-5 at 9 GHz.	32
12. Amplitude of y-component of plane wave spectrum for Probe PX-5 at 9 GHz	33
13. Phase of y-component of plane wave spectrum for Probe PX-5 at 9 GHz.	34
14. Amplitude of predicted vertical (parallel) component of measured plane wave spectrum for Probe PX-5 measuring another another PX-5 that is transmitting	36

LIST OF FIGURES (cont.)

<u>Figure</u>	<u>Page</u>
15. Phase of predicted vertical (parallel) component of measured plane wave spectrum for probe PX-5 measuring another PX-5 that is transmitting	37
16. Amplitude of predicted horizontal (cross) component of measured plane wave spectrum for probe PX-5 measuring another PX-5 that is transmitting	38
17. Phase of predicted horizontal (cross) component of measured plane wave spectrum for probe PX-5 measuring another PX-5 that is transmitting	39
18. Amplitude of vertical (parallel) component of measured voltage obtained using one PX-6 as the probe and another PX-6 as a transmitter	40
19. Amplitude of horizontal (cross) component of measured voltage obtained using one PX-6 as the probe and another PX-6 as a transmitter	41
20. Amplitude of vertical (parallel) component of measured plane wave spectrum obtained using one PX-6 as the probe and another PX-6 as a transmitter	42
21. Phase of vertical (parallel) component of measured plane wave spectrum obtained using one PX-6 as the probe and another PX-6 as a transmitter	43
22. Amplitude of horizontal (cross) component of measured plane wave spectrum obtained using one PX-6 as the probe and another PX-6 as a transmitter	44
23. Phase of horizontal (cross) component of measured plane wave spectrum obtained using one PX-6 as the probe and another PX-6 as a transmitter	45
24. Amplitude of x-component of plane wave spectrum for probe PX-6 at 9 GHz	46
25. Phase of x-component of plane wave spectrum for probe PX-6 at 9 GHz.	47
26. Amplitude of y-component of plane wave spectrum for probe PX-6 at 9 GHz	48
27. Phase of y-component of plane wave spectrum for probe PX-6 at 9 GHz.	49

LIST OF FIGURES (cont.)

<u>Figure</u>		<u>Page</u>
28. Amplitude of predicted vertical (parallel) component of measured plane wave spectrum for probe PX-6 measuring another PX-6 that is transmitting.		50
29. Phase of predicted vertical (parallel) component of measured plane wave spectrum for probe PX-6 measuring another PX-6 that is transmitting		51
30. Amplitude of predicted horizontal (cross) component of measured plane wave spectrum for probe PX-6 measuring another PX-6 that is transmitting.		52
31. Phase of predicted horizontal (cross) component of measured plane wave spectrum for probe PX-6 measuring another PX-6 that is transmitting		53
32. Amplitude of vertical (parallel) component of measured plane wave spectrum obtained using PX-6 as the probe and PX-5 as a transmitter.		54
33. Phase of vertical (parallel) component of measured plane wave spectrum obtained using PX-6 as the probe and PX-5 as a transmitter.		55
34. Amplitude of horizontal (cross) component of measured plane wave spectrum obtained using PX-6 as the probe and PX-5 as a transmitter.		56
35. Phase of horizontal (cross) component of measured plane wave spectrum obtained using PX-6 as the probe and PX-5 as a transmitter.		57
36. Amplitude of predicted vertical (parallel) component of measured plane wave spectrum for probe PX-6 measuring PX-5 as a transmitter		58
37. Phase of predicted vertical (parallel) component of measured plane wave spectrum for probe PX-6 measuring PX-5 as a transmitter.		59
38. Amplitude of predicted horizontal (cross) component of measured plane wave spectrum for probe PX-6 measuring PX-5 as a transmitter		60
39. Phase of predicted horizontal (cross) component of measured plane wave spectrum for probe PX-6 measuring PX-5 as a transmitter.		61

LIST OF FIGURES (cont.)

<u>Figure</u>	<u>Page</u>
40. Geometry for flyby measurements at 9.0 GHz of 1/33 scale F-105 model aircraft.	64
41. Amplitude of vertical (parallel) component of measured voltage for sum channel of one-foot tracker at 9 GHz using probe PX-5.	66
42. Amplitude of horizontal (cross) component of measured voltage for sum channel of one-foot tracker at 9 GHz using probe PX-5.	67
43. Amplitude of vertical (parallel) component of measured voltage for difference channel of one-foot tracker at 9 GHz using probe PX-5.	68
44. Amplitude of horizontal (cross) component of measured voltage for difference channel of one-foot tracker at 9 GHz using probe PX-5.	69
45. Amplitude of vertical (parallel) component of measured plane wave spectrum for sum channel of one-foot tracker at 9 GHz using probe PX-5.	70
46. Amplitude of horizontal (cross) component of measured plane wave spectrum for sum channel of one-foot tracker at 9 GHz using probe PX-5.	71
47. Amplitude of vertical (parallel) component of measured plane wave spectrum for difference channel of one-foot tracker at 9 GHz using probe PX-5.	72
48. Amplitude of horizontal (cross) component of measured plane wave spectrum for difference channel of one-foot tracker at 9 GHz using probe PX-5	73
49. Amplitude of x-component of plane wave spectrum for sum channel of one-foot tracker at 9 GHz.	74
50. Amplitude of y-component of plane wave spectrum for sum channel of one-foot tracker at 9 GHz.	75
51. Amplitude of x-component of plane wave spectrum for difference channel of one-foot tracker at 9 GHz	76
52. Amplitude of y-component of plane wave spectrum for difference channel of one-foot tracker at 9 GHz	77
53. Measured amplitude of parallel-polarized component of the scattered electric field from F-105 model at 9.0 GHz using probe PX-5.	79

LIST OF FIGURES (cont.)

<u>Figure</u>	<u>Page</u>
54. Measured amplitude of cross-polarized component of the scattered electric field from F-105 model at 9.0 GHz using probe PX-5	80
55. Amplitude of x-component of scattered plane wave spectrum from F-105 model at 9.0 GHz	81
56. Phase of x-component of scattered plane wave spectrum from F-105 model at 9.0 GHz	82
57. Amplitude of y-component of scattered plane wave spectrum from F-105 model at 9.0 GHz	83
58. Phase of y-component of scattered plane wave spectrum from F-105 model at 9.0 GHz	84
59. Comparison of measured and computed signal received by sum channel along line $y = -6$ inches on $z = 44.5$ inch plane for parallel polarization	86
60. Comparison of measured and computed signal received by sum channel along line $y = 0$ inches on $z = 44.5$ inch plane for parallel polarization	87
61. Comparison of measured and computed signal received by sum channel along line $y = 0$ inches on $z = 54.5$ inch plane for parallel polarization	88
62. Comparison of measured and computed signal received by sum channel along line $y = 6$ inches on $z = 54.5$ inch plane for parallel polarization	89
63. Comparison of measured and computed signal received by difference channel along line $y = -6$ inches on $z = 44.5$ inch plane for parallel polarization	90
64. Comparison of measured and computed signal received by difference channel along line $y = 0$ inches on $z = 44.5$ inch plane for parallel polarization	91
65. Comparison of measured and computed signal received by difference channel along line $y = 0$ inches on $z = 54.5$ inch plane for parallel polarization	92
66. Comparison of measured and computed signal received by difference channel along line $y = 6$ inches on $z = 54.5$ inch plane for parallel polarization	93

LIST OF FIGURES (cont.)

<u>Figure</u>	<u>Page</u>
67. Comparison of measured and computed signal received by sum channel along line $y = 0$ inches on $z = 44.5$ inch plane for cross polarization	94
68. Comparison of measured and computed signal received by difference channel along line $y = -6$ inches on $z = 54.5$ inch plane for cross polarization.	95
69. Measured and computed ratio of difference channel to sum channel along line $y = -6$ inches on $z = 44.5$ inch plane for parallel polarization.	97
70. Measured and computed ratio of difference channel to sum channel along line $y = 0$ inches on $z = 44.5$ inch plane for parallel polarization.	98
71. Measured and computed ratio of difference channel to sum channel along line $y = 6$ inches on $z = 44.5$ inch plane for parallel polarization.	99
72. Measured and computed ratio of difference channel to sum channel along line $y = -6$ inches on $z = 54.5$ inch plane for parallel polarization.	100
73. Measured and computed ratio of difference channel to sum channel along line $y = 0$ inches on $z = 54.5$ inch plane for parallel polarization.	101
74. Measured and computed ratio of difference channel to sum channel along line $y = 6$ inches on $z = 54.5$ inch plane for parallel polarization.	102
75. Calculated difference channel to sum channel ratio for parallel polarization along the vertical line $x=0$ inches on the $z = 44.5$ inch plane	103
76. Calculated difference channel to sum channel ratio for parallel polarization along the vertical line $x=0$ inches on the $z = 54.5$ inch plane	104
77. Computed phase of error signal Δ/Σ for parallel polarization for F-105 model as seen by monopulse tracker at $z = 44.5$ inches	106
78. Computed phase of error signal Δ/Σ for parallel polarization for F-105 model as seen by monopulse tracker at $z = 54.5$ inches	107

LIST OF FIGURES (cont.)

<u>Figure</u>	<u>Page</u>
79. Diagram of the relation between the near-field sidelobe location x_c , the lobe 3-dB width ΔX , and the sample spacing δX	114
80. Location of measurement plane ($z = z_0$) and computed plane ($z = z_1$) with respect to the scattering structure	116
81. Location of center of the region of interest.	117
82. Location of eight wavelength square aperture in the measurement area and its respective illumination function . .	118
83. Comparison of the calculated near field of a uniformly illuminated 8-wavelength square aperture using a 16 x 16 low-pass filtered and a 64 x 16 unfiltered plane wave spectrum at a near-field distance of 6.44 wavelengths	120
84. Comparison of the calculated near field of a uniformly illuminated 8-wavelength square aperture using an 8 x 8 low-pass filtered and a 64 x 64 unfiltered plane wave spectrum at a near field distance of 6.44 wavelengths	121
85. Comparison of the calculated near field of a uniformly illuminated 8-wavelength square aperture using a 4 x 4 low-pass filtered and a 64 x 64 unfiltered plane wave spectrum at a near-field distance of 6.44 wavelengths	122
86. Comparison of the calculated near field of a uniformly illuminated 8-wavelength square aperture using an 8 x 8 low-pass filtered and a 32 x 32 unfiltered plane wave spectrum at a near-field distance of 3.22 wavelengths	124
87. Comparison of the calculated near field of a uniformly illuminated 8-wavelength square aperture using a 4 x 4 low-pass filtered and a 32 x 32 unfiltered plane wave spectrum at a near-field distance of 3.22 wavelengths	125
88. (a) Illustration of path used for near-field "flyby" calculations at a measurement distance of 6.44λ (b) Bandpass filtered wavenumber region of spectral data used for calculation of 1st sidelobe	126
89. Comparison of the calculated near field of a uniformly illuminated 8-wavelength square aperture using a 16 x 16 bandpass filtered and a 64 x 64 unfiltered plane wave spectrum. The 16 x 16 bandpass filtered spectrum is located at the first sidelobe region and the near-field distance is 6.44 wavelengths.	127

LIST OF FIGURES (cont.)

<u>Figure</u>	<u>Page</u>
90. Comparison of the calculated near field of a uniformly illuminated 8-wavelength square aperture using an 8 x 8 bandpass filtered and a 64 x 64 unfiltered plane wave spectrum. The 8 x 8 bandpass filtered spectrum is located at the first sidelobe region and the near-field distance is 6.44 wavelengths.	128

SECTION I

INTRODUCTION

The objective of this program was to define, develop, and demonstrate a generalized technique for obtaining realistic GLINT data on aerospace model targets. This technique, while of a general nature, is vital to the design of homing systems, proximity fuses, and countermeasures against such systems.

The problem of interest concerns an aerospace target being illuminated by a transmitter which may be on a missile or on the ground. This illumination signal produces a reflected field from the target. Interference effects occurring between various reflection points on the target produce a scattering pattern in space. In the far-field, these interference effects do not vary significantly with range. Thus, the scattering pattern is not range dependent. In the near-zone, however, these interference effects do vary with range. It is impossible to predict from far-zone measurements what the near-zone field will look like. Thus the near-zone problem is much more complex than the far-zone case because of the nonuniform and nonplanar fields involved. The near-zone radar cross-section (NZRCS) depends on frequency, polarization, and target as in the case of the far-zone RCS and in addition depends on range and antenna pattern.

Several techniques are, in principle, available for obtaining the near-zone RCS of aerospace targets. Four techniques that have been considered by Georgia Tech include (1) direct measurement, (2) theoretical calculation, (3) subarea matrix method, and (4) modal expansion technique. In the case of the direct measurement technique, a full scale missile with seeker is pulled along a rail past a full size target and the received signal versus time is recorded. This technique has the advantage of using the actual

missile and seeker with a full size target and so no question of scaling is involved. However, the data obtained from this technique is applicable only to those trajectories flown in the program and does not provide information on other targets or effects due to changing the seeker. Another approach is to employ theoretical calculations such as the geometrical theory of diffraction, physical optics, moment methods, or other similar computational techniques. Generally, such techniques are limited to targets of relatively simple geometric shape. Complicated shapes and measured data on them are difficult or impossible to include. A third technique that was considered is the subarea matrix method. Using this technique, the RCS of small portions of the target would be measured individually and would be stored in a computer. The overall RCS of the target would be obtained by combining the illumination pattern and the measured scattering characteristics of the sub-areas. Equipment problems such as positioner design and focusing system design severely limit the application of this technique.

The fourth technique, the modal expansion technique, was the method finally selected for investigation by Georgia Tech. This technique is based on proven methods for determining antenna patterns in the far-zone from measurements made in the near-zone. It can, in principle, be applied for both monostatic and bistatic cross-section determination and, in addition, the basic equipment was already available at Georgia Tech for performing these measurements. The modal expansion technique requires the measurement of the scattered fields from the target at evenly spaced points on a planar surface near the target. This measured near-field data is Fourier transformed to obtain the plane wave spectrum of the target. This plane wave spectrum can be used to predict the scattered electric and magnetic fields at any distance from the target between the measurement plane and infinity.

There are a number of advantages to using the modal expansion technique. The complete three dimensional pattern of the target is obtained instead of just principal plane cuts. In addition, the cross polarization pattern is also determined and its characteristics are known in principle for all ranges from the measurement plane to infinity. In addition, the measurements can be performed indoors, thus providing protection for the equipment and personnel. Weather problems are thus eliminated, environmental testing is possible, and signals can be radiated at classified frequencies with greatly reduced probability of being intercepted.

This report documents the present state of development of the modal expansion technique for near-zone radar cross-section of complex targets and determination of their glint characteristics. In Section II a brief review of plane wave spectrum theory is presented. In Section III a new derivation of probe correction equations is presented correcting previously published errors in these equations. A new method for obtaining the probe characteristics is presented in Section IV. This technique utilizes only a planar scanner and assumes no a priori information about the probe. This characterization technique represents a significant saving in measurement time and installation costs since previous techniques have required the use of a separate spherical positioning system to measure probe radiation patterns. Section V presents near-field glint measurements made on an F-105 model aircraft. Conclusions and recommendations based on the results of this program are presented in Section VI.

SECTION II

PLANE WAVE SPECTRUM REPRESENTATION OF FIELDS

The electric field intensity in a linear, isotropic, homogeneous and source-free region defined by $z > 0$ can be expressed [1] for $\exp(j\omega t)$ time variations as

$$\bar{E}(\bar{r}) = \frac{1}{2\pi} \int_{-\infty}^{\infty} \int_{-\infty}^{\infty} \bar{A}(k_x, k_y) e^{-jk \cdot \bar{r}} dk_x dk_y \quad (1)$$

where

$$\bar{r} = x\bar{a}_x + y\bar{a}_y + z\bar{a}_z = \text{the observation point} \quad (2)$$

$$\bar{k} = k_x\bar{a}_x + k_y\bar{a}_y + k_z\bar{a}_z = \text{the propagation vector} \quad (3)$$

$$k_z = \sqrt{k^2 - k_x^2 - k_y^2} = \text{the } z \text{ component of the propagation vector} \quad (4)$$

$$k = \frac{2\pi}{\lambda} = \omega\sqrt{\mu\epsilon} = \text{the wavenumber in the medium } z > 0 \quad (5)$$

The plane wave spectrum \bar{A} can be determined from (1) if the electric field intensity is known on the $z=0$ plane. Then

$$\bar{A}(k_x, k_y) = \frac{1}{2\pi} \int_{-\infty}^{\infty} \int_{-\infty}^{\infty} \bar{E}(x, y, 0) e^{j(xk_x + yk_y)} dx dy \quad (6)$$

Only two components of \bar{E} need to be used in (6) since the third component of \bar{A} can be determined from [1]

$$k_x A_x + k_y A_y + k_z A_z = 0 \quad (7)$$

The magnetic field intensity can also be obtained from the plane wave spectrum [1] and is given by

$$\bar{H}(\bar{r}) = \frac{1}{2\pi\omega\mu} \int_{-\infty}^{\infty} \int_{-\infty}^{\infty} \bar{k} \times \bar{A}(k_x, k_y) e^{-jk \cdot \bar{r}} dk_x dk_y \quad (8)$$

Usually \bar{E} is zero (or at least below the system noise level) over most of the $z=0$ plane. Hence, the Fourier transforms in (6) need only be performed over a finite region of x - y space. If the transform is done discretely as on a computer, the resulting computation is expedited using the Fast Fourier Transform algorithm. If two components of the true electric field $\bar{E}(\bar{r})$ are known on the $z=0$ plane, then (6) is used to calculate two components of the plane wave spectrum. The third component is obtained from (7). The electric and magnetic fields can then be obtained anywhere in the region $z>0$ by using (1) and (8), respectively. The preceding comments apply to both radiating antennas and to scattered fields from targets.

When \bar{E} is nonzero over only a finite region of space, the near-field is typically sampled on a rectangular grid in the x - y plane at N_x points per row spaced Δx apart in the x -direction and on N_y rows spaced Δy apart in the y -direction. Fast Fourier Transforming this sampled data produces a sampled spectrum on a rectangular grid of points in the k_x - k_y plane of k -space. This grid has N_x points per row spaced Δk_x apart in the k_x -direction and N_y points spaced Δk_y apart in the k_y -direction where

$$\Delta k_x = \frac{2\pi}{\Delta x N_x} \quad (9)$$

$$\Delta k_y = \frac{2\pi}{\Delta y N_y}$$

The spectrum function is periodic due to the sampling process with a period of

$$k_{xp} = \frac{2\pi}{\Delta x}$$

$$k_{yp} = \frac{2\pi}{\Delta y} \quad (10)$$

in the k_x and k_y directions, respectively. The spatial function is also periodic due to Fourier Transform properties with a period of

$$x_p = \Delta x N_x$$

$$y_p = \Delta y N_y \quad (11)$$

in the x and y directions, respectively.

The measurement of the electric field intensity on the $z=0$ plane is corrupted by the pattern characteristics of the measurement probe. The probe characteristics must be removed from the measured data in order to obtain the true electric field of the antenna or target under test. A new derivation of the equations for removing the probe effects is presented in the next section.

SECTION III
CORRECTION FOR PROBE EFFECTS

The near-field data measured by the probe is a filtered version of the true near-field data, because the probe does not pick up energy from all directions uniformly. The filtering process of the probe must be removed from the measured data to obtain the true near-field data. This inverse filtering process is called "probe correction" in near-field studies.

The object (antenna or scatterer) producing the electric field of interest is assumed to lie in the region $z < 0$. A probe is placed at position

$$\bar{P} = x_p \bar{a}_x + y_p \bar{a}_y + z_p \bar{a}_z$$

where $z_p > 0$ (see Figure 1). The voltage measured by the probe at this location will be calculated next in terms of the plane wave spectra of the object and the probe. A new derivation of the probe correction equations for near-field data will be presented since a review of previously published [2,3] probe correction equations revealed errors in them.

The electric field intensity produced by the object under test can from (1) be expressed in the region $z > 0$ as

$$\bar{E}_a(\bar{r}) = \frac{1}{2\pi} \int_{-\infty}^{\infty} \int_{-\infty}^{\infty} \bar{A}_a(k_x, k_y) e^{-jk \cdot \bar{r}} dk_x dk_y \quad (12)$$

while the magnetic field intensity in the same region can be obtained from (7) and (8). The x and y components of this magnetic field are

$$H_{ax}(\bar{r}) = \frac{-1}{2\pi\omega\mu} \int_{-\infty}^{\infty} \int_{-\infty}^{\infty} k_z^{-1} [k_x k_y A_{ax} + (k^2 - k_x^2) A_{ay}] e^{-jk \cdot \bar{r}} dk_x dk_y \quad (13)$$

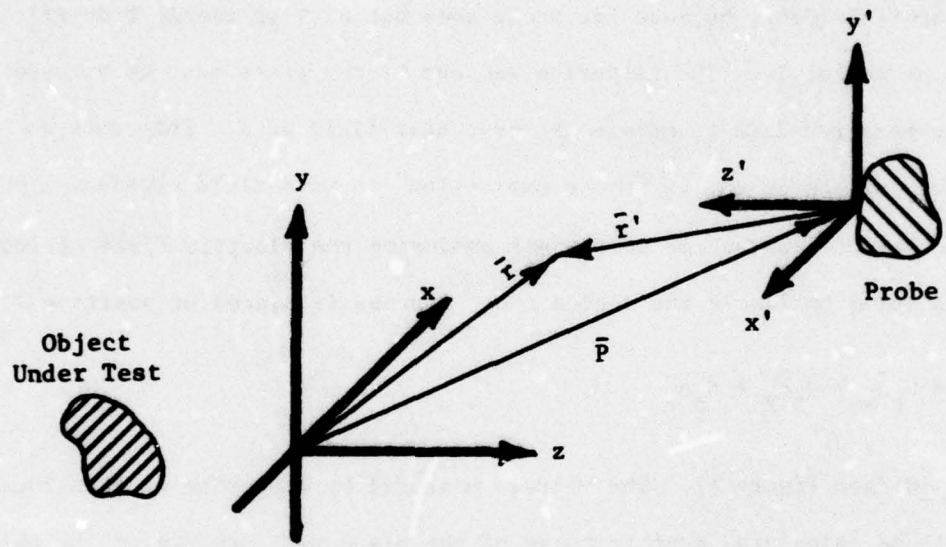


Figure 1. Probe measurement of target or antenna.

$$H_{ay}(\vec{r}) = \frac{1}{2\pi\omega\mu} \int_{-\infty}^{\infty} \int_{-\infty}^{\infty} k_z^{-1} [(k_x^2 - k_y^2) A_{ax} + k_x k_y A_{ay}] e^{-jk \cdot \vec{r}} dk_x dk_y \quad (14)$$

where A_{ax} and A_{ay} are the x and y components, respectively, of \vec{A}_a .

Consider the probe first located in the region $z < 0$. The x and y components of the fields produced by the probe (when it is transmitting) at an arbitrary point \vec{r}' in the region $z > 0$ can be represented by analogy with (12) through (14) as

$$E_{px'}(\vec{r}') = \frac{1}{2\pi} \int_{-\infty}^{\infty} \int_{-\infty}^{\infty} A_{px}(k_x, k_y) e^{-jk \cdot \vec{r}'} dk_x dk_y$$

$$E_{py'}(\vec{r}') = \frac{1}{2\pi} \int_{-\infty}^{\infty} \int_{-\infty}^{\infty} A_{py}(k_x, k_y) e^{-jk \cdot \vec{r}'} dk_x dk_y$$

$$H_{px'}(\vec{r}') = \frac{-1}{2\pi\omega\mu} \int_{-\infty}^{\infty} \int_{-\infty}^{\infty} k_z^{-1} [k_x k_y A_{px} + (k_x^2 - k_y^2) A_{py}] e^{-jk \cdot \vec{r}'} dk_x dk_y$$

$$H_{py'}(\vec{r}') = \frac{1}{2\pi\omega\mu} \int_{-\infty}^{\infty} \int_{-\infty}^{\infty} k_z^{-1} [(k_x^2 - k_y^2) A_{px} + k_x k_y A_{py}] e^{-jk \cdot \vec{r}'} dk_x dk_y$$

The primed coordinate system used above to specify the components of the probe fields initially coincides with the unprimed system. This probe is then translated without rotation by the vector \vec{P} and then rotated 180° in the x - z plane as shown in Figure 1.

It is next necessary to have the probe fields expressed in terms of unprimed coordinates in calculating the voltage induced in the probe at its new location. To do this first of all notice that the unit vectors along the coordinate axes are related by $\bar{a}_x' = -\bar{a}_x$, $\bar{a}_y' = \bar{a}_y$, and $\bar{a}_z' = -\bar{a}_z$. At the same observation point in space $\vec{r}' = \vec{r} - \vec{P}$, hence

$$x' = (\vec{r} - \vec{P}) \cdot \bar{a}_x' = (\vec{r} - \vec{P}) \cdot (-\bar{a}_x) = -x + x_p$$

$$y' = y - y_p$$

$$z' = -z + z_p$$

Thus in terms of the unprimed coordinate system, the x and y components of the fields produced by the probe from its translated and rotated location are

$$E_{px}(\bar{r}) = \frac{-1}{2\pi} \int_{-\infty}^{\infty} \int_{-\infty}^{\infty} A_{px}(k_x, k_y) e^{\xi} dk_x dk_y \quad (15)$$

$$E_{py}(\bar{r}) = \frac{1}{2\pi} \int_{-\infty}^{\infty} \int_{-\infty}^{\infty} A_{py}(k_x, k_y) e^{\xi} dk_x dk_y \quad (16)$$

$$H_{px}(\bar{r}) = \frac{1}{2\pi\omega\mu} \int_{-\infty}^{\infty} \int_{-\infty}^{\infty} k_z^{-1} [k_x k_y A_{px}(k_x, k_y) + (k_x^2 - k_y^2) A_{py}(k_x, k_y)] e^{\xi} dk_x dk_y \quad (17)$$

$$H_{py}(\bar{r}) = \frac{1}{2\pi\omega\mu} \int_{-\infty}^{\infty} \int_{-\infty}^{\infty} k_z^{-1} [(k_x^2 - k_y^2) A_{px}(k_x, k_y) + k_x k_y A_{py}(k_x, k_y)] e^{\xi} dk_x dk_y \quad (18)$$

where

$$\xi = -j(-k_x x + k_x x_p + k_y y - k_y y_p - k_z z + k_z z_p)$$

Let the surface S_1 be the $z=0$ plane and let S_∞ be a hemisphere of infinite radius, centered at $\bar{r}=0$ and existing in the region $z \geq 0$. Assume that all fields scattered back and forth between the probe and the object under test are negligible. Let V be the volume bounded by S_1 and S_∞ in the region $z > 0$. Then by the reciprocity theorem [4]

$$-\oint_{S_1+S_\infty} (\bar{E}_a \times \bar{H}_p - \bar{E}_p \times \bar{H}_a) \cdot \bar{n} da = \iiint_V (\bar{E}_a \cdot \bar{J}_p - \bar{E}_p \cdot \bar{J}_a) dv \quad (19)$$

where \bar{J}_a and \bar{J}_p are the source currents producing the \bar{E}_a , \bar{H}_a and the \bar{E}_p , \bar{H}_p fields, respectively, and \bar{n} is a unit vector normal to the surface and pointing out of V.

In the region V, $\bar{J}_a = 0$ while over S_∞ the integrand on the left side of the last equation is identically zero [4]. The volume integral of $\bar{E}_a \cdot \bar{J}_p$ is simply $-V_{pa} I_p$ [5] where I_p is the probe source current that produces \bar{E}_p and \bar{H}_p . V_{pa} is the voltage produced by the object under test in the probe when $I_p = 0$. The internal impedance of the probe source-current generator should still be connected to the probe when V_{pa} is measured. From the preceding observations, it can be seen that (19) can be rewritten as

$$-V_{pa} I_p = I_a + I_b + I_c + I_d \quad (20)$$

where

$$I_a = \int_{-\infty}^{\infty} \int_{-\infty}^{\infty} E_{ax} H_{py} \Big|_{z=0} dx dy$$

$$I_b = - \int_{-\infty}^{\infty} \int_{-\infty}^{\infty} E_{ay} H_{px} \Big|_{z=0} dx dy$$

$$I_c = - \int_{-\infty}^{\infty} \int_{-\infty}^{\infty} E_{px} H_{ay} \Big|_{z=0} dx dy$$

$$I_d = \int_{-\infty}^{\infty} \int_{-\infty}^{\infty} E_{py} H_{ax} \Big|_{z=0} dx dy$$

These last four integrals can be evaluated in terms of the previous representations of the fields. Using (12) and (18) I_a can be written as

$$I_a = \frac{1}{(2\pi)^2 \omega \mu} \int_{-\infty}^{\infty} \int_{-\infty}^{\infty} \int_{-\infty}^{\infty} \int_{-\infty}^{\infty} \int_{-\infty}^{\infty} \int_{-\infty}^{\infty} A_{ax}(k_x, k_y) \left[\frac{1}{k_z'} \right] [(k^2 - k_y'^2) \\ A_{px}(k_x', k_y') + k_x' k_y' A_{py}(k_x', k_y')] e^{-j[k_x x + k_y y - k_x' x + k_x' x_p + k_y' y - k_y' y_p + k_z' z_p]} \\ dk_x dk_y dk_x' dk_y' dx dy \quad (21)$$

Primes have been used on the probe integration variables to distinguish them from those of the object-under-test variables. Interchange the order of integration in (21) and perform the x,y integration first. Note that [6]

$$\int_{-\infty}^{\infty} \int_{-\infty}^{\infty} e^{jx(k_x' - k_x)} e^{jy(-k_y - k_y')} dx dy = (2\pi)^2 \delta(k_x' - k_x) \delta(k_y + k_y')$$

where δ is the Dirac delta function. Integrating (21) with respect to x and y and then k_x' and k_y' yields $k_x' + k_x$ and $k_y' + -k_y$ so that

$$I_a = \frac{1}{\omega \mu} \int_{-\infty}^{\infty} \int_{-\infty}^{\infty} A_{ax}(k_x, k_y) k_z^{-1} [(k^2 - k_y^2) A_{px}(k_x, -k_y) - k_x k_y A_{py}(k_x, -k_y)] \\ e^{-j\bar{k} \cdot \bar{p}} dk_x dk_y$$

Similarly

$$I_b = \frac{-1}{\omega \mu} \int_{-\infty}^{\infty} \int_{-\infty}^{\infty} A_{ay}(k_x, k_y) k_z^{-1} [-k_x k_y A_{px}(k_x, -k_y) + (k^2 - k_x^2) A_{py}(k_x, -k_y)] \\ e^{-j\bar{k} \cdot \bar{p}} dk_x dk_y$$

and

$$I_c = \frac{1}{\omega \mu} \int_{-\infty}^{\infty} \int_{-\infty}^{\infty} A_{px}(k_x, -k_y) k_z^{-1} [(k^2 - k_y^2) A_{ax}(k_x, k_y) + k_x k_y A_{ay}(k_x, k_y)] \\ e^{-j\bar{k} \cdot \bar{p}} dk_x dk_y$$

and

$$I_d = \frac{-1}{\omega\mu} \int_{-\infty}^{\infty} \int_{-\infty}^{\infty} A_{py}(k_x, -k_y) k_z^{-1} [k_x k_y A_{ax}(k_x, k_y) + (k_x^2 - k_y^2) A_{ay}(k_x, k_y)] e^{-jk \cdot \bar{P}} dk_x dk_y$$

Combining (20) and the last four equations yields

$$\begin{aligned} -V_{pa} I_p &= \frac{1}{\omega\mu} \int_{-\infty}^{\infty} \int_{-\infty}^{\infty} \left\{ A_{ax}(k_x, k_y) k_z^{-1} [2(k_y^2 - k_x^2) A_{px}(k_x, -k_y) - 2k_x k_y A_{py}(k_x, -k_y)] \right. \\ &\quad \left. + A_{ay}(k_x, k_y) k_z^{-1} [2k_x k_y A_{px}(k_x, -k_y) - 2(k_x^2 - k_y^2) A_{py}(k_x, -k_y)] \right\} e^{-jk \cdot \bar{P}} dk_x dk_y \end{aligned} \quad (22)$$

Equation (22) gives the voltage V_{pa} produced in the probe by the object under test when the probe is at position \bar{P} . Usually A_{ax} and A_{ay} are to be found from the measured probe voltage and the known probe spectrum. Equation (22) gives only one equation in terms of these two unknowns. Hence, a second independent measurement must be made either with the same probe or with a different probe. The same probe in a different orientation will be used in this derivation to obtain the second equation.

Consider a second orientation of the same probe produced by rotating the probe 90° clockwise about the z' axis so that the new $+x'$ axis now points in the same direction as the old $+y'$ axis (see Figure 1). Call this new coordinate system the double prime system. The unit vectors along the coordinate axes are now related by $\bar{a}_{x''} = \bar{a}_y$, $\bar{a}_{y''} = \bar{a}_x$, and $\bar{a}_{z''} = -\bar{a}_z$. At the same observation point in space $\bar{r}'' = \bar{r} - \bar{P}$ and so

$$x'' = (\bar{r} - \bar{P}) \cdot \bar{a}_{x''} = (\bar{r} - \bar{P}) \cdot \bar{a}_y = y - y_p$$

$$y'' = x - x_p$$

$$z'' = -z + z_p$$

Thus, the fields produced by the probe from its second orientation in terms of the unprimed coordinate system are

$$E_{p2x}(\bar{r}) = \frac{1}{2\pi} \int_{-\infty}^{\infty} \int_{-\infty}^{\infty} A_{py}(k_x, k_y) e^{\tau} dk_x dk_y$$

$$E_{p2y}(\bar{r}) = \frac{1}{2\pi} \int_{-\infty}^{\infty} \int_{-\infty}^{\infty} A_{px}(k_x, k_y) e^{\tau} dk_x dk_y$$

$$H_{p2x}(\bar{r}) = \frac{1}{2\pi\omega\mu} \int_{-\infty}^{\infty} \int_{-\infty}^{\infty} k_z^{-1} [(k_x^2 - k_y^2) A_{px} + k_x k_y A_{py}] e^{\tau} dk_x dk_y$$

$$H_{p2y}(\bar{r}) = \frac{-1}{2\pi\omega\mu} \int_{-\infty}^{\infty} \int_{-\infty}^{\infty} k_z^{-1} [k_x k_y A_{px} + (k_x^2 - k_y^2) A_{py}] e^{\tau} dk_x dk_y$$

where

$$\tau = -j(k_x y - k_x y_p + k_y x - k_y x_p - k_z z + k_z z_p)$$

Reciprocity is again used and (19) simplifies to (20) in the form

$$-V_{p2a} I_p = I_a + I_b + I_c + I_d \quad (23)$$

where

$$I_a = \int_{-\infty}^{\infty} \int_{-\infty}^{\infty} E_{ax} H_{p2y} \Big|_{z=0} dx dy$$

$$I_b = - \int_{-\infty}^{\infty} \int_{-\infty}^{\infty} E_{ay} H_{p2x} \Big|_{z=0} dx dy$$

$$I_c = - \int_{-\infty}^{\infty} \int_{-\infty}^{\infty} E_{p2x} H_{ay} \Big|_{z=0} dx dy$$

$$I_d = \int_{-\infty}^{\infty} \int_{-\infty}^{\infty} E_{p2y} H_{ax} \Big|_{z=0} dx dy$$

V_{p2a} is the voltage induced in the probe in its second orientation by the object under test. Substituting the "a" and the "p2" fields into the first integral yields

$$I_a = \frac{-1}{(2\pi)^2 \omega \mu} \int_{-\infty}^{\infty} \int_{-\infty}^{\infty} \int_{-\infty}^{\infty} \int_{-\infty}^{\infty} \int_{-\infty}^{\infty} \int_{-\infty}^{\infty} A_{ax}(k_x, k_y) \left[\frac{1}{k_z} \right] [k'_x k'_y A_{px}(k'_x, k'_y) + (k^2 - k'^2_x) A_{py}(k'_x, k'_y)] e^{\nu dk_x dk_y dk'_x dk'_y dx dy$$

where

$$\nu = -j(k_x x + k_y y + k'_x y - k'_y x + k'_x x - k'_y y + k'_z z_p)$$

Using [6]

$$\int_{-\infty}^{\infty} \int_{-\infty}^{\infty} e^{jx(-k_x - k'_x)} e^{jy(-k_y - k'_y)} dx dy = (2\pi)^2 \delta(k_x + k'_x) \delta(k_y + k'_y)$$

in the last equation and first integrating with respect to x and y and then with respect to k'_x and k'_y yields $k'_x \rightarrow -k_y$ and $k'_y \rightarrow -k_x$ so that

$$I_a = \frac{-1}{\omega \mu} \int_{-\infty}^{\infty} \int_{-\infty}^{\infty} A_{ax}(k_x, k_y) k_z^{-1} [k_x k_y A_{px}(-k_y, -k_x) + (k^2 - k_y^2) A_{py}(-k_y, -k_x)] e^{-jk \cdot \bar{P}} dk_x dk_y$$

Similarly

$$I_b = \frac{-1}{\omega\mu} \int_{-\infty}^{\infty} \int_{-\infty}^{\infty} A_{ay}(k_x, k_y) k_z^{-1} [(k^2 - k_x^2) A_{px}(-k_y, -k_x) + k_x k_y A_{py}(-k_y, -k_x)]$$

$$e^{-j\bar{k} \cdot \bar{P}} dk_x dk_y$$

$$I_c = \frac{-1}{\omega\mu} \int_{-\infty}^{\infty} \int_{-\infty}^{\infty} A_{py}(-k_y, -k_x) k_z^{-1} [(k^2 - k_y^2) A_{ax}(k_x, k_y) + k_x k_y A_{ay}(k_x, k_y)]$$

$$e^{-j\bar{k} \cdot \bar{P}} dk_x dk_y$$

$$I_d = \frac{-1}{\omega\mu} \int_{-\infty}^{\infty} \int_{-\infty}^{\infty} A_{px}(-k_y, -k_x) k_z^{-1} [k_x k_y A_{ax}(k_x, k_y) + (k^2 - k_x^2) A_{ay}(k_x, k_y)]$$

$$e^{-j\bar{k} \cdot \bar{P}} dk_x dk_y$$

Combining (23) and the last four equations yields

$$\begin{aligned} -v_{p2a} I_p &= \frac{1}{\omega\mu} \int_{-\infty}^{\infty} \int_{-\infty}^{\infty} \left\{ A_{ax}(k_x, k_y) k_z^{-1} [-2k_x k_y A_{px}(-k_y, -k_x) - 2(k^2 - k_y^2) \right. \\ &\quad A_{py}(-k_y, -k_x)] + A_{ay}(k_x, k_y) k_z^{-1} [-2(k^2 - k_x^2) A_{px}(-k_y, -k_x) \right. \\ &\quad \left. \left. - 2k_x k_y A_{py}(-k_y, -k_x)] \right\} e^{-j\bar{k} \cdot \bar{P}} dk_x dk_y \end{aligned} \quad (24)$$

Next define the Fourier transforms of the measured probe voltages as follows:

$$A_{ma}(k_x, k_y) = \frac{1}{2\pi} \int_{-\infty}^{\infty} \int_{-\infty}^{\infty} v_{pa}(\bar{P}) e^{j[k_x x_p + k_y y_p]} dx_p dy_p \quad (25)$$

$$A_{mb}(k_x, k_y) = \frac{1}{2\pi} \int_{-\infty}^{\infty} \int_{-\infty}^{\infty} V_{p2a}(\bar{p}) e^{j[k_x x_p + k_y y_p]} dx_p dy_p \quad (26)$$

Also, note that [6]

$$\begin{aligned} & \int_{-\infty}^{\infty} \int_{-\infty}^{\infty} e^{j[-k_x x_p - k_y y_p - k_z z_p + k'_x x_p + k'_y y_p]} dx_p dy_p \\ &= (2\pi)^2 e^{-jk_z z_p} \delta(k'_x - k_x) \delta(k'_y - k_y) \end{aligned}$$

and that $\omega \mu = kn$ where n = the characteristic impedance of the $z>0$ medium.

Now perform the double Fourier transform of (22) and of (24) with respect to x_p and y_p . Using Equation (25) and the equations following it one can obtain

$$\begin{aligned} -A_{ma}(k_x, k_y) \left(\frac{I_p kn}{4\pi} \right) &= \frac{e^{-jk_z z_p}}{k_z} \left\{ A_{ax}(k_x, k_y) [(k^2 - k_y^2) A_{px}(k_x, -k_y) - k_x k_y A_{py}(k_x, -k_y)] \right. \\ &\quad \left. + A_{ay}(k_x, k_y) [k_x k_y A_{px}(k_x, -k_y) - (k^2 - k_x^2) A_{py}(k_x, -k_y)] \right\} \\ -A_{mb}(k_x, k_y) \left(\frac{I_p kn}{4\pi} \right) &= -\frac{e^{-jk_z z_p}}{k_z} \left\{ A_{ax}(k_x, k_y) [k_x k_y A_{px}(-k_y, -k_x) + (k^2 - k_y^2) \right. \\ &\quad \left. A_{py}(-k_y, -k_x)] + A_{ay}(k_x, k_y) [(k^2 - k_x^2) A_{px}(-k_y, -k_x) + k_x k_y A_{py}(-k_y, -k_x)] \right\} \end{aligned}$$

The last two equations can be rewritten in the following form (27)

$$A_{ma}(k_x, k_y) = \left[\frac{-A_{ax}(k_x, k_y) T + A_{ay}(k_x, k_y) V}{kk_z S} \right] e^{-jk_z z_p} \quad (28)$$

$$A_{mb}(k_x, k_y) = \left[\frac{A_{ax}(k_x, k_y) W - A_{ay}(k_x, k_y) U}{kk_z S} \right] e^{-jk_z z_p}$$

which can be solved for the true spectrum of the object under test giving

$$A_{ax}(k_x, k_y) = S \left[\frac{A_{ma}(k_x, k_y)U + A_{mb}(k_x, k_y)V}{Den} \right] e^{jk_z z_p} \quad (29)$$

$$A_{ay}(k_x, k_y) = S \left[\frac{A_{ma}(k_x, k_y)W + A_{mb}(k_x, k_y)T}{Den} \right] e^{jk_z z_p} \quad (30)$$

where

$$\begin{aligned} U &= -(k^2 - k_x^2)A_{px}(-k_y, -k_x) - k_x k_y A_{py}(-k_y, -k_x) \\ V &= -k_x k_y A_{px}(k_x, -k_y) + (k^2 - k_x^2)A_{py}(k_x, -k_y) \\ W &= k_x k_y A_{px}(-k_y, -k_x) + (k^2 - k_y^2)A_{py}(-k_y, -k_x) \\ T &= (k^2 - k_y^2)A_{px}(k_x, -k_y) - k_x k_y A_{py}(k_x, -k_y) \end{aligned} \quad (31)$$

$$Den = k k_z [A_{px}(k_x, -k_y)A_{px}(-k_y, -k_x) + A_{py}(k_x, -k_y)A_{py}(-k_y, -k_x)]$$

$$S = \frac{I_p n}{4\pi}$$

$$n = \sqrt{\frac{\mu}{\epsilon}}$$

I_p = probe source current

$$k_z = \pm \sqrt{k^2 - k_x^2 - k_y^2}$$

$$k = \frac{2\pi}{\lambda} = \omega\sqrt{\mu\epsilon}$$

Equations (29) and (30) are the final equations that were desired. They show how to remove the effects of the probe from the measured data to obtain the true spectrum of the object under test. Equations (27) and (28) show how to compute the measured spectrum from the probe spectrum and the true spectrum of the object under test. A_{ma} is the measured spectrum when the probe is in the orientation for which its spectrum is specified. A_{mb} is the measured spectrum obtained when the probe is rotated 90° clockwise as seen looking from behind the probe toward the object under test.

SECTION IV

A CHARACTERIZATION TECHNIQUE FOR NEAR-FIELD PROBES

A new technique has been developed for characterizing near-field measurement probes. The technique involves measurements made only with a planar scanner and assumes that two identical probes are available. One of the two identical probes is used to measure the other and from this data the plane wave spectrum of the probe is obtained. An initial guess of the plane wave spectrum of the probe is used as a starting point and an automated, iterative procedure modifies the guessed solution so that it matches the measured data via a system of equations. The current probe characterization technique [2] requires a separate spherical positioning system for measuring the probe. Using it, the spherical components of fields are measured, recorded, and converted to k-space data. This data is then interpolated and transformed to obtain evenly spaced k-space data as is required for subsequent usage. The new technique appears to offer advantages over the old technique in overall system cost.

A. Description of Technique

Consider a particular point (k_x, k_y) in k-space at which the spectrum of the probe is to be determined. Let this point be labeled Point 1 as shown in Figure 2. It is assumed that two electrically identical probes are available and that one has been used to measure the other using a planar scanner with a separation of z_p between the two probes. Since the probe and antenna are identical, $A_{px} = A_{ax}$ and $A_{py} = A_{ay}$. The basic approach of the characterization technique is to guess the values of two components, \hat{A}_{px} and \hat{A}_{py} , of the probe spectrum and use these values to calculate the spectra \hat{A}_{ma} and \hat{A}_{mb} that would be measured using such a probe. The estimated probe

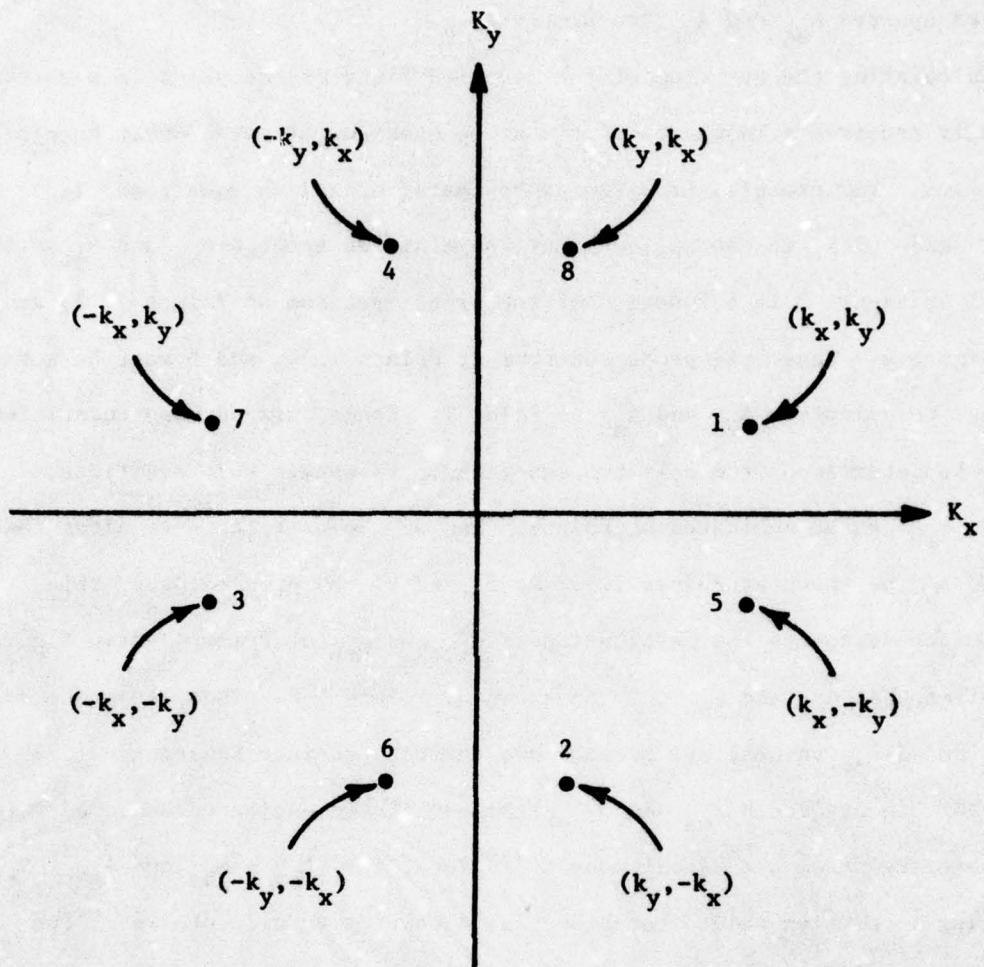


Figure 2. Location of points in k -space used in characterizing probe spectrum.

spectrum components \hat{A}_{px} and \hat{A}_{py} are then systematically adjusted so that the estimated measured spectra \hat{A}_{ma} and \hat{A}_{mb} are forced to be equal to the actual measured spectra A_{ma} and A_{mb} , respectively.

Calculating the spectrum of the measured field at one point in k-space generally requires a knowledge of the probe spectrum at seven other points in k-space. For example, from the probe characterization equations (27), (28), and (31), it can be seen that the measured spectra \hat{A}_{ma} and \hat{A}_{mb} at Point 1 of Figure 2 is a function of the probe spectrum at Points 1, 5, and 6 in Figure 2. Thus, the probe spectrum at Points 1, 5, and 6 must be guessed in order to calculate \hat{A}_{ma} and \hat{A}_{mb} at Point 1. Hence, six unknown quantities are to be determined from only two equations. To obtain more equations, \hat{A}_{ma} and \hat{A}_{mb} can be evaluated at Points 5 and 6. However, this requires that \hat{A}_{px} and \hat{A}_{py} be known at Points 1, 2, 4, 5, and 6. By proceeding in this fashion one discovers that evaluation of \hat{A}_{ma} and \hat{A}_{mb} at Points 1-8 in Figure 2 requires that \hat{A}_{px} and \hat{A}_{py} only be known at Points 1-8. Thus, 16 probe values (8 \hat{A}_{px} and 8 \hat{A}_{py} values) are guessed and substituted into Equations (27) and (28) to produce 8 \hat{A}_{ma} and 8 \hat{A}_{mb} values. These estimated measured values are subtracted from the actual measured values, i.e. $A_{ma} - \hat{A}_{ma}$ and $A_{mb} - \hat{A}_{mb}$, producing 16 complex valued equations in 16 complex valued unknowns. The solution technique tries to make these 16 equations zero simultaneously.

After solving for the probe values at these 8 points, another point (k_x, k_y) is selected. The probe values at this point and at the seven additional points associated with it as shown in Figure 2 are then determined as in the preceding discussion. All k-space will be evaluated if each point in one 45° sector, for example the first 45° of the first quadrant, of k-space is stepped through as was Point 1 in the preceding discussion. Only 8 equations in 8 unknowns are required along the line $k_x = 0$ and the line $k_x = k_y$ since

Points 5-8 are identical to Points 1-4. At the Point $k_x = k_y = 0$ only two equations and 2 unknowns are needed.

Several techniques were tested for solving the system of equations described above. The most satisfactory method was a modified Levenberg-Marquardt technique [7,8].

B. Discussion of Results

The new probe characterization technique has been applied to two X-band horns designated PX-5 and PX-6, which are shown in Figure 3. Horn PX-5 is an E-plane sectoral horn with an E-plane aperture of 1.0 inches and an H-plane aperture of 0.9 inches. Horn PX-6 is an E-plane sectoral horn with corrugations on the inside E-plane walls. The aperture of this horn is 1.38 inches in the E-plane and 0.9 inches in the H-plane. Horn PX-5 has an E-plane half-angle flare of 3.4° while the corresponding angle for PX-6 is 4.7° . All measurements were made at 9.0 GHz to demonstrate that the technique could be applied at a new frequency. All previous X-band measurements made by Georgia Tech were performed at 9.68 GHz since this was the only frequency for which complete probe data was available. This probe data was measured by Joy [2] using a separate spherical probe positioning system.

Figures 4 and 5 show the amplitude of the measured parallel and cross polarized voltages, respectively, for PX-5 measuring a second PX-5 probe that is transmitting. Measurements were made every 0.5 inches (0.38λ) in x and y and the probes were separated 0.5 inches. The plane wave spectra of these measured voltages are shown in Figures 6 through 9. The probe characterization technique forces the guessed probe spectrum to match the measured spectrum at each point in k-space. Figures 10 through 13 show the predicted probe spectrum for Probe PX-5 obtained using the new characterization technique. Notice that both parallel- and cross-polarized components are obtained in both amplitude and phase and that this information is obtained off as well as on the principal planes. To check the validity of the technique, the predicted probe spectra

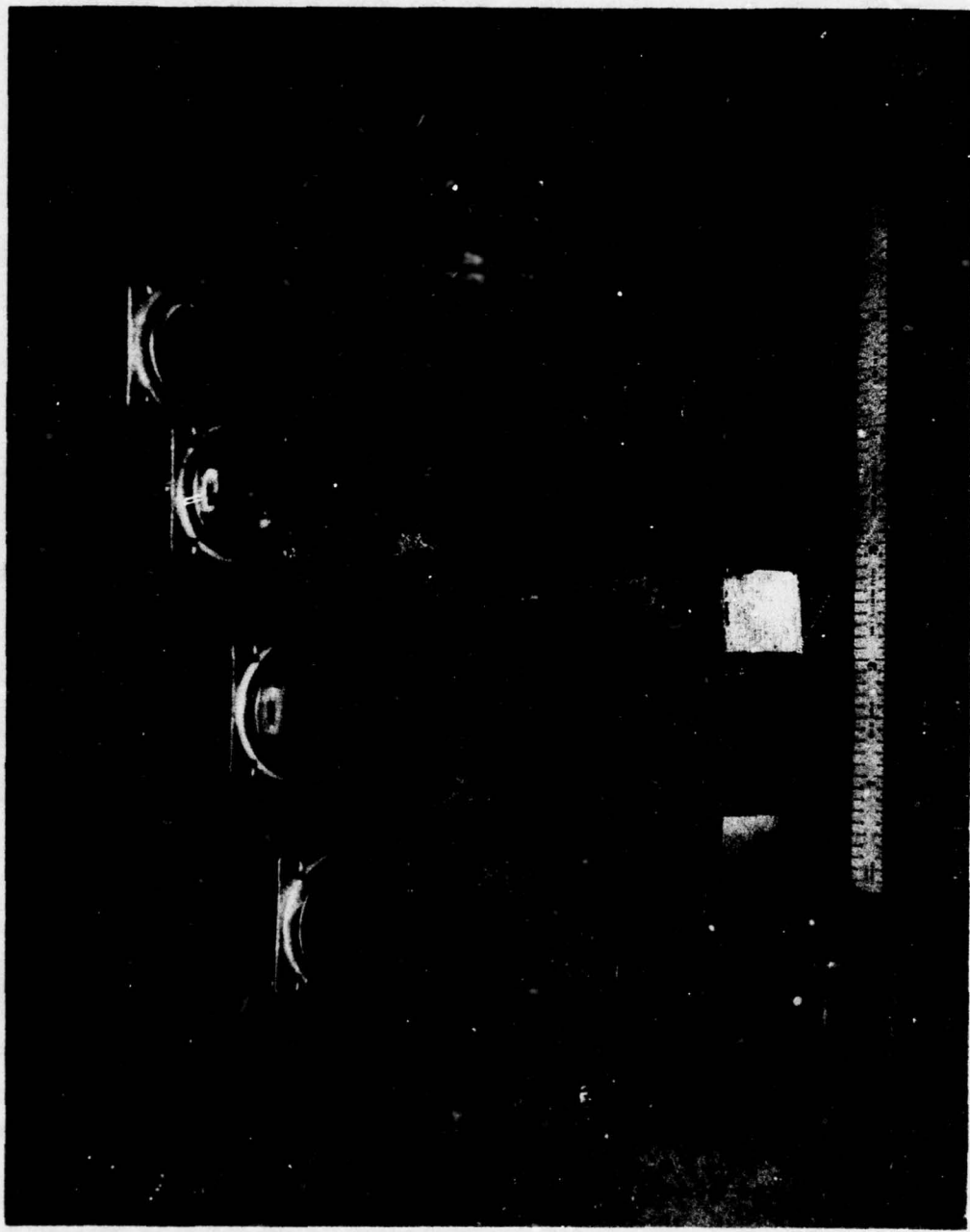
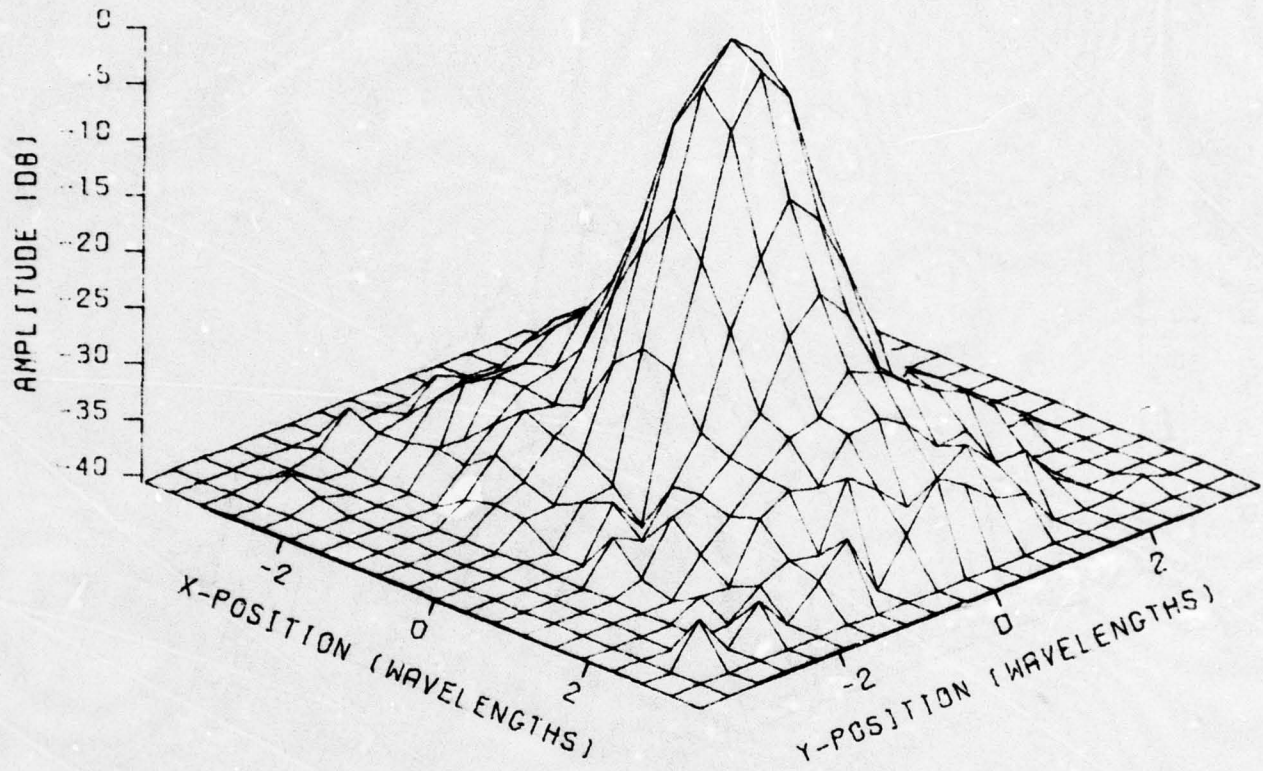
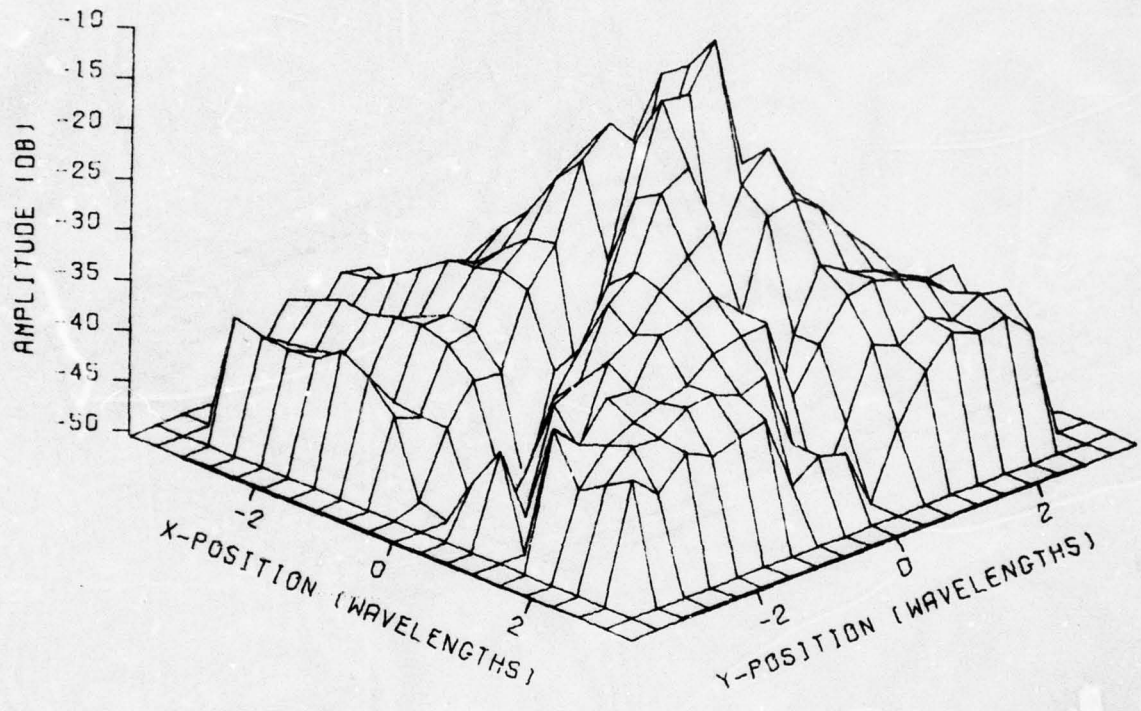


Figure 3. Photograph of X-band probe horns PX-6 on left and PX-5 on right.



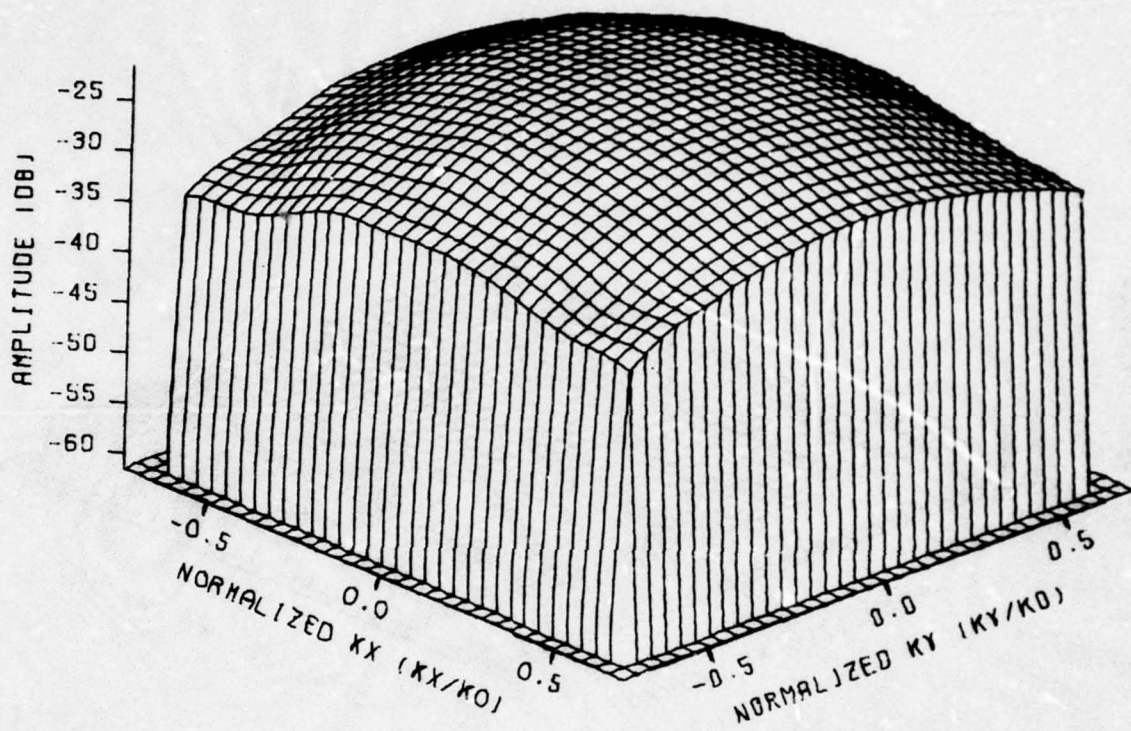
FILE 1. PX-5A MEAS. WITH PX-5B. VA

Figure 4. Amplitude of vertical (parallel) component of measured voltage obtained using one PX-5 as the probe and another PX-5 as a transmitter.



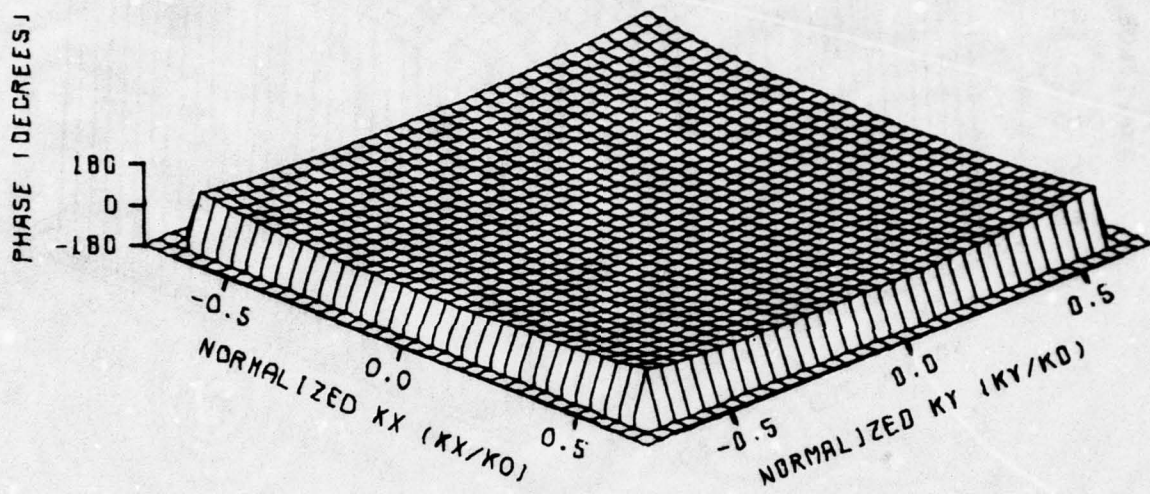
FILE 2. PX-5A MEAS. WITH PX-5B, VB

Figure 5. Amplitude of horizontal (cross) component of measured voltage obtained using one PX-5 as the probe and another PX-5 as a transmitter.



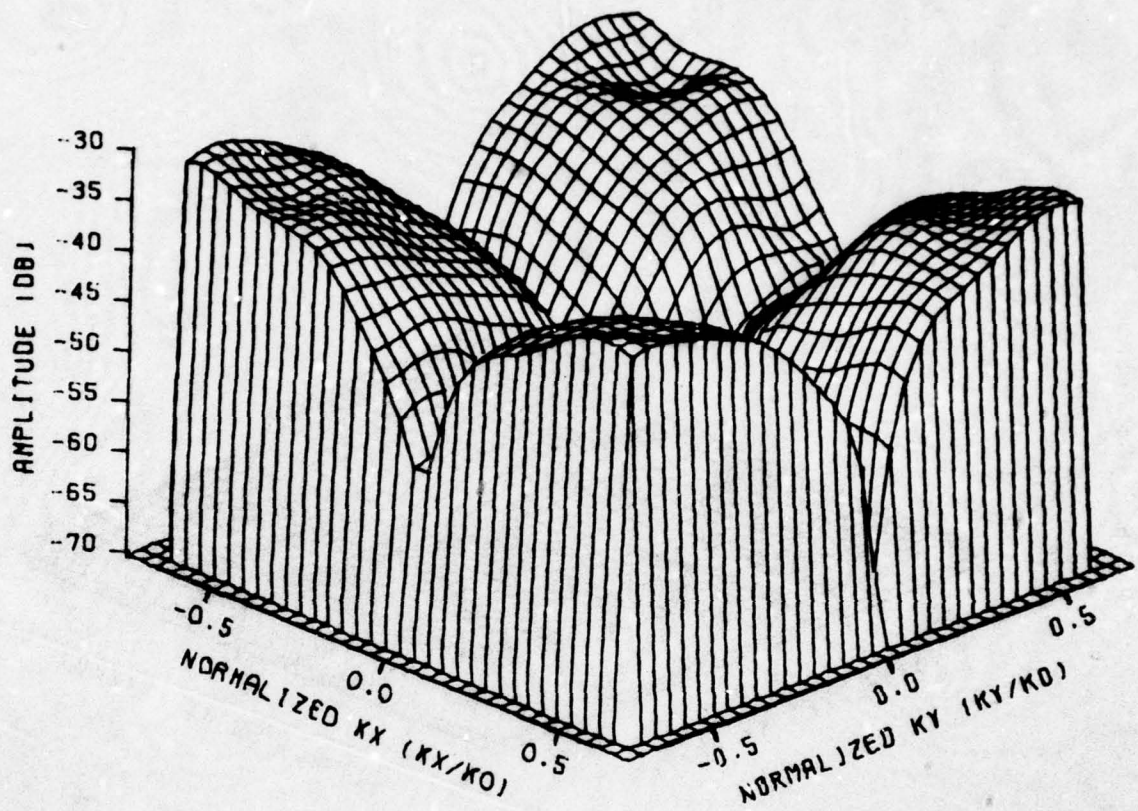
FILE 21. AMA(TRUE) FOR PX-5A MEAS. WITH PX-5B

Figure 6. Amplitude of vertical (parallel) component of measured plane wave spectrum obtained using one PX-5 as the probe and another PX-5 as a transmitter.



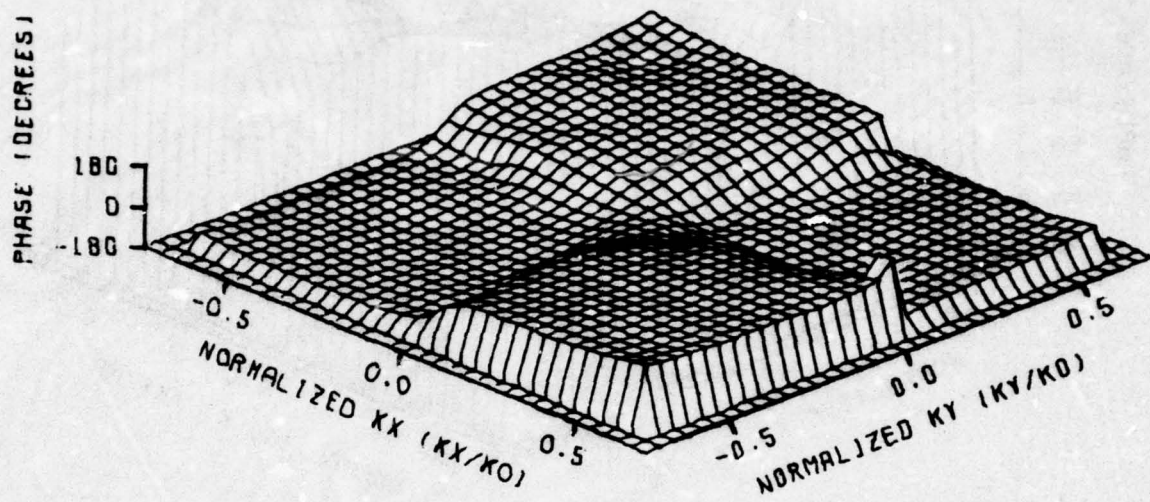
FILE 21. AMA(TRUE) FOR PX-5A MEAS. WITH PX-5B

Figure 7. Phase of vertical (parallel) component of measured plane wave spectrum obtained using one PX-5 as the probe and another PX-5 as a transmitter.



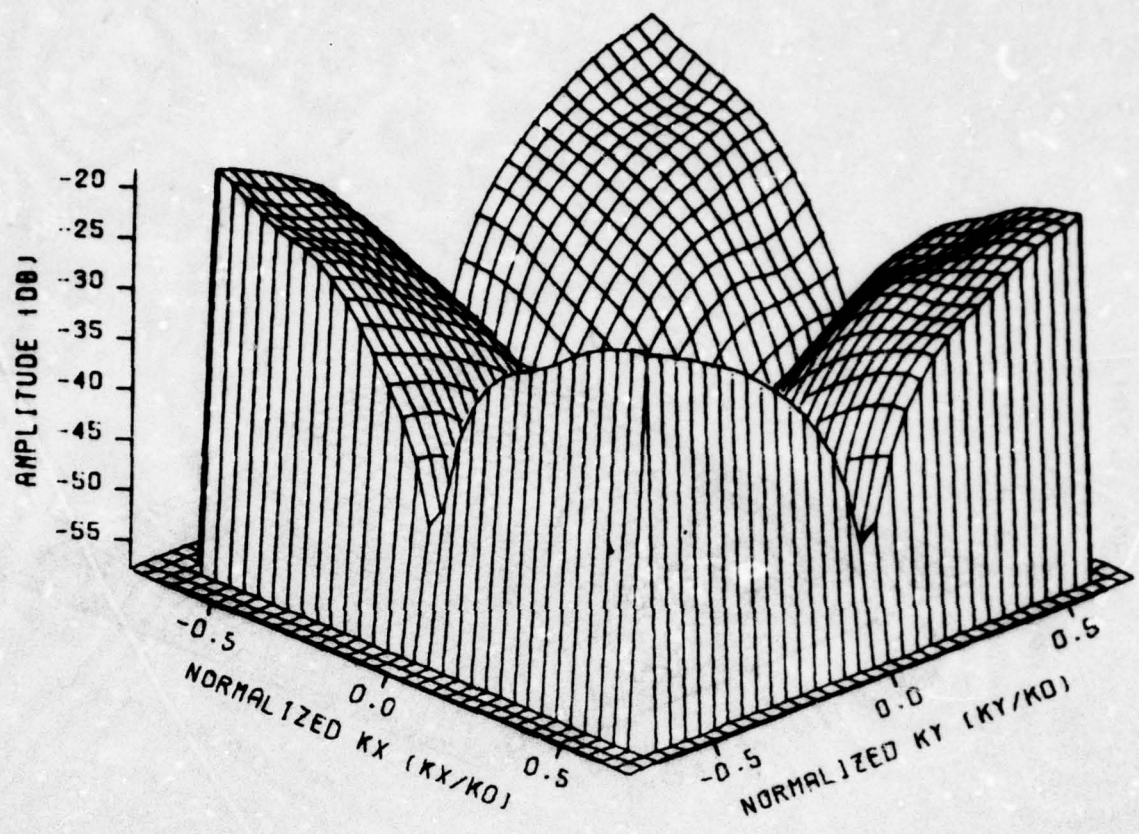
FILE 22. AMB(TRUE) FOR PX-5A MEAS. WITH PX-5B

Figure 8. Amplitude of horizontal (cross) component of measured plane wave spectrum obtained using one PX-5 as the probe and another PX-5 as a transmitter.



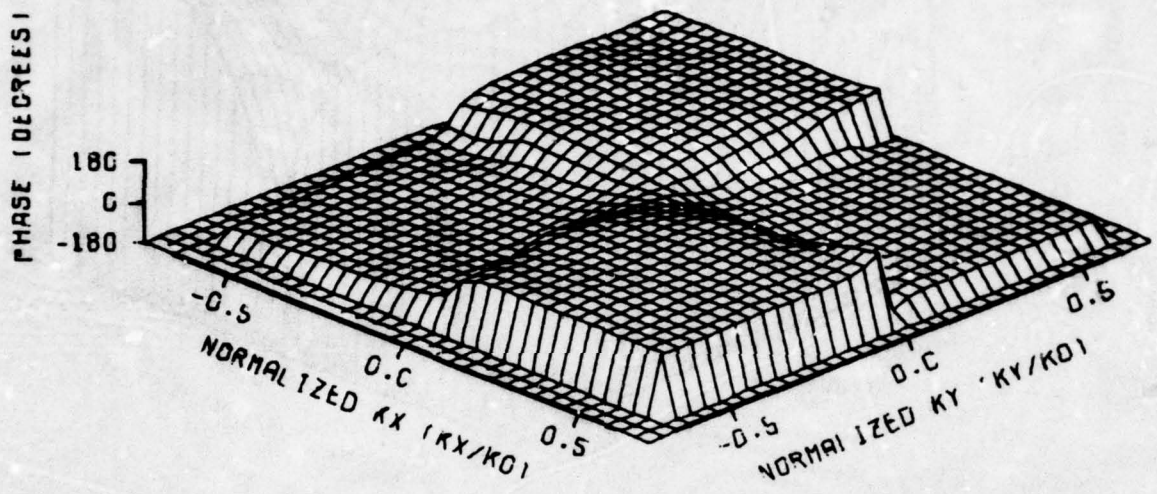
FILE 22. AMB(TRUE) FOR PX-5A MEAS. WITH PX-5B

Figure 9. Phase of horizontal (cross) component of measured plane wave spectrum obtained using one PX-5 as the probe and another PX-5 as a transmitter.



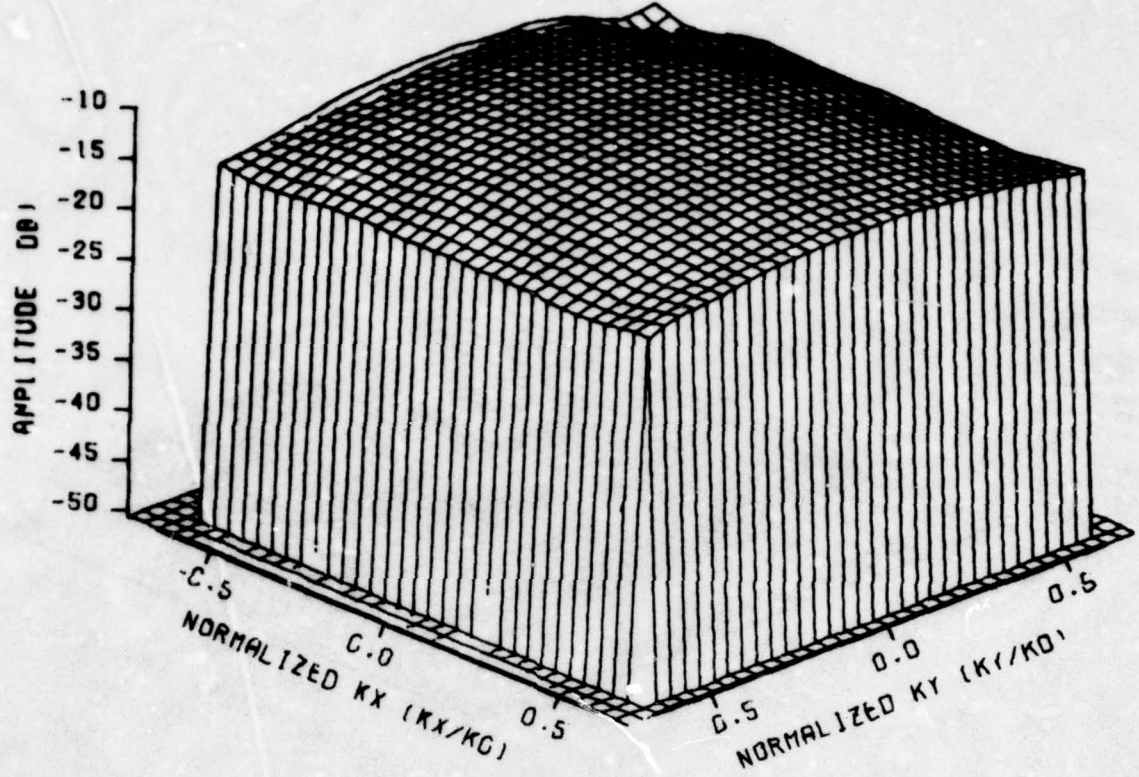
FILE 998, APX FOR PX-5

Figure 10. Amplitude of x-component of plane wave spectrum for probe PX-5 at 9 GHz.



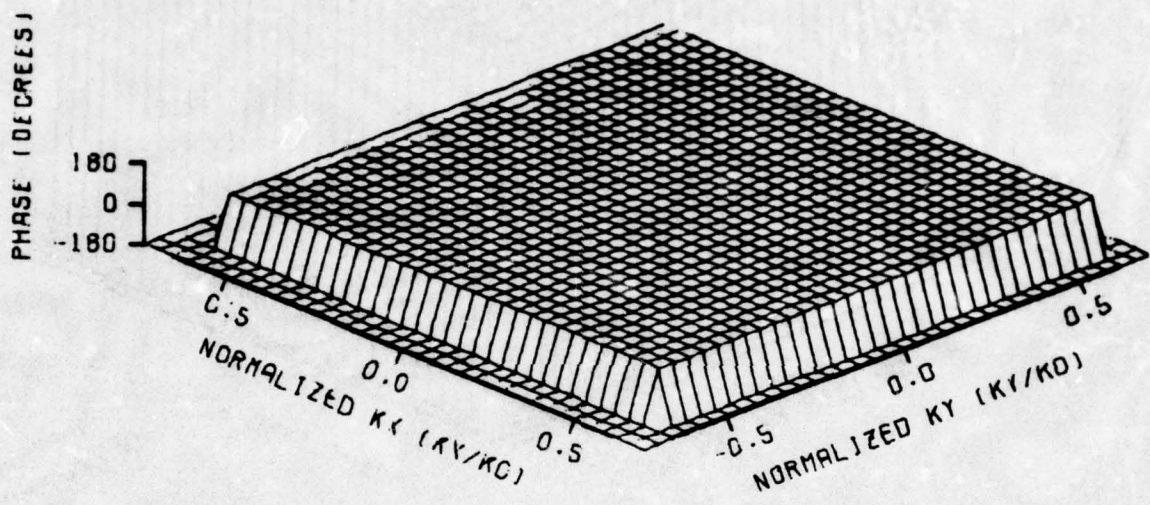
FILE 998, APX FOR PX-5

Figure 11. Phase of x-component of plane wave spectrum for probe PX-5
at 9 GHz.



FILE 999, APY FOR PX-5

Figure 12. Amplitude of y-component of plane wave spectrum for probe PX-5 at 9 GHz.



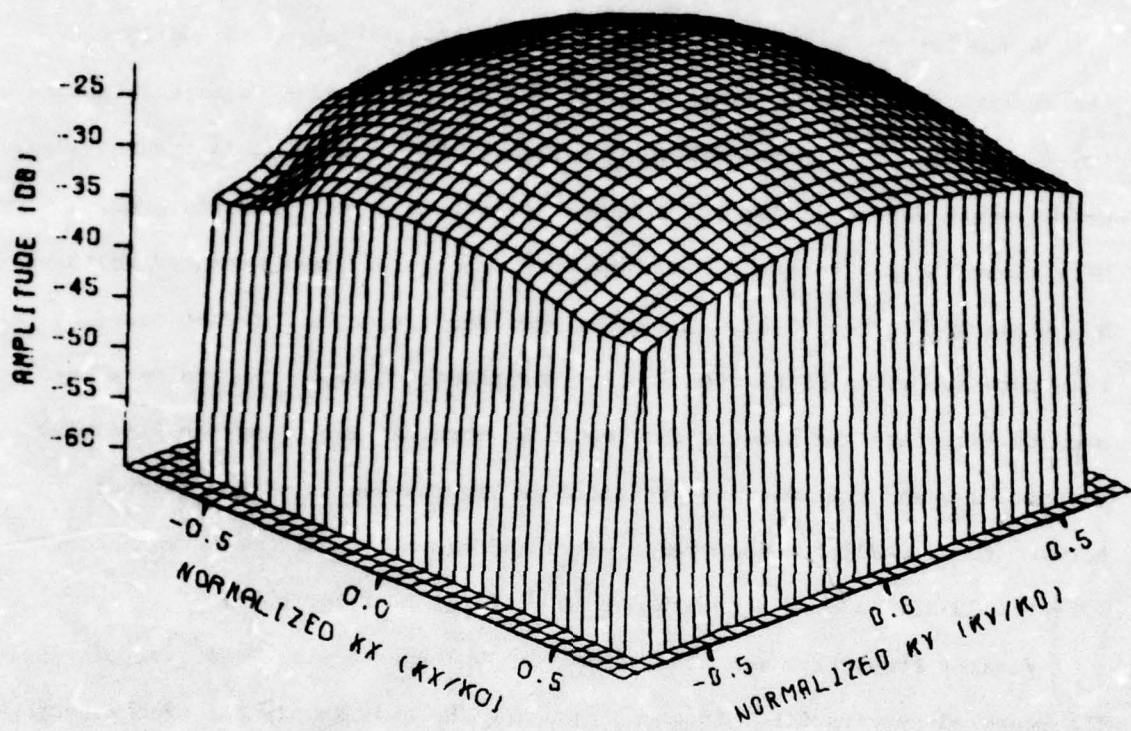
FILE 999, QPY FOR PX-5

Figure 13. Phase of y-component of plane wave spectrum for probe PX-5 at 9 GHz.

shown in Figures 10-13 were used to predict the spectra that would be obtained with one PX-5 probe measuring another. This data is shown in Figures 14-17. The good agreement between these predicted spectra and those actually measured, i.e. Figures 6-9, indicate that the new characterization technique is performing properly.

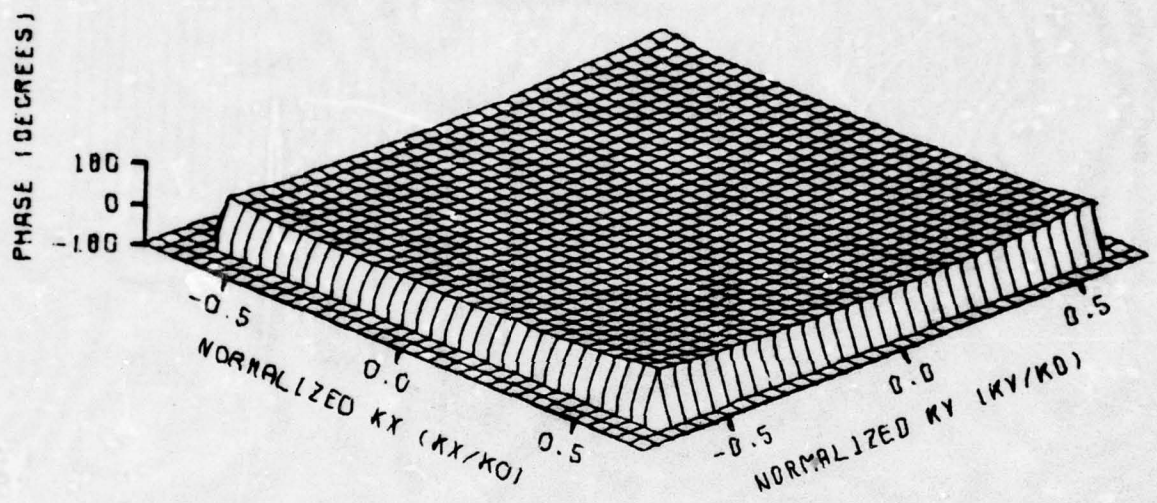
A similar procedure was applied to Probe PX-6. Figures 18 and 19 show the amplitudes of the measured parallel and cross polarized voltages, respectively, for one PX-6 probe measuring a second PX-6 probe that is transmitting. Measurements were made every 0.5 inches (0.38λ) in x and y and the probes were separated 0.5 inches. The plane wave spectra of these measured voltages are shown in Figures 20-23. The calculated probe spectra for PX-6 based on this data are given in Figures 24-27. The predicted probe spectra were then used to calculate the spectra that would be obtained measuring one PX-6 with another PX-6 and this data is presented in Figures 28-31. The agreement between these predicted measured spectra and those actually measured spectra (Figures 20-23) is good although not as close as that for PX-5.

Finally Probe PX-6 was used to measure Probe PX-5 which was transmitting. The measured spectra for this geometry using the same sample and probe spacing as before are shown in Figures 32-35. The spectra for Probes PX-5 and PX-6 obtained using the new characterization techniques were then used to predict the spectra that should be measured when PX-6 measures PX-5 and this data is given in Figures 36-39. An unknown but constant phase and amplitude error was made between each of the three sets of measurements reported above. The phase error produced a shift in the phase levels of Figures 33 versus 37 and 35 versus 39. The shape of the phase plots, however, still shows agreement. The amplitude error produced a difference in absolute levels of the plots. The good agreement among these last eight figures demonstrates that the characterization technique is working properly.



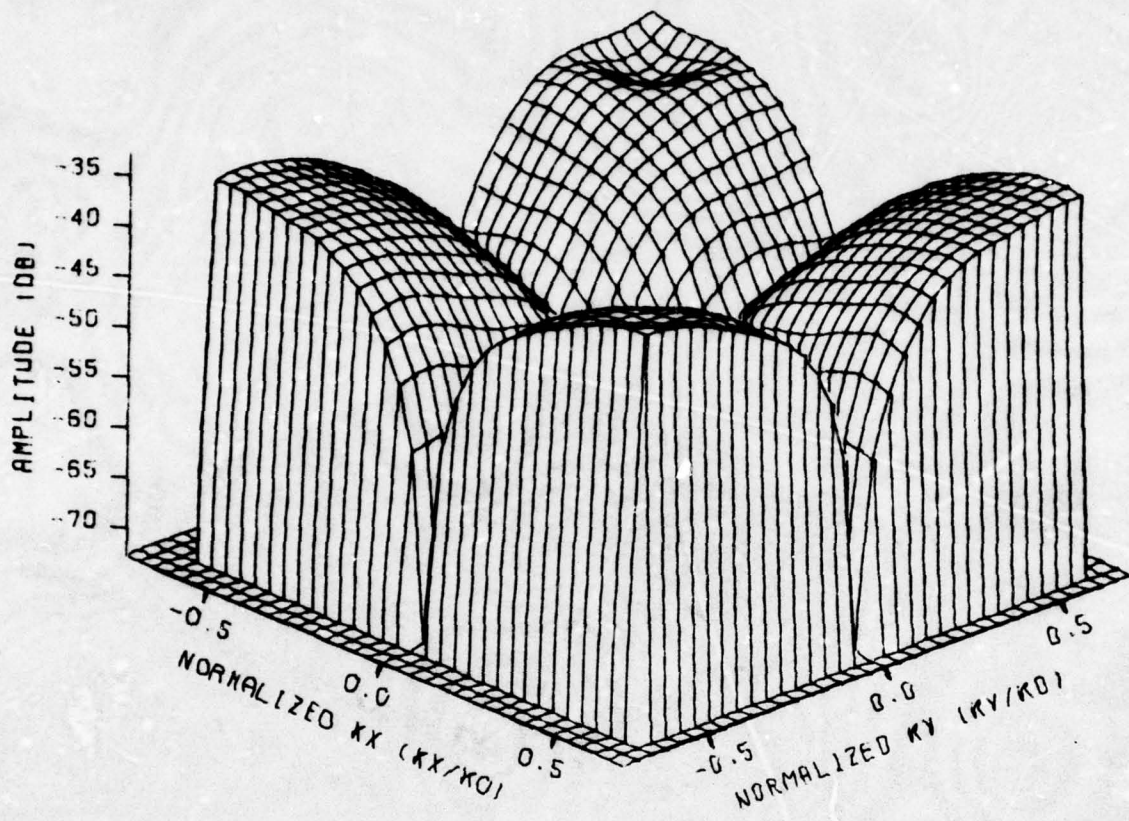
FILE 900, AMA(EST.) FOR PX-5

Figure 14. Amplitude of predicted vertical (parallel) component of measured plane wave spectrum for probe PX-5 measuring another PX-5 that is transmitting. Spectrum of PX-5 was calculated using measured data.



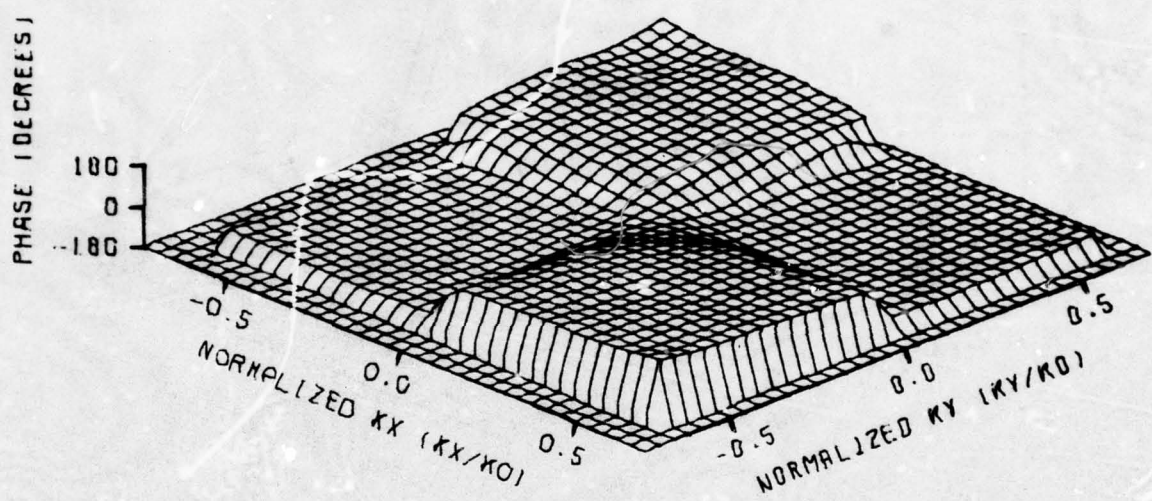
FILE 900, AMA1EST.I FOR PX-5

Figure 15. Phase of predicted vertical (parallel) component of measured plane wave spectrum for probe PX-5 measuring another PX-5 that is transmitting. Spectrum of PX-5 was calculated using measured data.



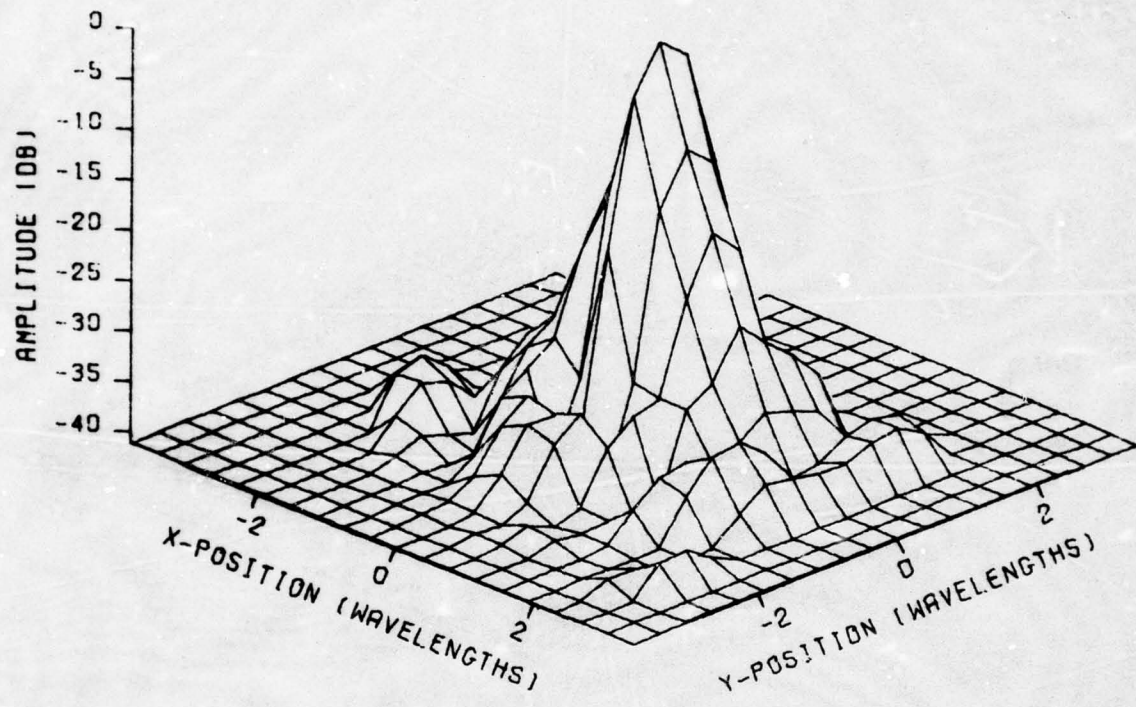
FILE 901. AMBLEST.I FOR PX-5

Figure 16. Amplitude of predicted horizontal (cross) component of measured plane wave spectrum for probe PX-5 measuring another PX-5 that is transmitting. Spectrum of PX-5 was calculated using measured data.



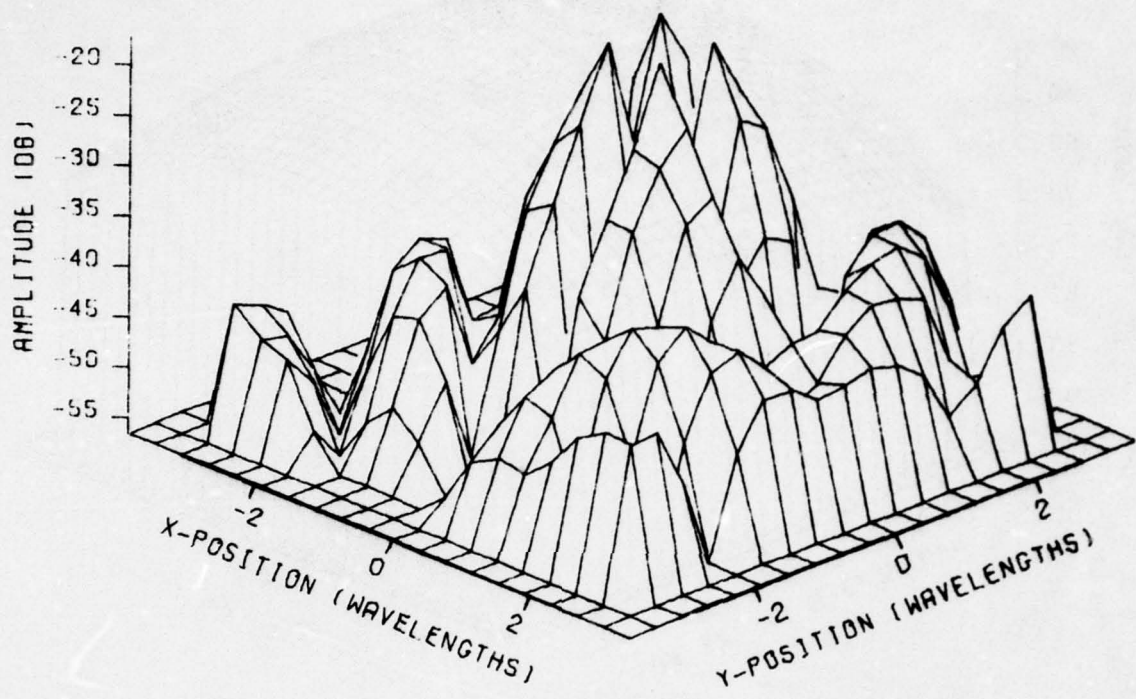
FILE 901. AMBIEST.I FOR PX-5

Figure 17. Phase of predicted horizontal (cross) component of measured plane wave spectrum for probe PX-5 measuring another PX-5 that is transmitting. Spectrum of PX-5 was calculated using measured data.



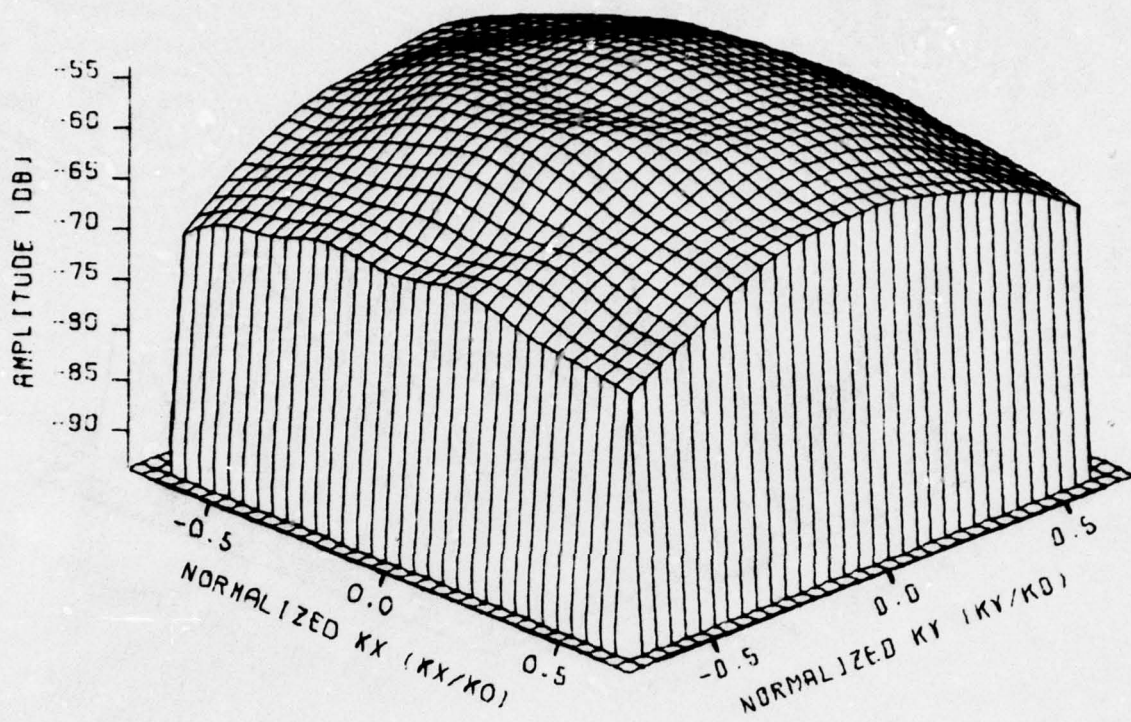
FILE 5. PX-6A MEAS. WITH PX-6B, VA

Figure 18. Amplitude of vertical (parallel) component of measured voltage obtained using one PX-6 as the probe and another PX-6 as a transmitter.



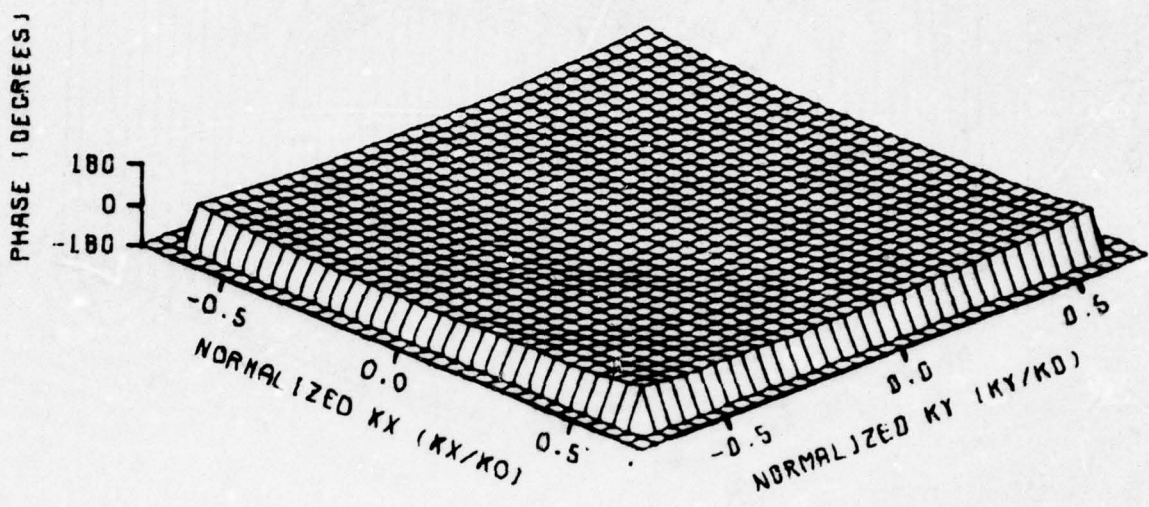
FILE 6. PX-6A MEAS. WITH PX-6B. VB

Figure 19. Amplitude of horizontal (cross) component of measured voltage obtained using one PX-6 as the probe and another PX-6 as a transmitter.



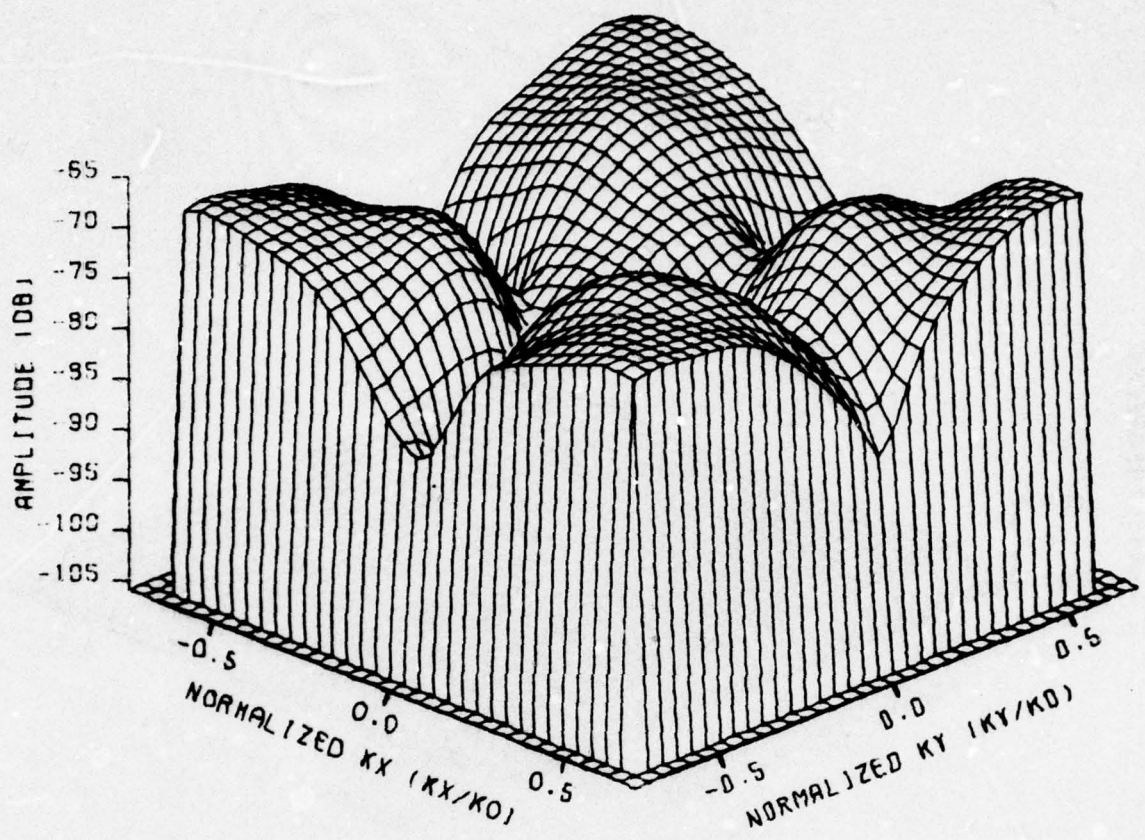
FILE 25, AMA(TRUE) FOR PX-6A MEAS. WITH PX-6B

Figure 20. Amplitude of vertical (parallel) component of measured plane wave spectrum obtained using one PX-6 as the probe and another PX-6 as a transmitter.



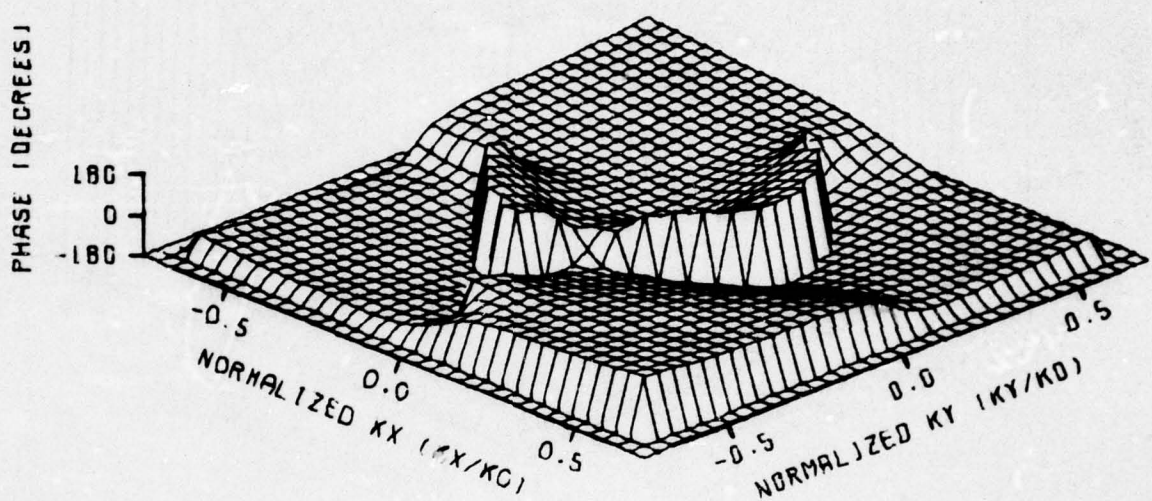
FILE 25. AMA(TRUE) FOR PX-6A MEAS. WITH PX-6B

Figure 21. Phase of vertical (parallel) component of measured plane wave spectrum obtained using one PX-6 as the probe and another PX-6 as a transmitter.



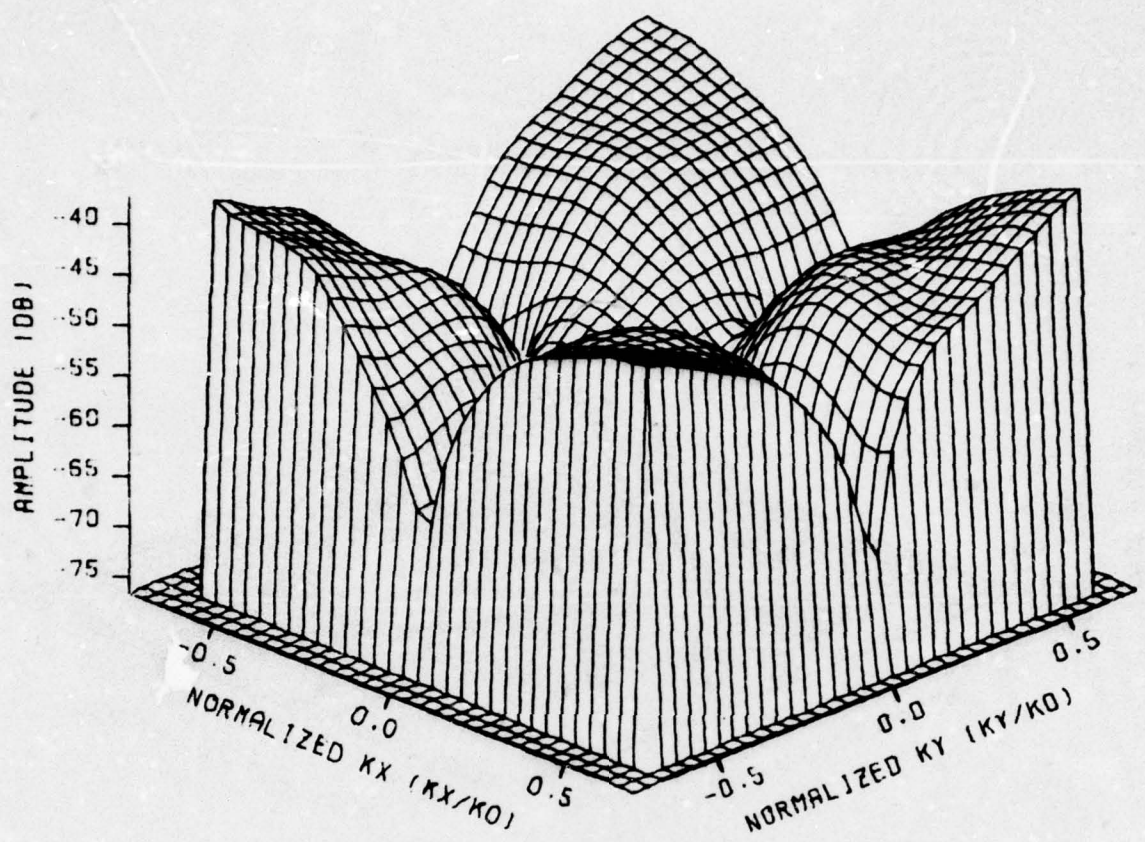
FILE 26. AMB(TRUE) FOR PX-6A MEAS. WITH PX-6B

Figure 22. Amplitude of horizontal (cross) component of measured plane wave spectrum obtained using one PX-6 as the probe and another PX-6 as a transmitter.



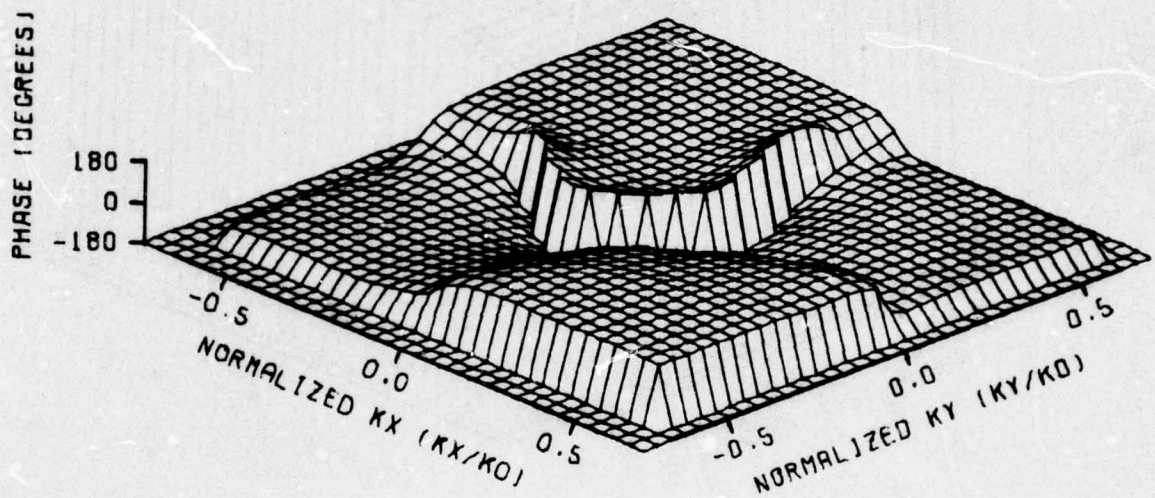
FILE 26, AMB(TRUE), FOR PX-6A MEAS. WITH PX-6B

Figure 23. Phase of horizontal (cross) component of measured plane wave spectrum obtained using one PX-6 as the probe and another PX-6 as a transmitter.



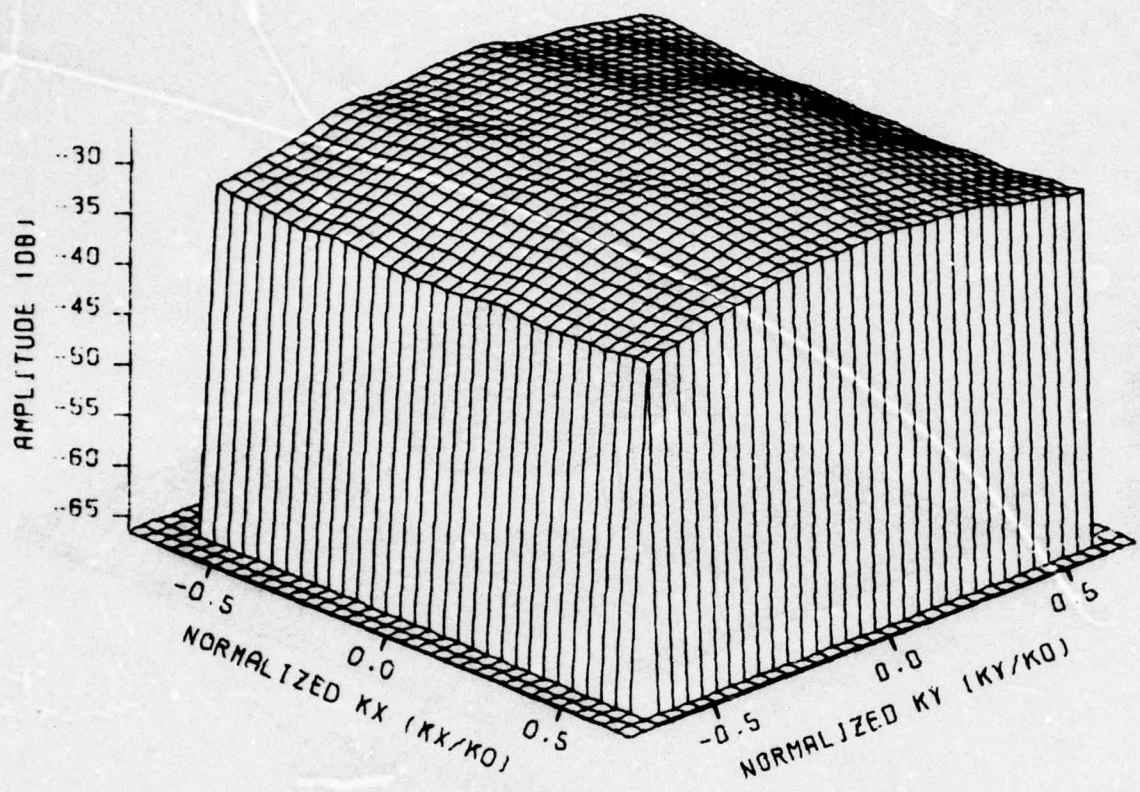
FILE 904, APX FOR PX-6

Figure 24. Amplitude of x-component of plane wave spectrum for probe PX-6
at 9 GHz.



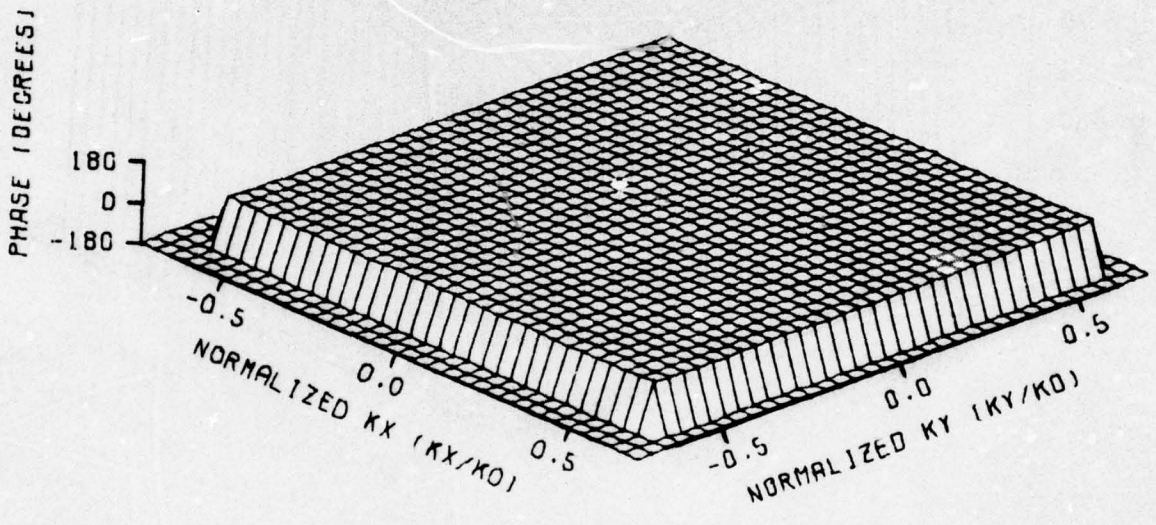
FILE 904, APX FOR PX-6

Figure 25. Phase of x-component of plane wave spectrum for probe PX-6
at 9 GHz.



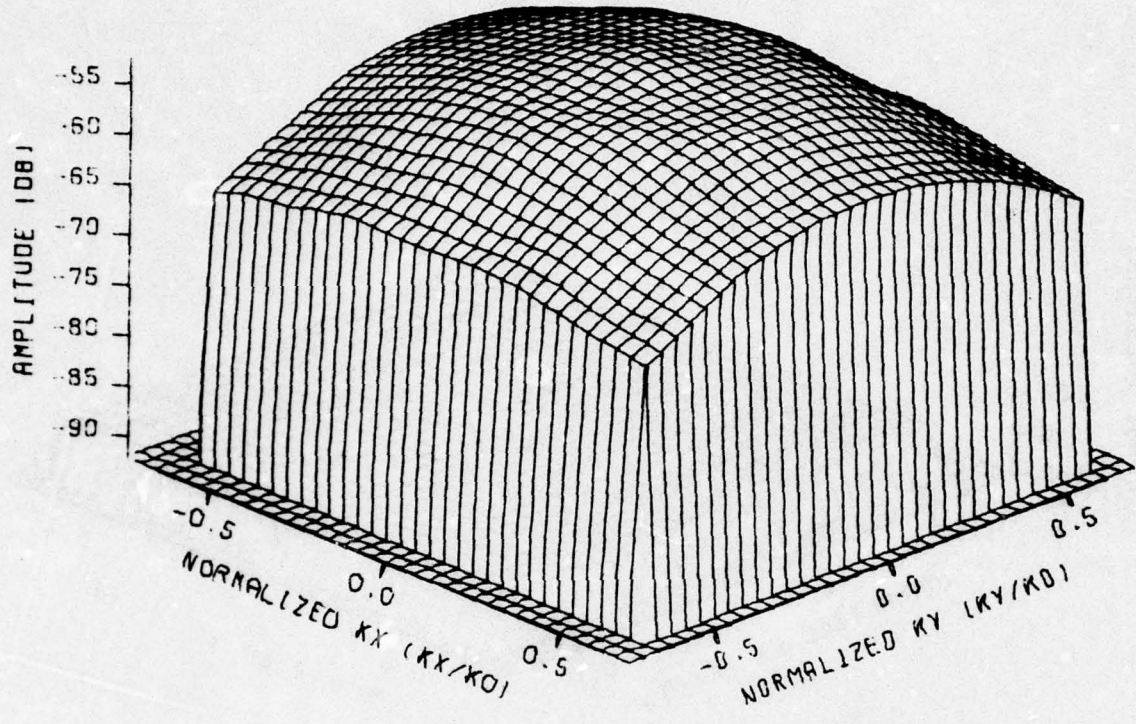
FILE 905, APY FOR PX-6

Figure 26. Amplitude of y-component of plane wave spectrum for probe PX-6 at 9 GHz.



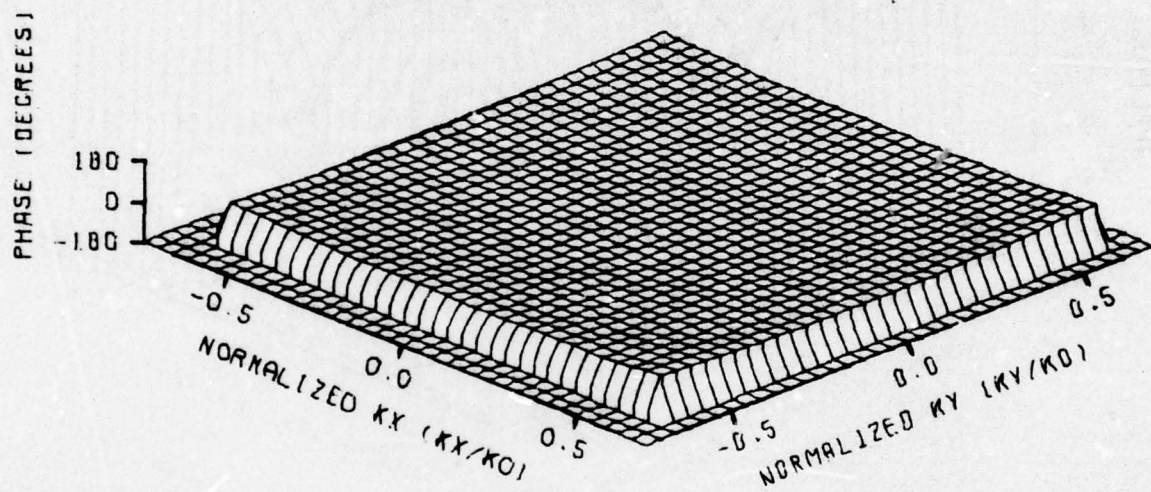
FILE 905, APY FOR PX-6

Figure 27. Phase of y-component of plane wave spectrum for probe PX-6
at 9 GHz.



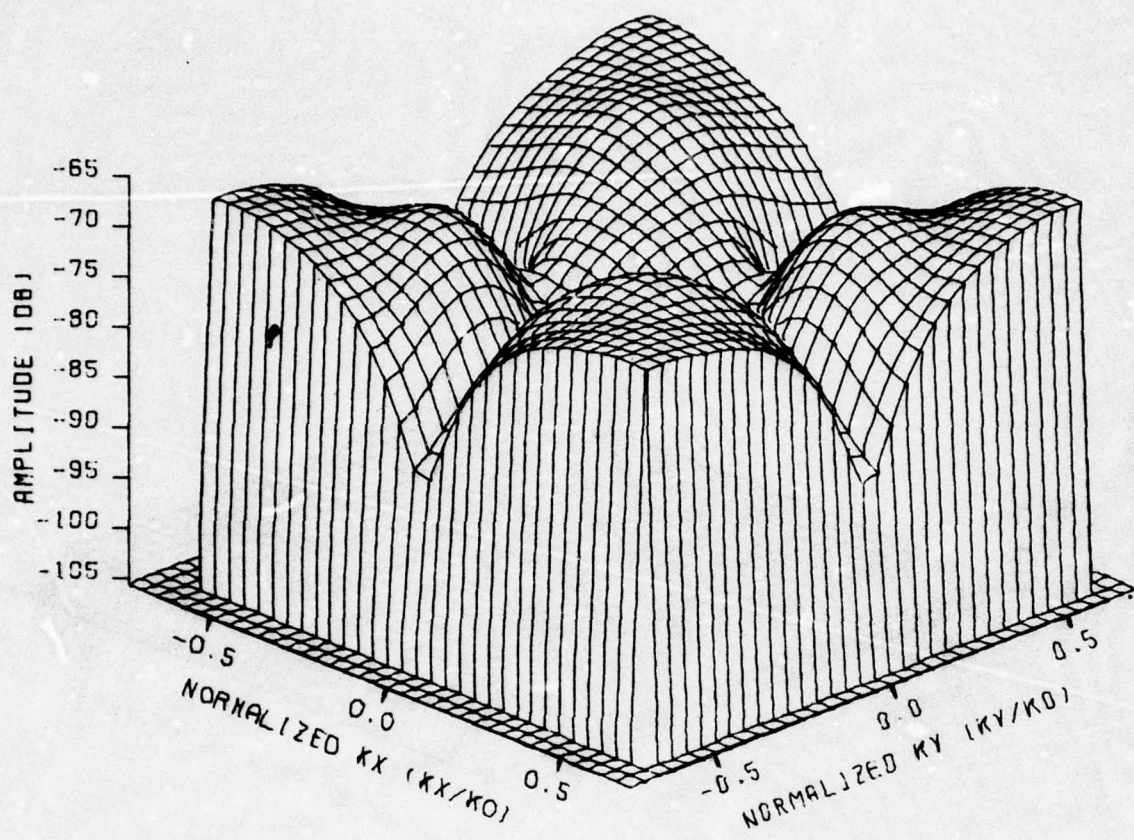
FILE 906. AMA(EST.1 FOR PX-6

Figure 28. Amplitude of predicted vertical (parallel) component of measured plane wave spectrum for probe PX-6 measuring another PX-6 that is transmitting. Spectrum of PX-6 was calculated using measured data.



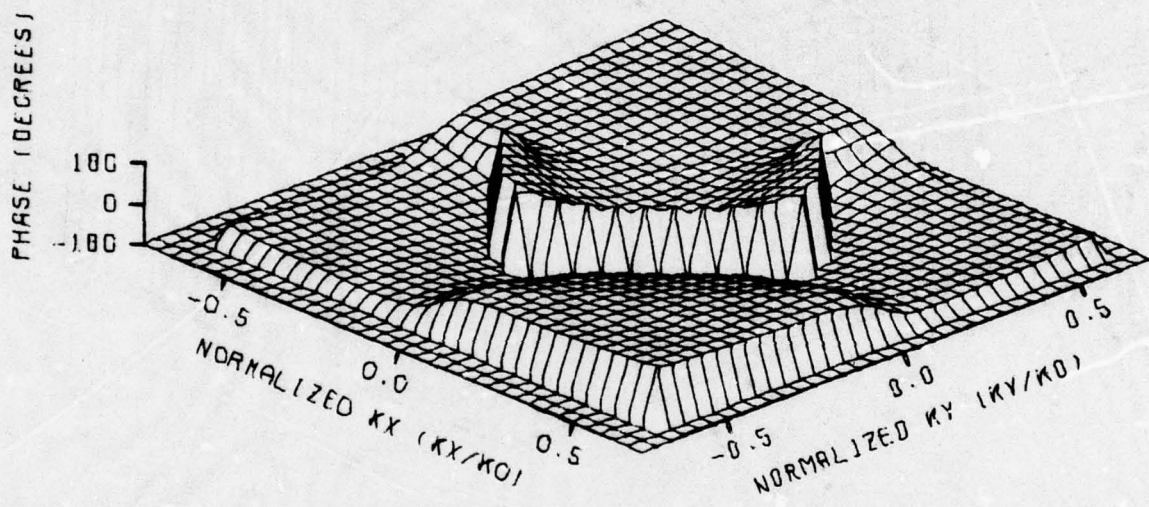
FILE 906. AMAIEST.I FOR PX-6

Figure 29. Phase of predicted vertical (parallel) component of measured plane wave spectrum for probe PX-6 measuring another PX-6 that is transmitting. Spectrum of PX-6 was calculated using measured data.



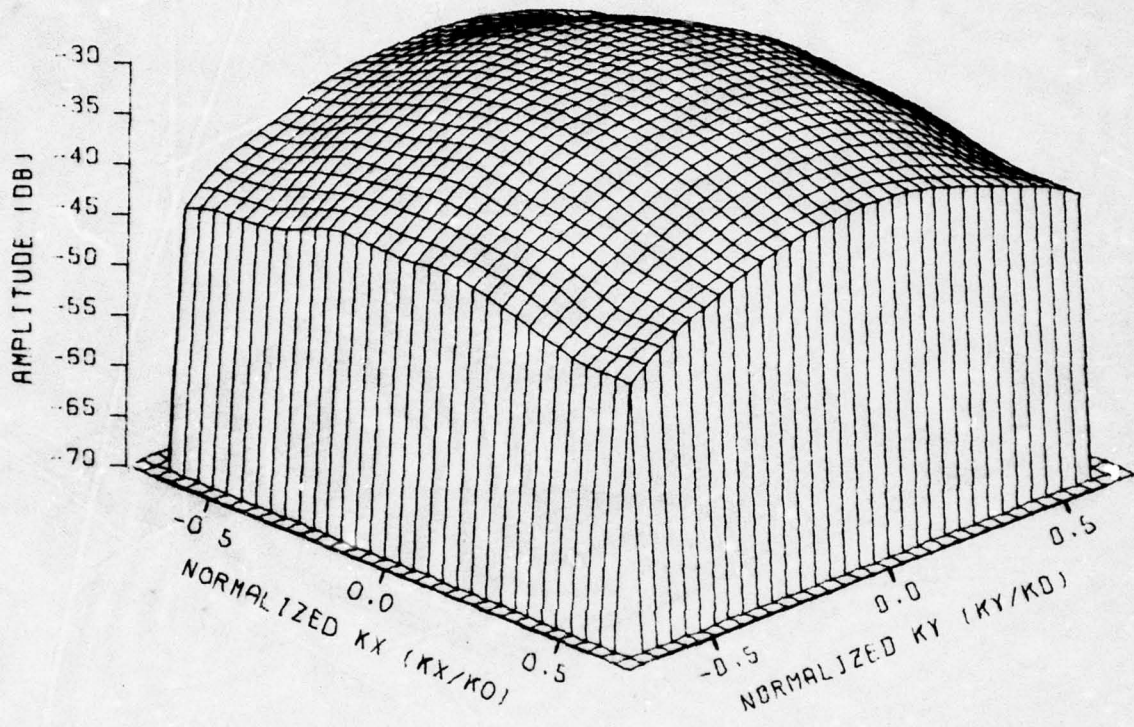
FILE 907. AMBLEST.I FOR PX-6

Figure 30. Amplitude of predicted horizontal (cross) component of measured plane wave spectrum for probe PX-6 measuring another PX-6 that is transmitting. Spectrum of PX-6 was calculated using measured data.



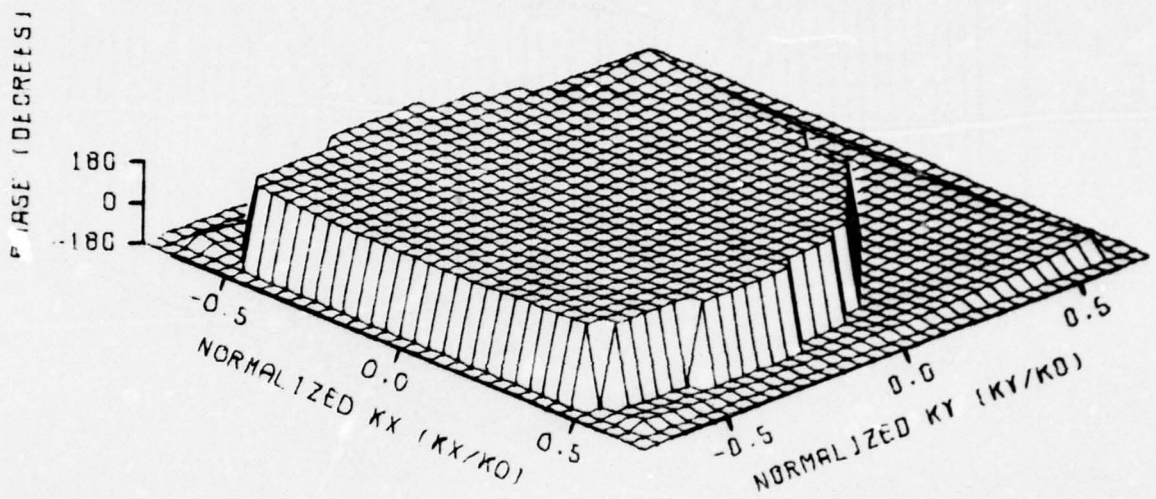
FILE 907. AMBIEST.I FOR PX-6

Figure 31. Phase of predicted horizontal (cross) component of measured plane wave spectrum for probe PX-6 measuring another PX-6 that is transmitting. Spectrum of PX-6 was calculated using measured data.



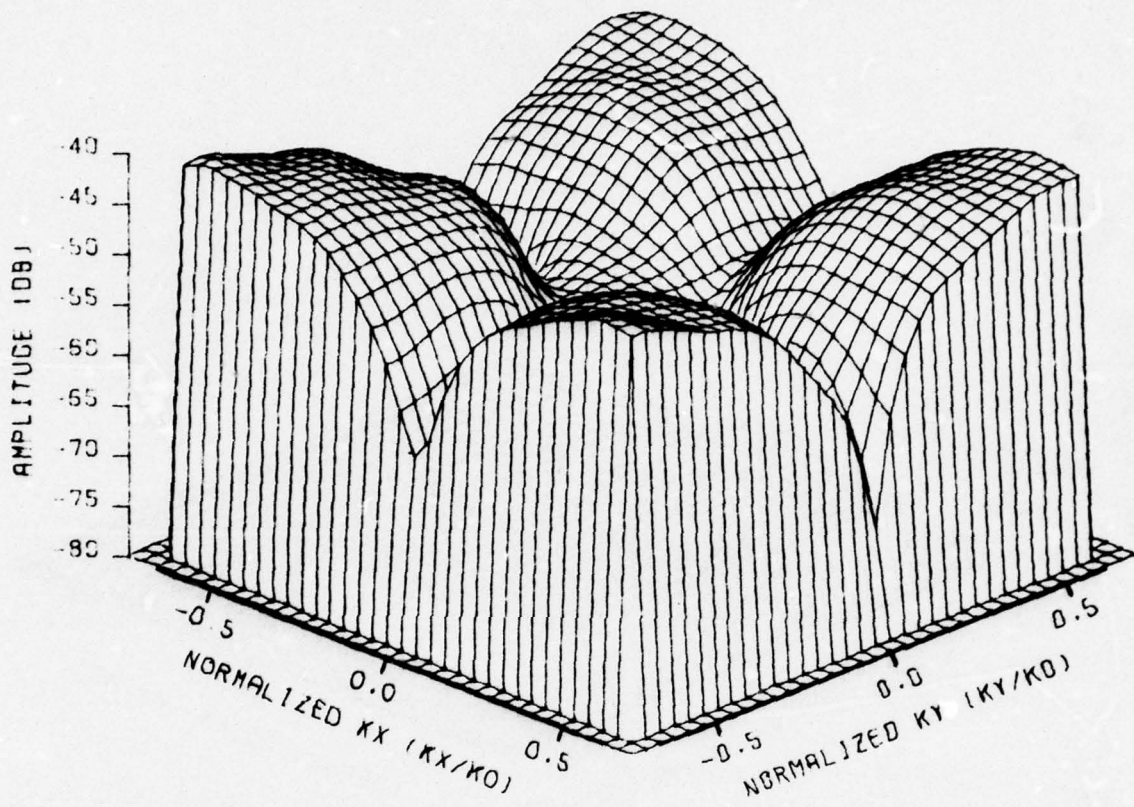
FILE 23, AMA(TRUE) FOR PX-5 MEAS. WITH PX-6

Figure 32. Amplitude of vertical (parallel) component of measured plane wave spectrum obtained using PX-6 as the probe and PX-5 as a transmitter.



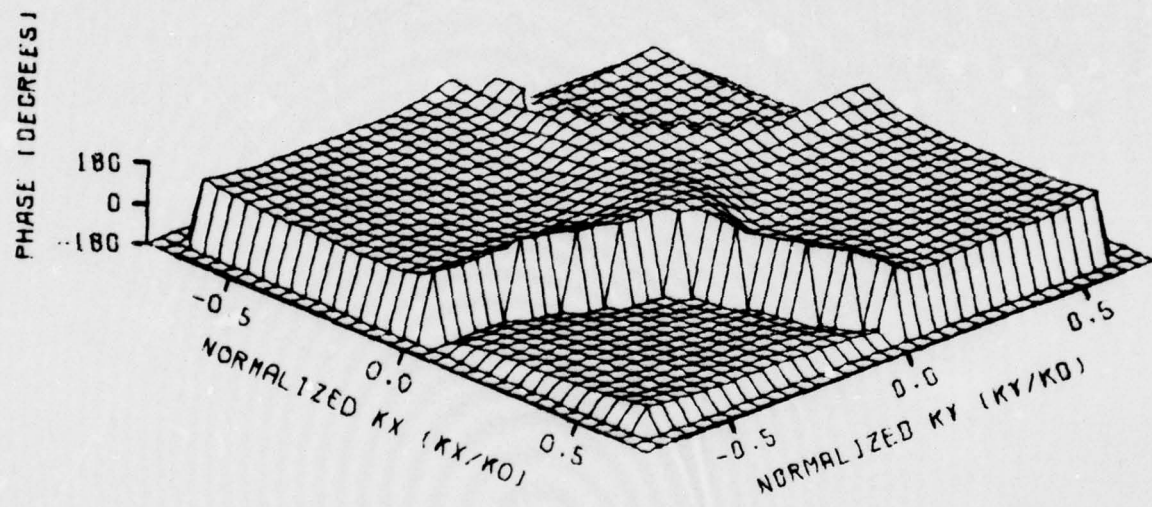
FILE 23. AMA(TRUE) FOR PX-5 MEAS. WITH PX-6

Figure 33. Phase of vertical (parallel) component of measured plane wave spectrum obtained using PX-6 as the probe and PX-5 as a transmitter.



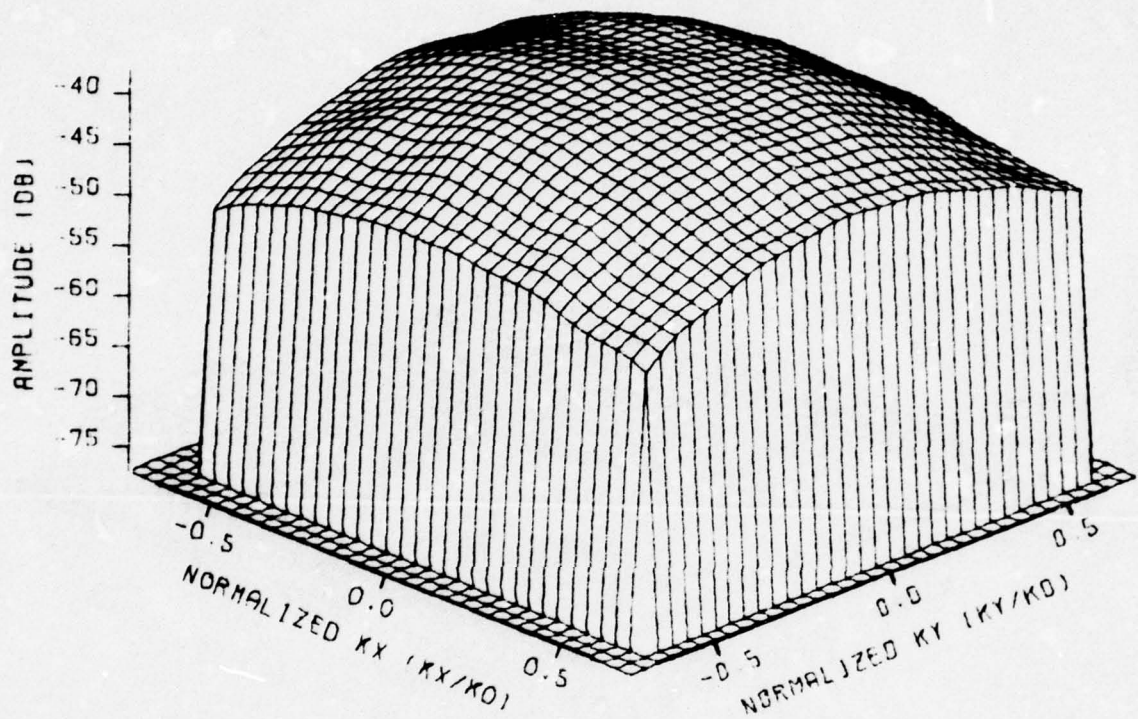
FILE 24, AMBI(TRUE) FOR PX-5 MEAS. WITH PX-6

Figure 34. Amplitude of horizontal (cross) component of measured plane wave spectrum obtained using PX-6 as the probe and PX-5 as a transmitter.



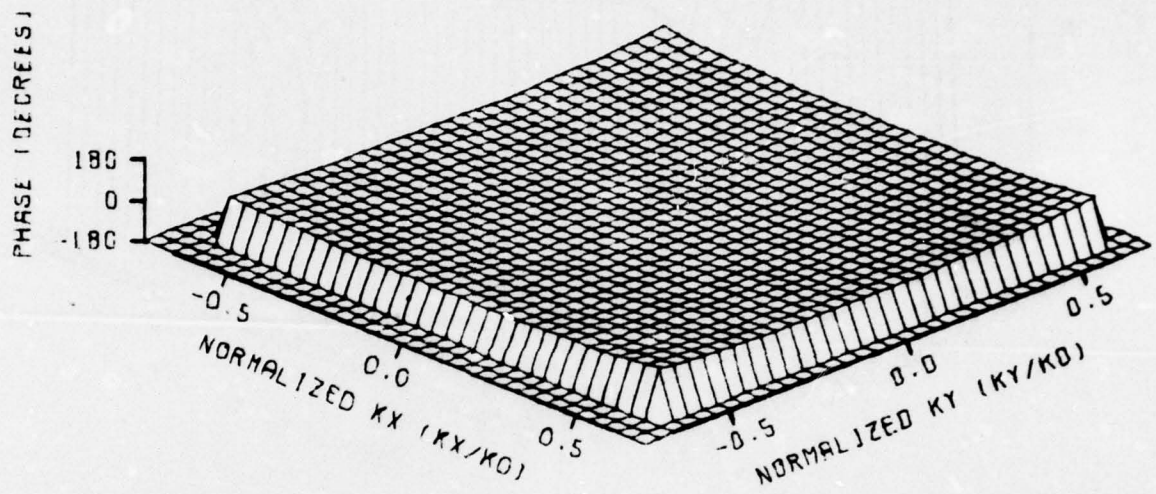
FILE 24. AMB(TRUE) FOR PX-5 MEAS. WITH PX-6

Figure 35. Phase of horizontal (cross) component of measured plane wave spectrum obtained using PX-6 as the probe and PX-5 as a transmitter.



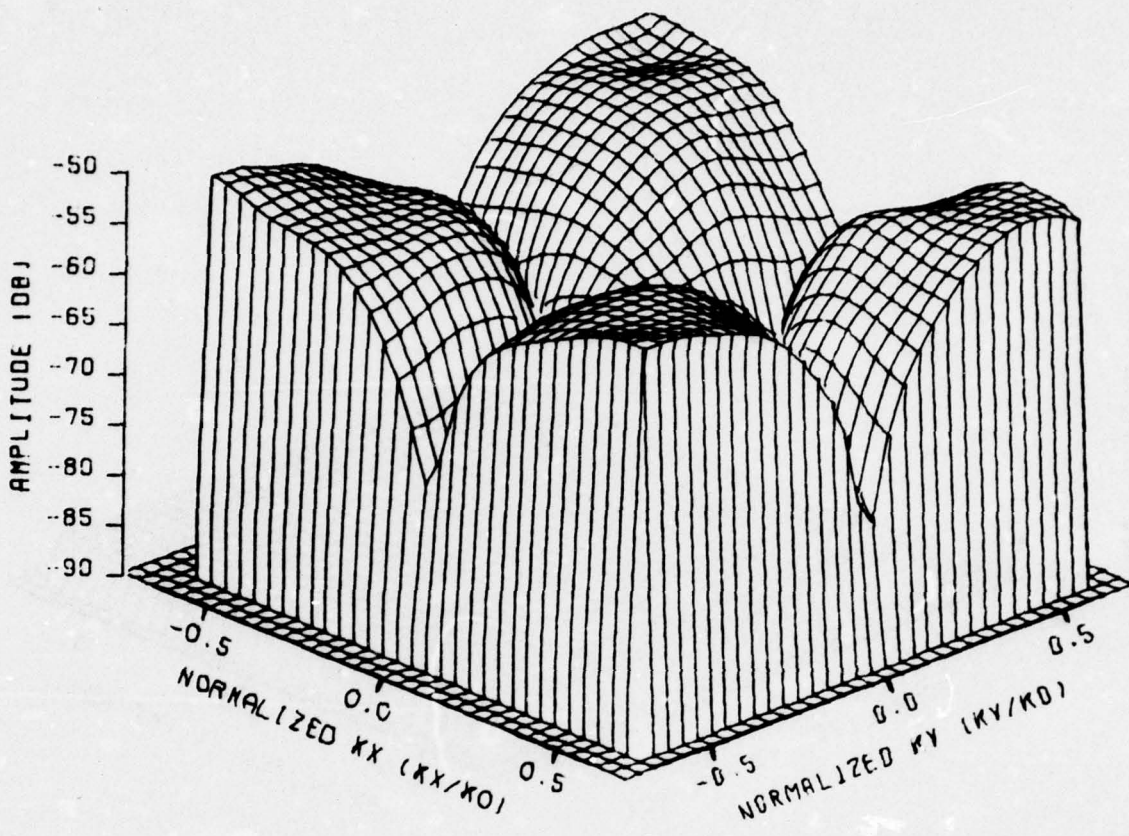
FILE 910, AMA(EST.1 FOR PX-5 MEAS. WITH PX-6

Figure 36. Amplitude of predicted vertical (parallel) component of measured plane wave spectrum for probe PX-6 measuring PX-5 as a transmitter. The spectra of PX-5 and PX-6 were calculated using measured data.



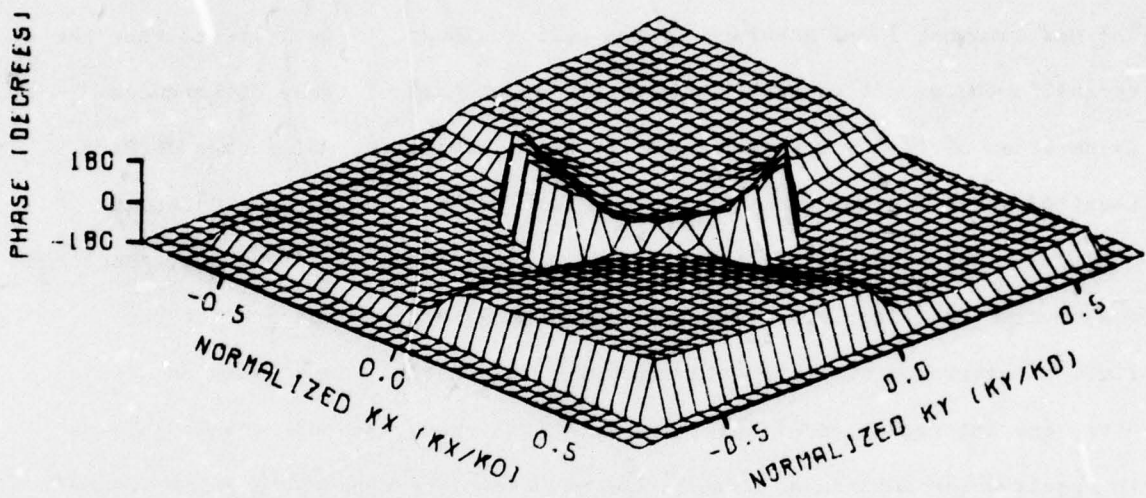
FILE 910, AMA(EST.) FOR PX-5 MEAS. WITH PX-6

Figure 37. Phase of predicted vertical (parallel) component of measured plane wave spectrum for probe PX-6 measuring PX-5 as a transmitter. The spectra of PX-5 and PX-6 were calculated using measured data.



FILE 911. AMB(EST.1 FOR PX-5 MEAS. WITH PX-6

Figure 38. Amplitude of predicted horizontal (cross) component of measured plane wave spectrum for probe PX-6 measuring PX-5 as a transmitter. The spectra of PX-5 and PX-6 were calculated using measured data.



FILE 911. AMB(EST.) FOR PX-5 MEAS. WITH PX-6

Figure 39. Phase of predicted horizontal (cross) component of measured plane wave spectrum for probe PX-6 measuring PX-5 as a transmitter. The spectra of PX-5 and PX-6 were calculated using measured data.

The preceding comparisons have shown that the new probe characterization technique does predict the probe spectrum for both parallel- and cross-polarization both on and off the principal planes. Accuracy of the technique is difficult to assess directly since no comparison probe data was available. A comparison between predicted and actual measured spectra of one probe measuring another showed the following: the parallel polarized component, i.e. AMA, generally agreed to within 0.5 dB in amplitude and 6° in phase, while the cross polarized component, i.e. AMB, generally agreed to within 1.5 dB in amplitude and 15° in phase near the peaks of the cross polarized pattern and had somewhat lower accuracy in the null regions. It is believed that the errors in the predicted probe spectra are about half of these differences. Calculation of PX-5's spectrum required about 4 minutes, while that of PX-6 required about 5 minutes on the Georgia Tech CYBER 70 computer. Obtaining comparable measurements using Joy's approach [2] requires a separate spherical measurement facility, measuring and recording spherical component of the fields, conversion of these data expressed in spherical components to k-space data, and interpolation of this data to obtain evenly spaced k-space data as is required for subsequent usage. The new technique appears to offer advantages over the old technique in overall system cost through elimination of both the need for a spherical positioning system and the need for many of the tedious calculations required by the older method.

SECTION V

GLINT MEASUREMENTS

The validity of the Plane-Wave Spectrum (or Modal Expansion) Technique for near-zone radar cross-section application was demonstrated under a previous contract [9] at Georgia Tech. Simple geometrical shapes such as flat plates as well as an F-100 model aircraft were measured using simple waveguide horn antennas. It was demonstrated that the Plane-Wave Spectrum Technique could predict near-zone radar cross-section signals for these simple antennas. The purpose of the present study is to validate the technique with more complicated antennas as are typical for realistic missile seekers. The apparatus used for this purpose is similar to that used in the previous contract [9]. A horizontally polarized plane wave illuminator is used, as illustrated in Figure 40, to illuminate the model aircraft with a plane wave. Reflected energy from the target is measured by the probe antenna moving on a planar surface. The previously measured probe characteristics are used to remove probe effects from the near-field data, thus obtaining the scattered field due to the target by itself. The signal received by a tracker antenna can be computed using the measured scattered characteristics of the target and the previously measured characteristics of the tracker antenna. The plane wave illuminator is a six-foot diameter paraboloidal reflector with only the upper half illuminated to avoid blockage due to the feed. A phase locked klystron operating at 9.0 GHz was used as the signal source. Near-field data is obtained using an XYZ positioner developed by Scientific Atlanta that is capable of moving a probe over a 100-inch by 100-inch plane with an accuracy of ± 0.005 inches. The receiver portion of the system consists of a Scientific-Atlanta phase-amplitude receiver. The measurement process has been automated by Georgia Tech to permit mini-computer control of the entire data measurement process.

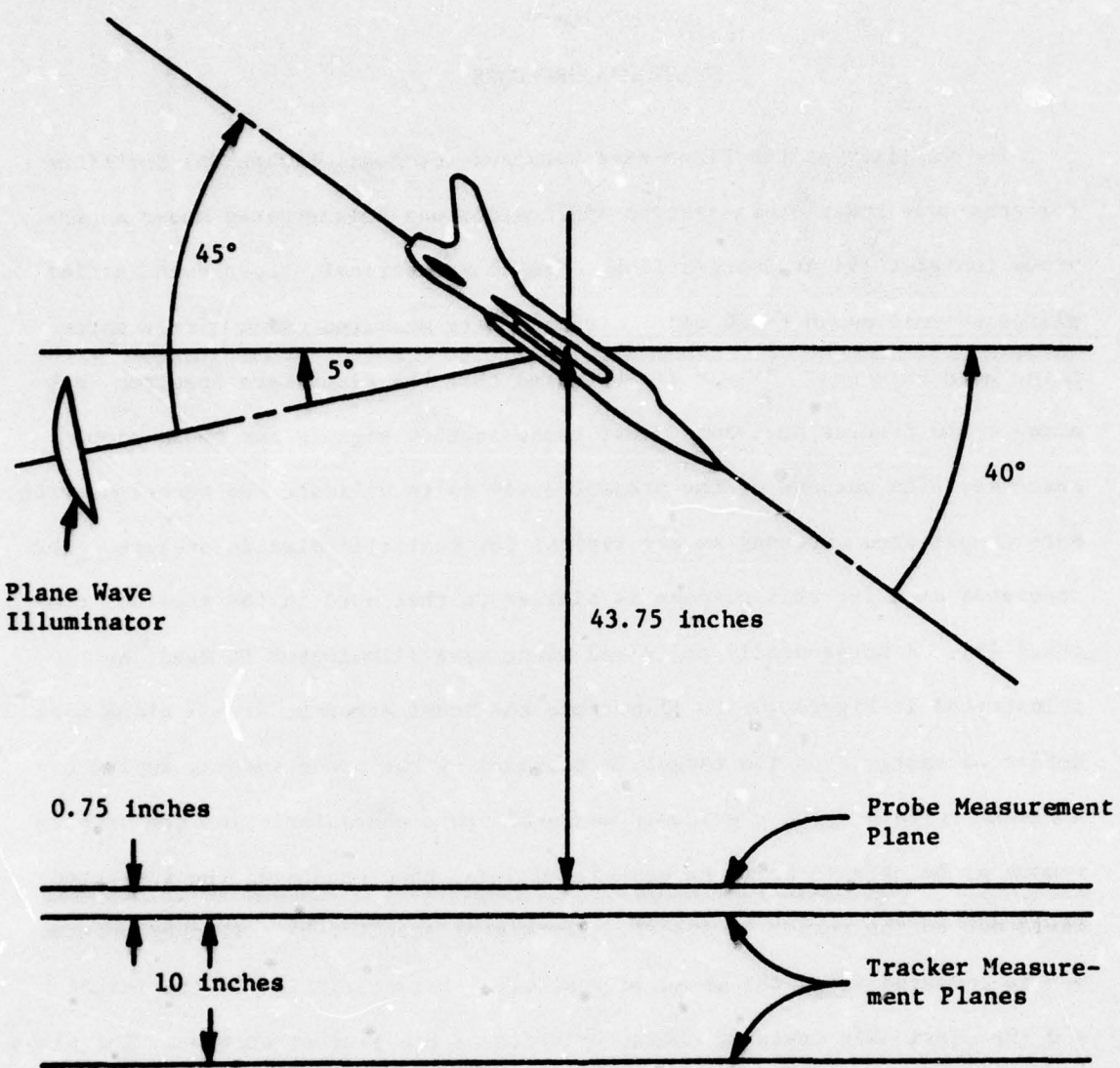


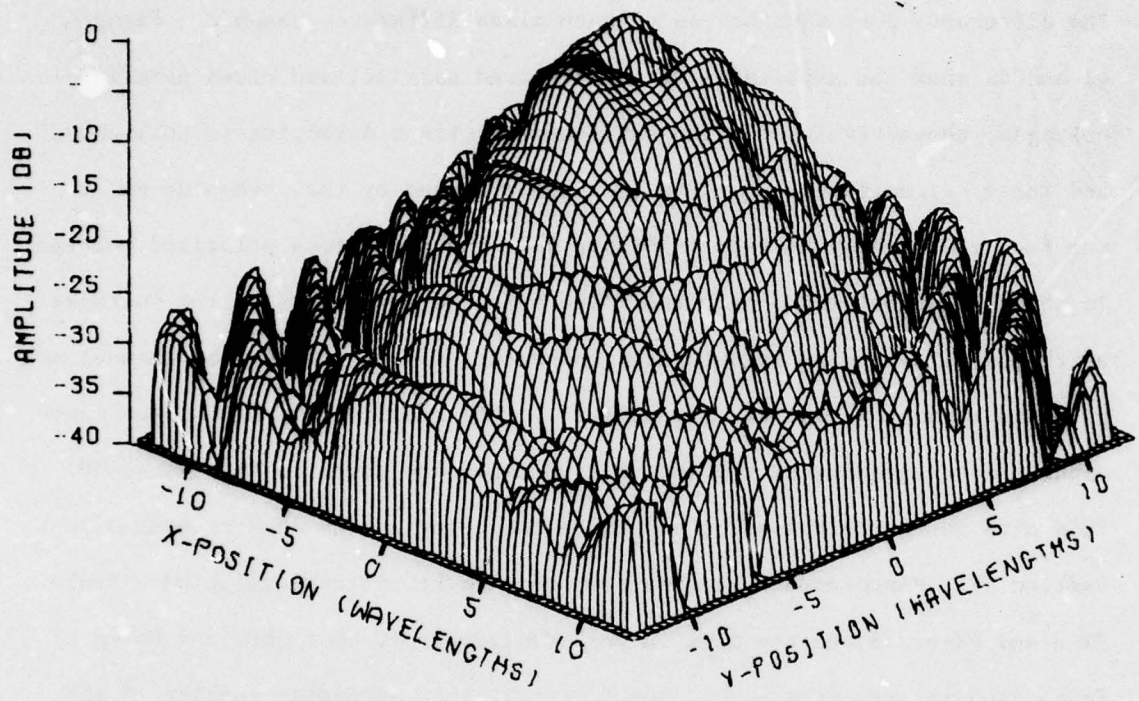
Figure 40. Geometry for flyby measurements at 9.0 GHz of 1/33 scale F-105 model aircraft.

A. Tracker Measurements

The tracking antenna used in these measurements is a one-foot diameter paraboloid with a single-plane monopulse feed at its focal point. The tracker was mounted for characterization purposes so that it was vertically polarized and such that the waveguide run to the feed went over the top of the dish. The difference port was then an azimuth plane difference channel. Figures 41 and 42 show the amplitudes of the measured parallel and cross polarized voltages, respectively, for the sum channel. The x direction is horizontal and the +y direction is up. The blockage produced by the waveguide run to the feed can clearly be seen in Figure 41. The peak cross polarized voltage is about 14 dB below the parallel. The measured amplitudes of the voltages of the parallel and cross polarized components for the difference channel are given in Figures 43 and 44, respectively. The amplitudes of the plane wave spectra corresponding to the measured voltages are given in Figures 45-48. This data was corrected using the probe characterization data described in Section IV. Measurements were made of the tracker antenna using both Probe PX-5 and PX-6. Since the data is very similar, only that obtained using Probe PX-5 is presented here. The fact that the calculated spectra of the tracker are nearly identical using the two sets of probe data indicates that the probe characterization data is very good. Removing probe characteristics produces the plane wave spectra of the seeker shown in Figures 49-52. The cross polarized signal of the sum channel is about 26 dB below the parallel polarized sum channel. For the difference channel the cross polarized signal is down nearly 20 dB for the angular sector plotted.

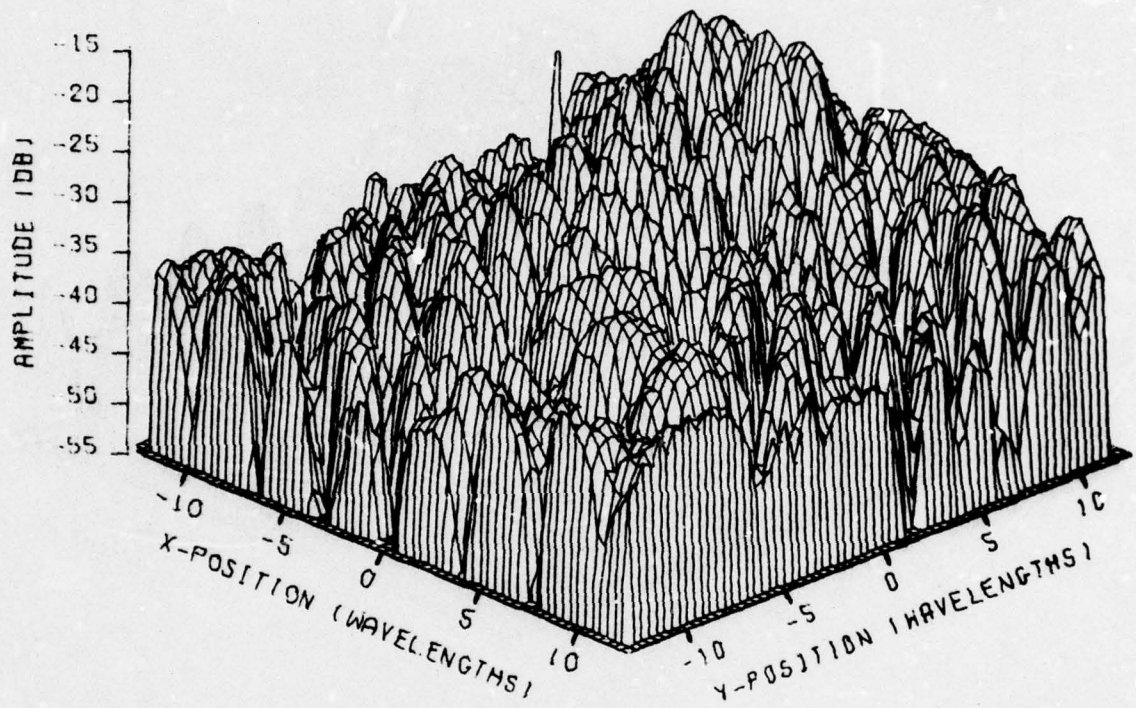
B. Target Measurements

Fly-by measurements were made on a model of an F-105 aircraft using a single plane (two horn) monopulse tracking antenna. Figure 40 illustrates



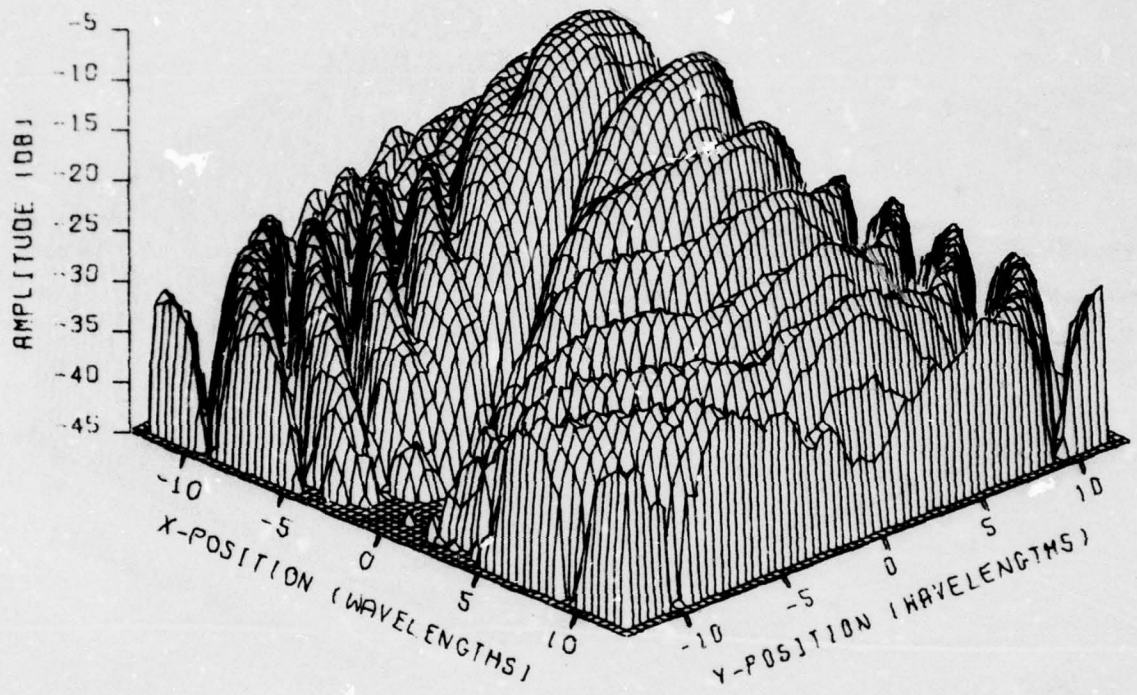
FILE 7. VA (PARALLEL) FOR SUM MEAS. WITH PX-5

Figure 41. Amplitude of vertical (parallel) component of measured voltage for sum channel of one-foot tracker at 9 GHz using probe PX-5.



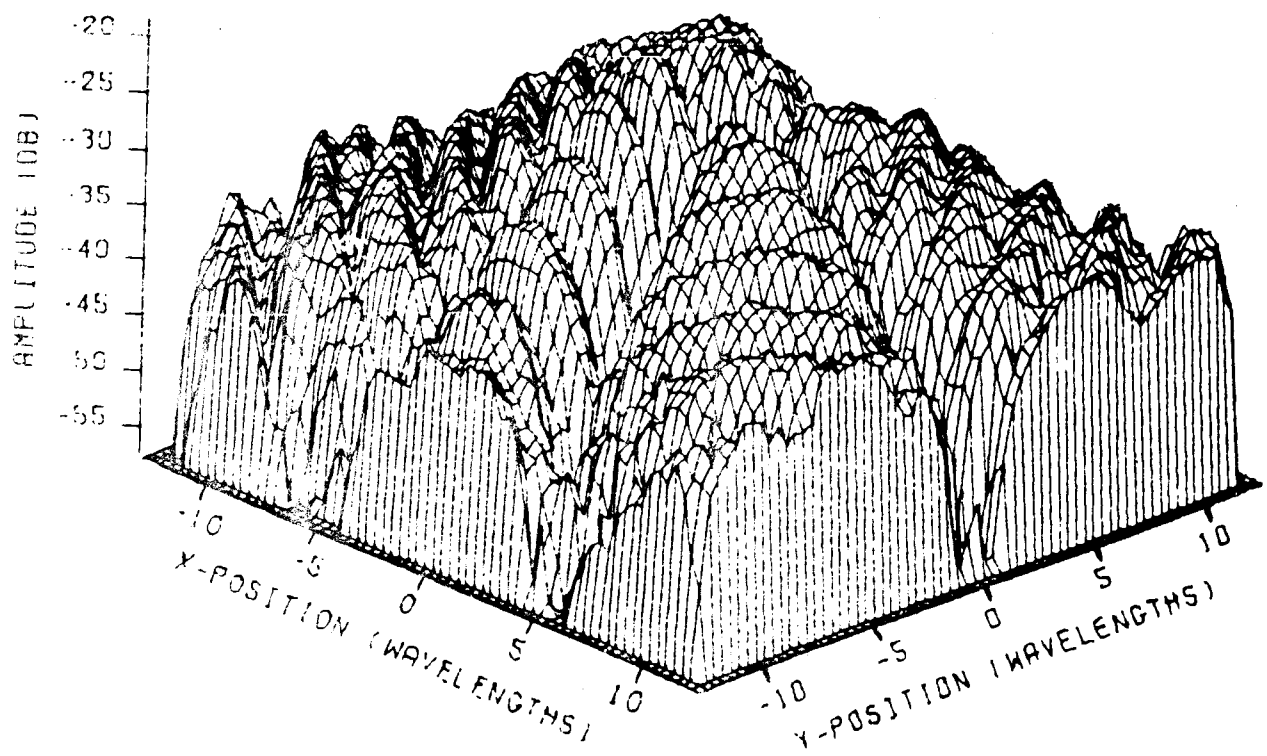
FILE 8. VB (CROSS) FOR SUM MEAS. WITH PX-5

Figure 42. Amplitude of horizontal (cross) component of measured voltage for sum channel of one-foot tracker at 9 GHz using probe PX-5.



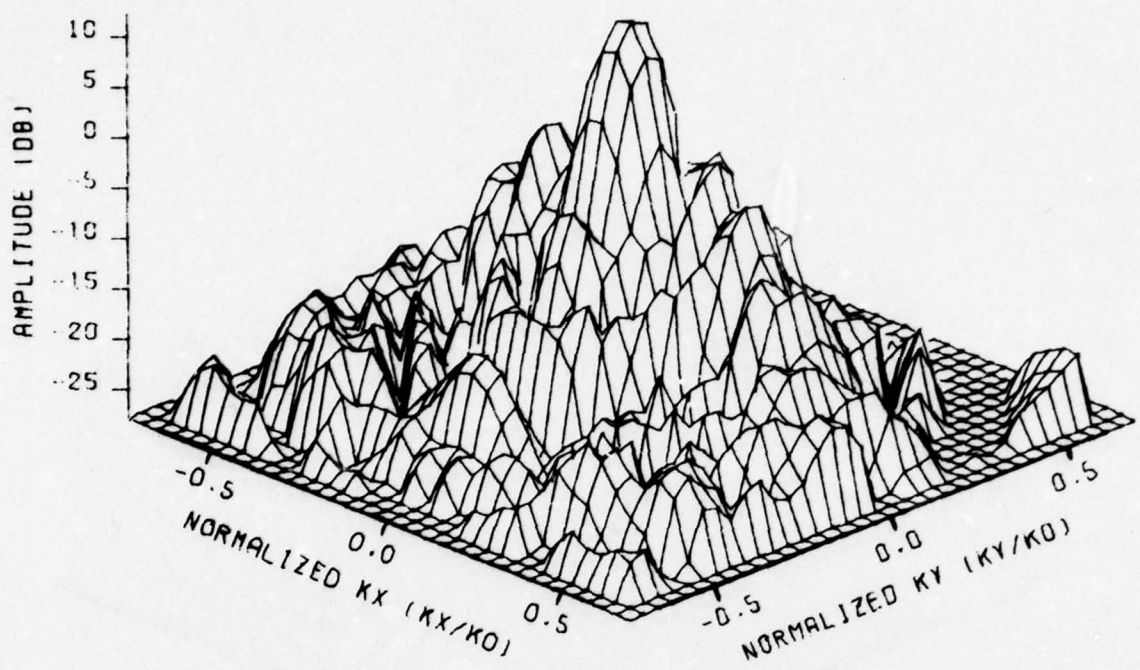
FILE 9, VA (PARALLEL) FOR AZ. DIFF. MEAS. WITH PX-5

Figure 43. Amplitude of vertical (parallel) component of measured voltage for difference channel of one-foot tracker at 9 GHz using probe PX-5.



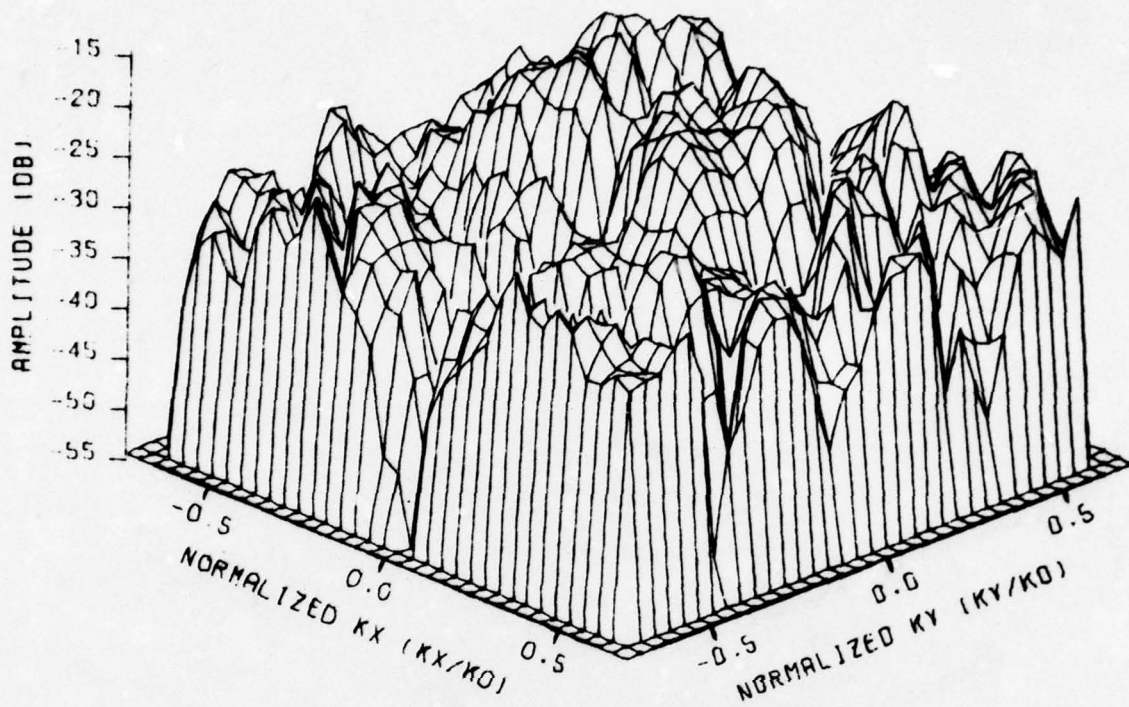
FILE 10, VB (CPSS) FOR AZ. DIFF. MEAS. WITH PX-5

Figure 44. Amplitude of horizontal (cross) component of measured voltage for difference channel of one-foot tracker at 9 GHz using probe PX-5.



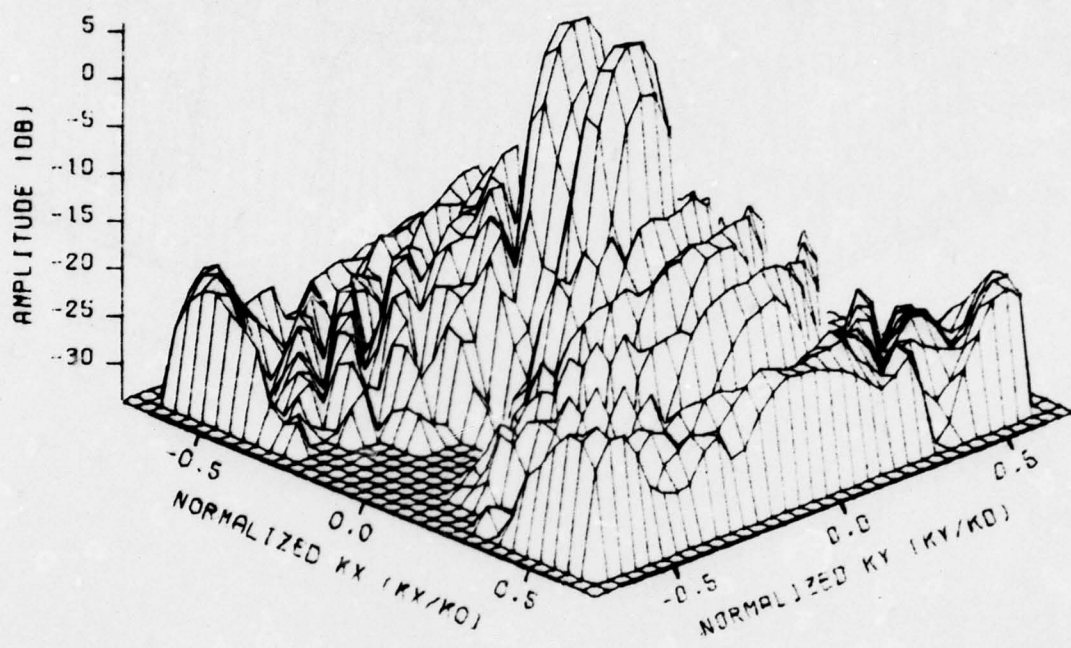
FILE 27. AMA FOR SUM PARALLEL USING PX-5

Figure 45. Amplitude of vertical (parallel) component of measured plane wave spectrum for sum channel of one-foot tracker at 9 GHz using probe PX-5.



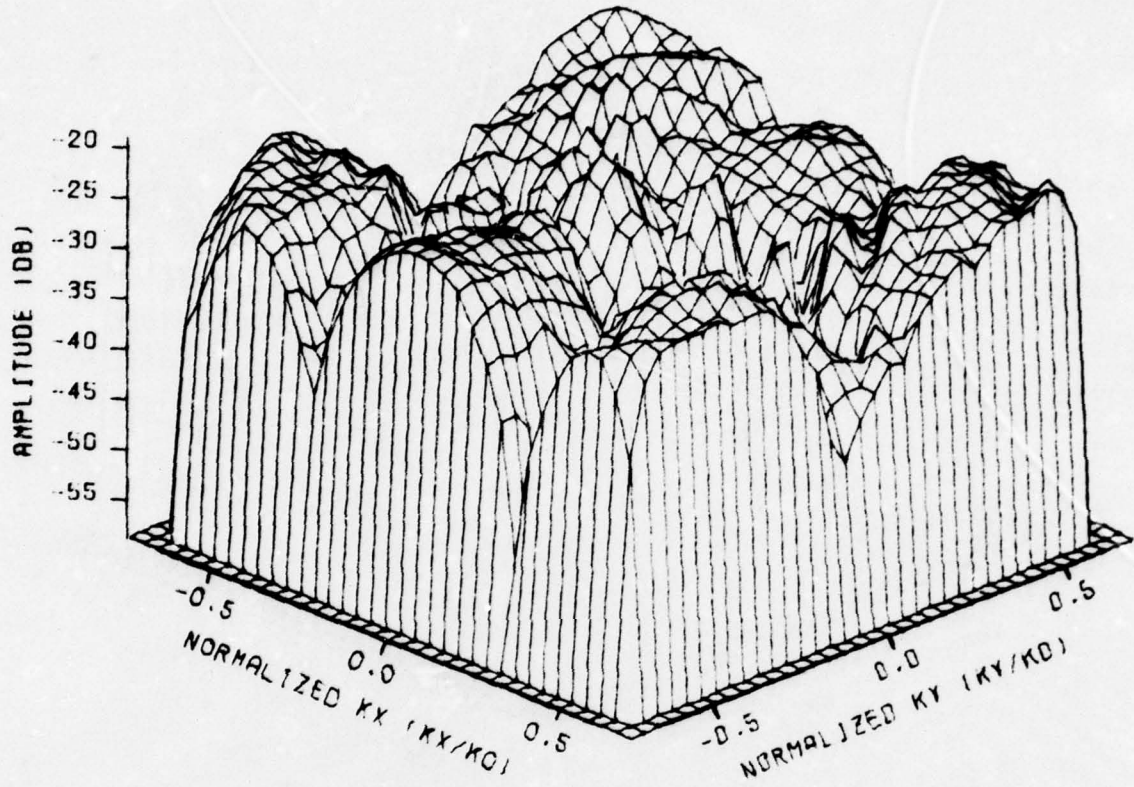
FILE 28. AMB FOR SUM (CROSS) USING PX-5

Figure 46. Amplitude of horizontal (cross) component of measured plane wave spectrum for sum channel of one-foot tracker at 9 GHz using probe PX-5.



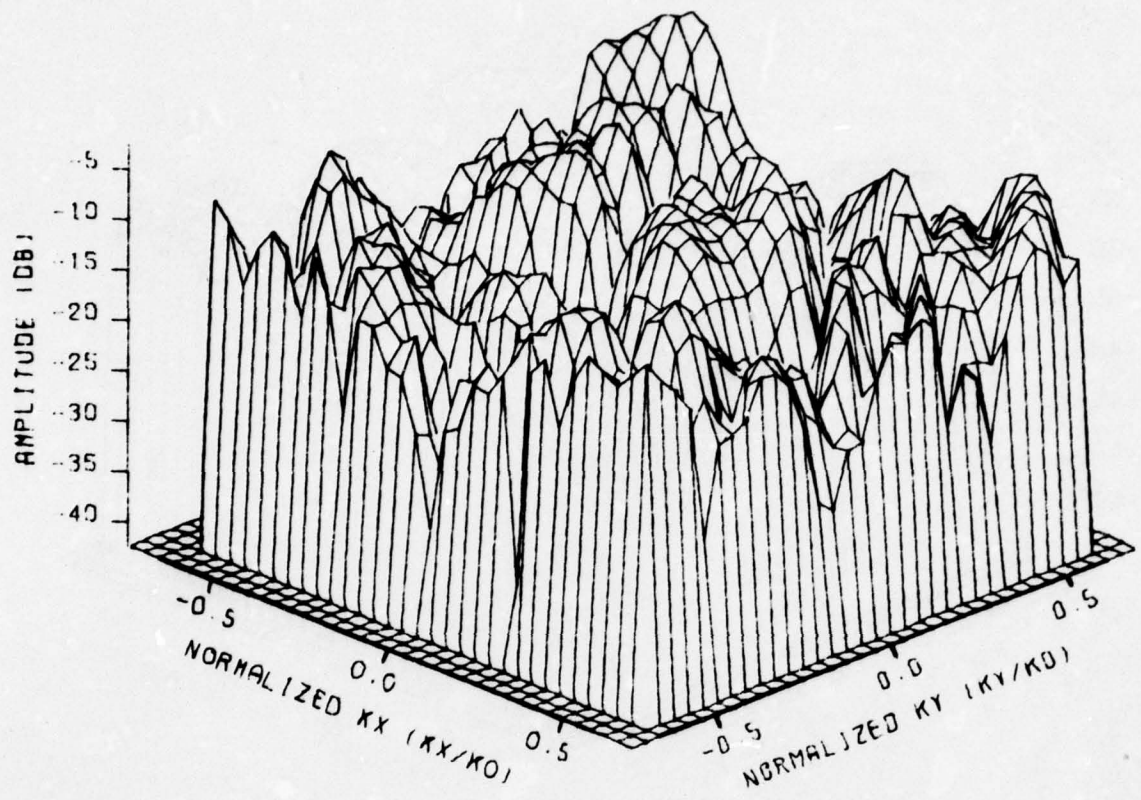
FILE 29. AMA FOR AZ. DIFF. (PARALLEL POL.) USING PX-5

Figure 47. Amplitude of vertical (parallel) component of measured plane wave spectrum for difference channel of one-fo tracker at 9 GHz using probe PX-5.



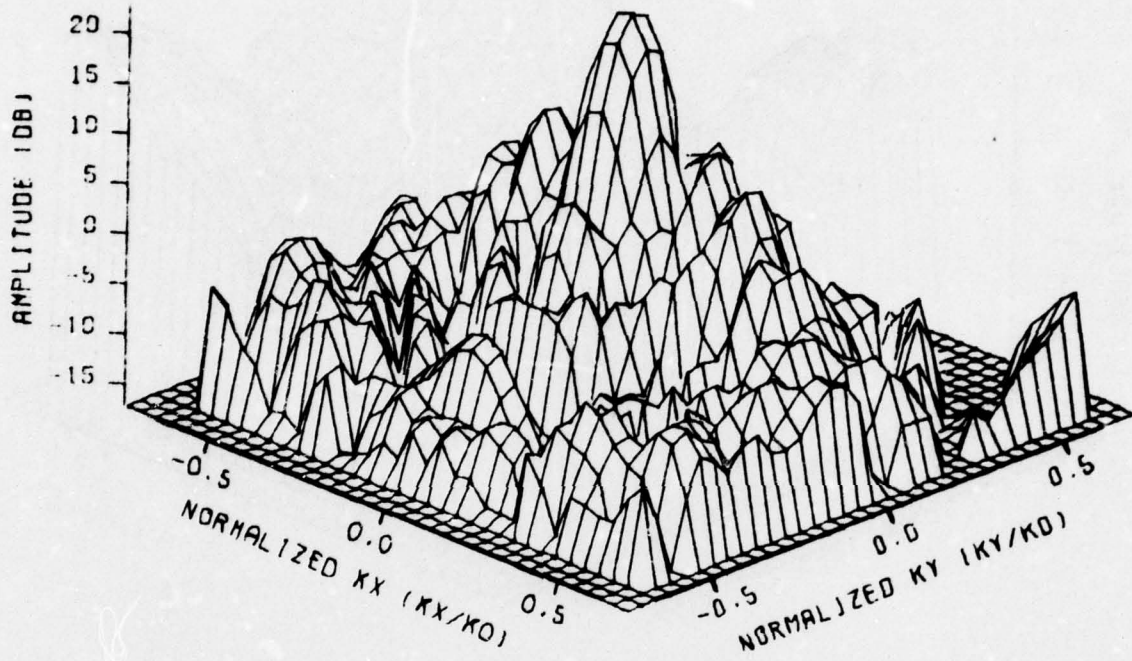
FILE 30. AMB FOR AZ. DIFF. (CROSS POL.) USING PX-5

Figure 48. Amplitude of horizontal (cross) component of measured plane wave spectrum for difference channel of one-foot tracker at 9 GHz using probe PX-5.



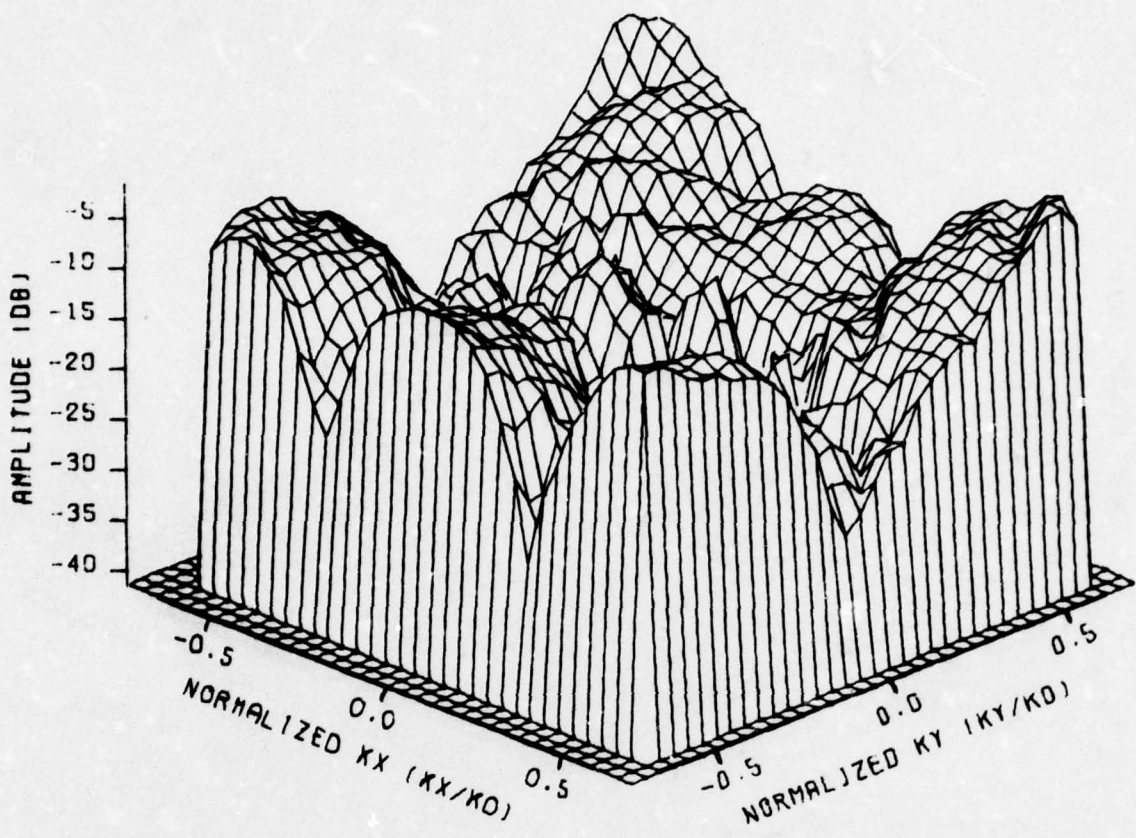
FILE 41. AAX FOR SUM USING PX-5

Figure 49. Amplitude of x-component of plane wave spectrum for sum channel of one-foot tracker at 9 GHz.



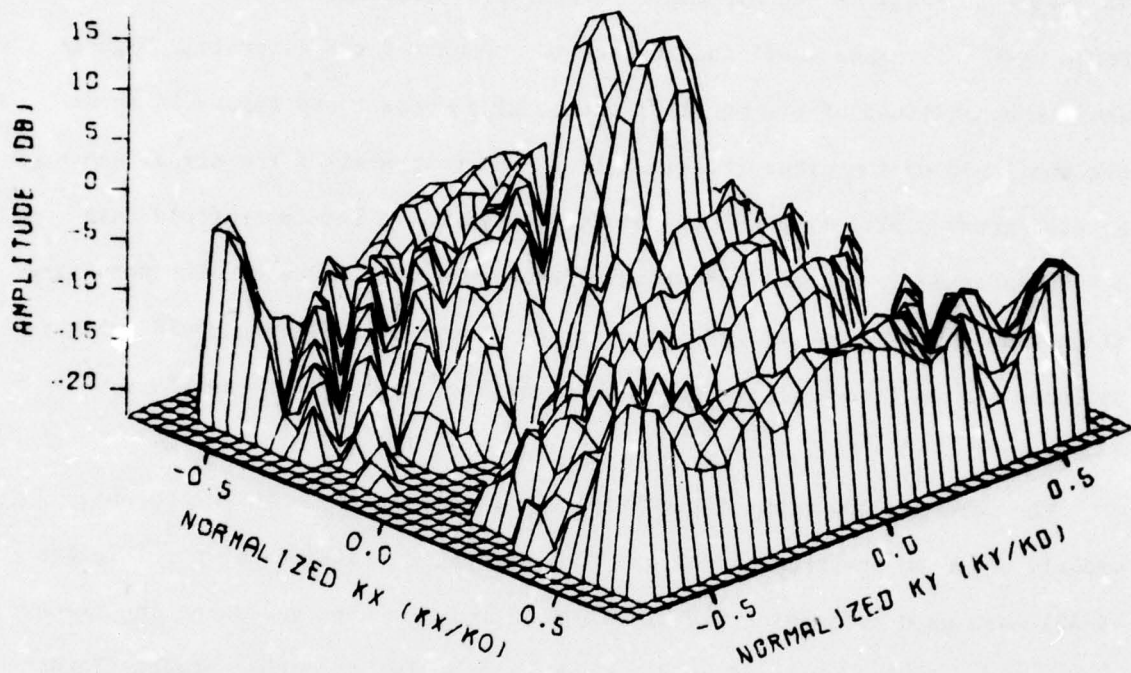
FILE 42, AAY FOR SUM USING PX-5

Figure 50. Amplitude of y-component of plane wave spectrum for sum channel of one-foot tracker at 9 GHz.



FILE 43. AAX FOR AZ. DIFF. USING PX-5

Figure 51. Amplitude of x-component of plane wave spectrum for difference channel of one-foot tracker at 9 GHz.

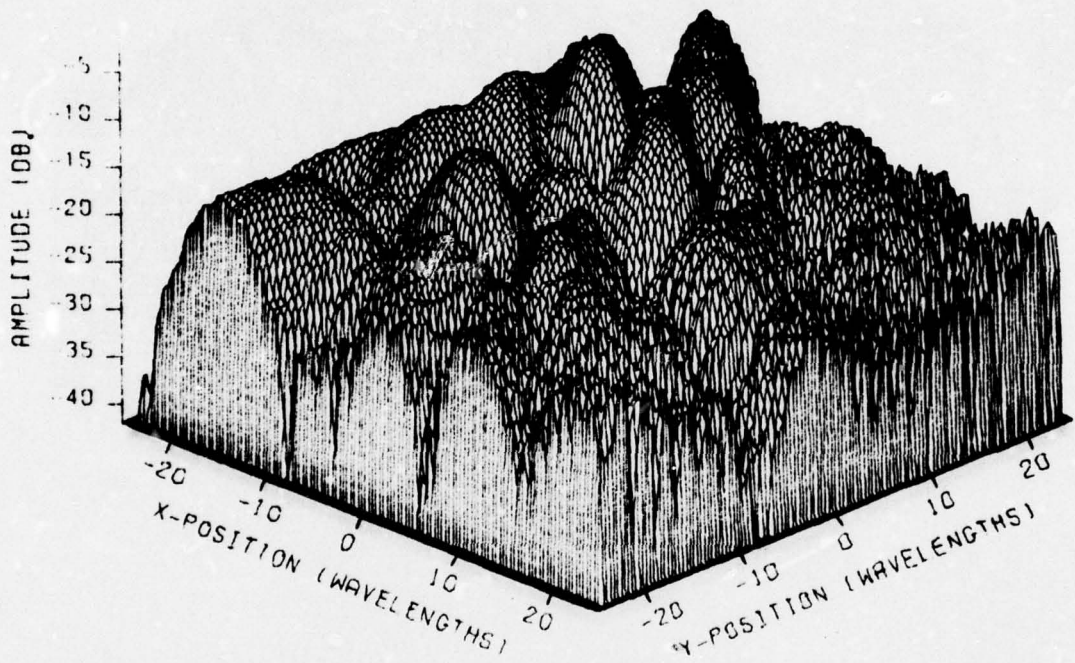


FILE 44, ARRAY FOR AZ. DIFF. USING PX-5

Figure 52. Amplitude of y-component of plane wave spectrum for difference channel of one-foot tracker at 9 GHz.

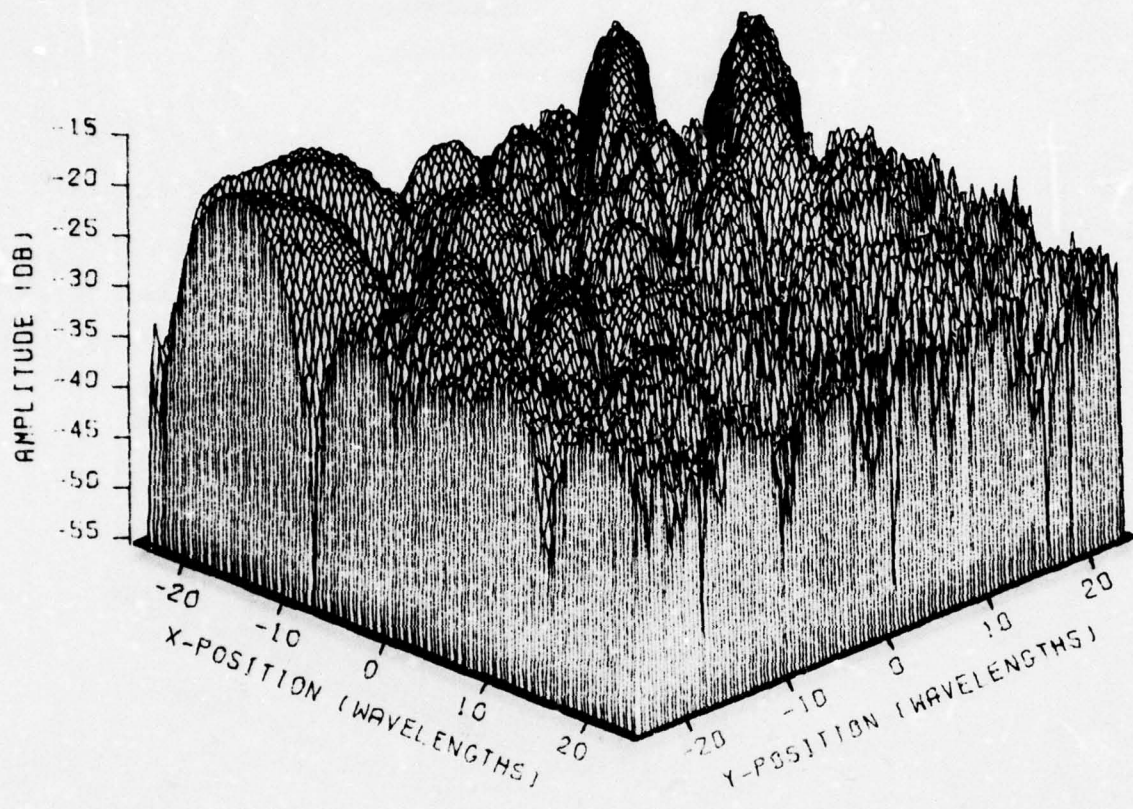
the geometry used in the measurements. The 1/33 scale model of the F-105 aircraft was illuminated at 9 GHz using an offset fed, parabolic reflector to generate a plane wave illumination on the model aircraft. The illuminator was horizontally polarized and illuminated the belly of the aircraft. The F-105 was mounted with its wings vertical and was illuminated at an angle of 45° below the tail of the aircraft. Near-field measurements were made using Probe PX-5 on a plane 43.75 inches from the center of the aircraft. Figure 53 shows the amplitude of the parallel (i.e., x) component and Figure 54 shows the amplitude of the cross polarized (i.e., y) component of the signal measured by PX-5 after subtracting out the background signal. This near-field data was transformed to k-space and probe effects were then removed. The resulting plane wave spectrum due to the target alone is shown in Figures 55-58. Figure 55 shows the amplitude of the parallel polarized component of the plane wave spectrum.

The measured spectrum of the F-105 shown in Figures 55-58 and the previously measured spectrum of the one-foot monopulse tracking antenna (Figures 49-52) were used to predict the signal that would be observed using the tracker over a plane 44.5 inches and over a plane 54.5 inches from the target. These distances correspond to easily obtainable separations on the near-field range. The predicted signal received by both the sum and difference channels of the monopulse antenna were calculated every 0.5 inches in x and y over a 128 x 128 grid. To validate these predictions, measurements were made using the monopulse tracker for horizontal fly-bys separated by 6 inches in elevation over both prediction planes. The tracker was oriented as an elevation-plane monopulse tracker to match the polarization of the illuminator, although the tracker's radiation patterns were measured earlier with it oriented as an azimuth-plane monopulse antenna. Measured data was recorded for both the



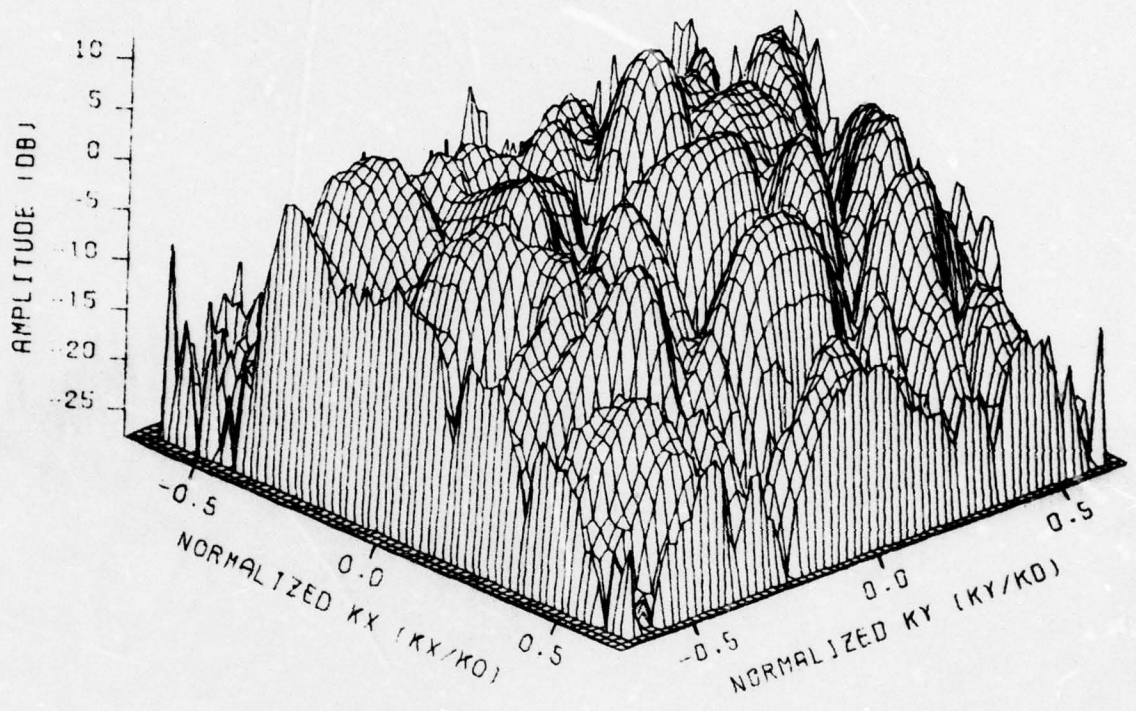
FILE 21. VA (PARALLEL POL.) FOR F-105 USING PROBE PX-5 *

Figure 53. Measured amplitude of parallel-polarized component of the scattered electric field from F-105 model at 9.0 GHz using probe PX-5.



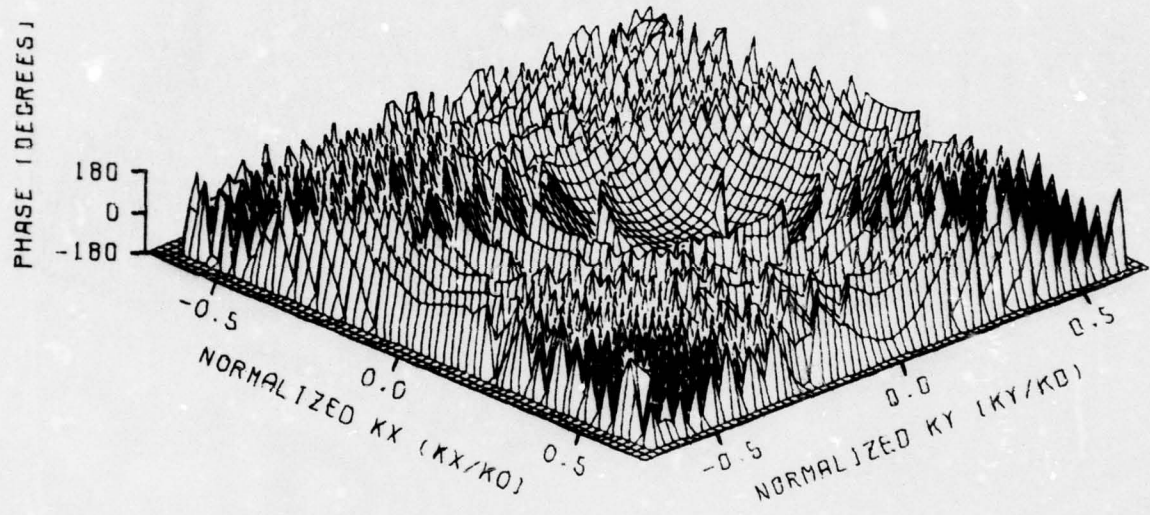
FILE 22, VB (CROSS POL.) FOR F-105 USING PROBE PX-5

Figure 54. Measured amplitude of cross-polarized component of the scattered electric field from F-105 model at 9.0 GHz using probe PX-5.



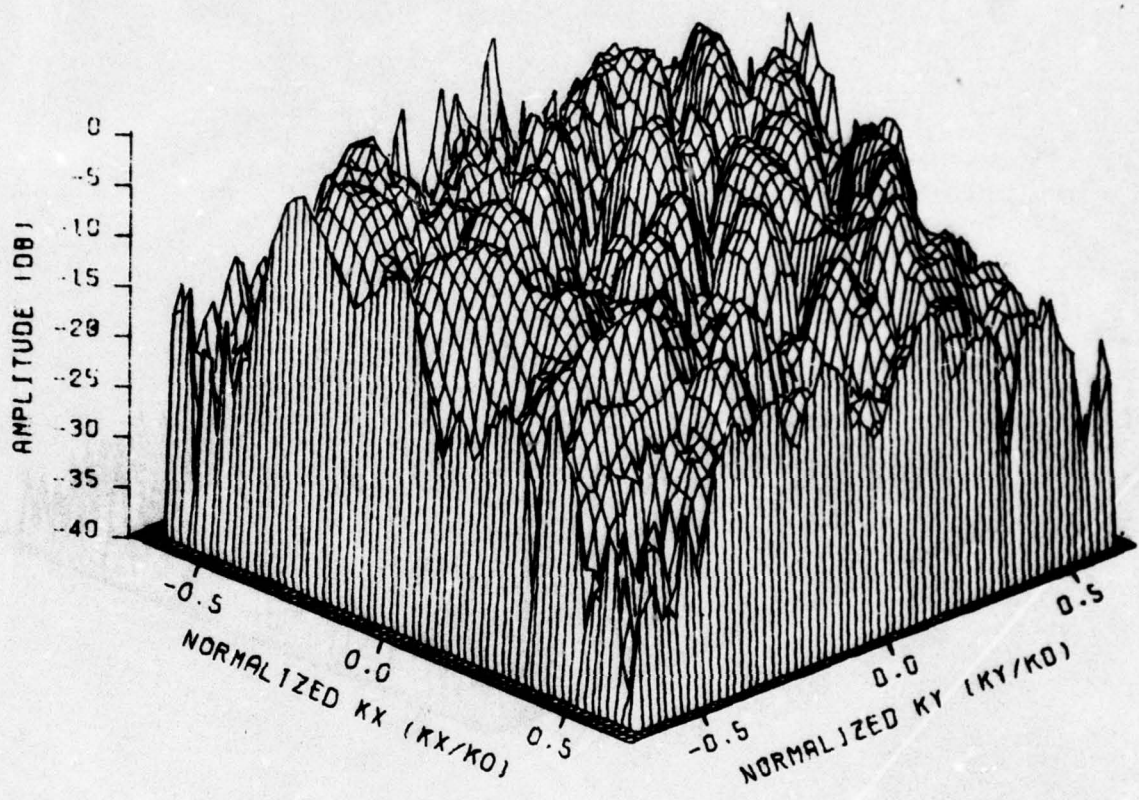
FILE 51, AAX FOR F-105

Figure 55. Amplitude of x-component of scattered plane wave spectrum from F-105 model at 9.0 GHz.



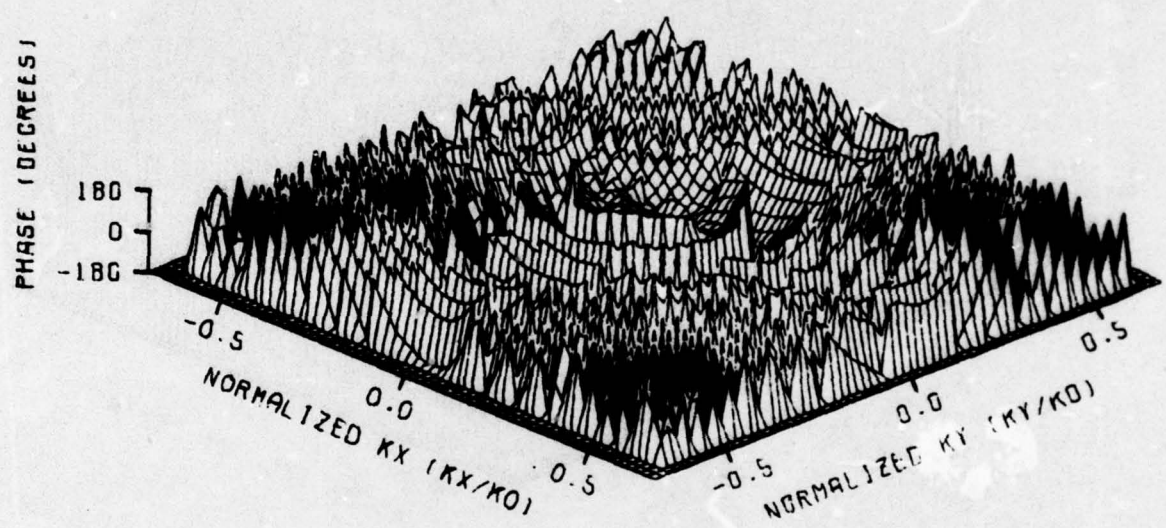
FILE 51. AAX FOR F-105

Figure 56. Phase of x-component of scattered plane wave spectrum from F-105 model at 9.0 GHz.



FILE 52, AAY FOR F-105

Figure 57. Amplitude of y-component of scattered plane wave spectrum from F-105 model at 9.0 GHz.



FILE 52, AAY FOR F-105

Figure 58. Phase of y-component of scattered plane wave spectrum from F-105 model at 9.0 GHz.

sum and the difference channels every 0.5 inches along each of the horizontal fly-by cuts. Figures 59-62 show a comparison of the parallel polarized sum channel signals measured and computed for horizontal fly-bys. It should be noticed that the agreement in amplitude and phase is quite good. Similar data for the difference channel is shown in Figures 63-66 and again the agreement is quite good. Cross polarized signals could not be predicted as well as shown in Figures 67 and 68. It is felt that the difficulty in predicting cross polarized signals is the result of small positioning errors in the measurement setup which can couple the strongly scattered parallel component into the weakly scattered cross component being received. Tests were run in which the monopulse antenna was slightly rotated or the model aircraft slightly repositioned. These changes produced substantial changes in cross polarized signals, as would be expected from typical antenna cross polarization measurements. It was thus concluded that accurate placement of the target and accurate rotation of the probe and monopulse antenna are required to make accurate measurements of the cross polarized components. However, such care was not exercised in performing this set of measurements.

Most tracking systems are not interested in the sum and difference channels by themselves. Instead, these two signals are used to produce error signals that drive tracking circuits which cause the antenna and missile to head toward the target. A typical monopulse tracker looks at the phase of the difference channel relative to the sum channel to determine if the target is to the left of (or below) or to the right of (or above) boresight. The magnitude of the difference signal determines how far the target is from boresight. An analysis of this signal processing technique [10] shows that the monopulse system basically utilizes the ratio of the difference channel voltage to the sum channel voltage to derive the error signal. The phase of

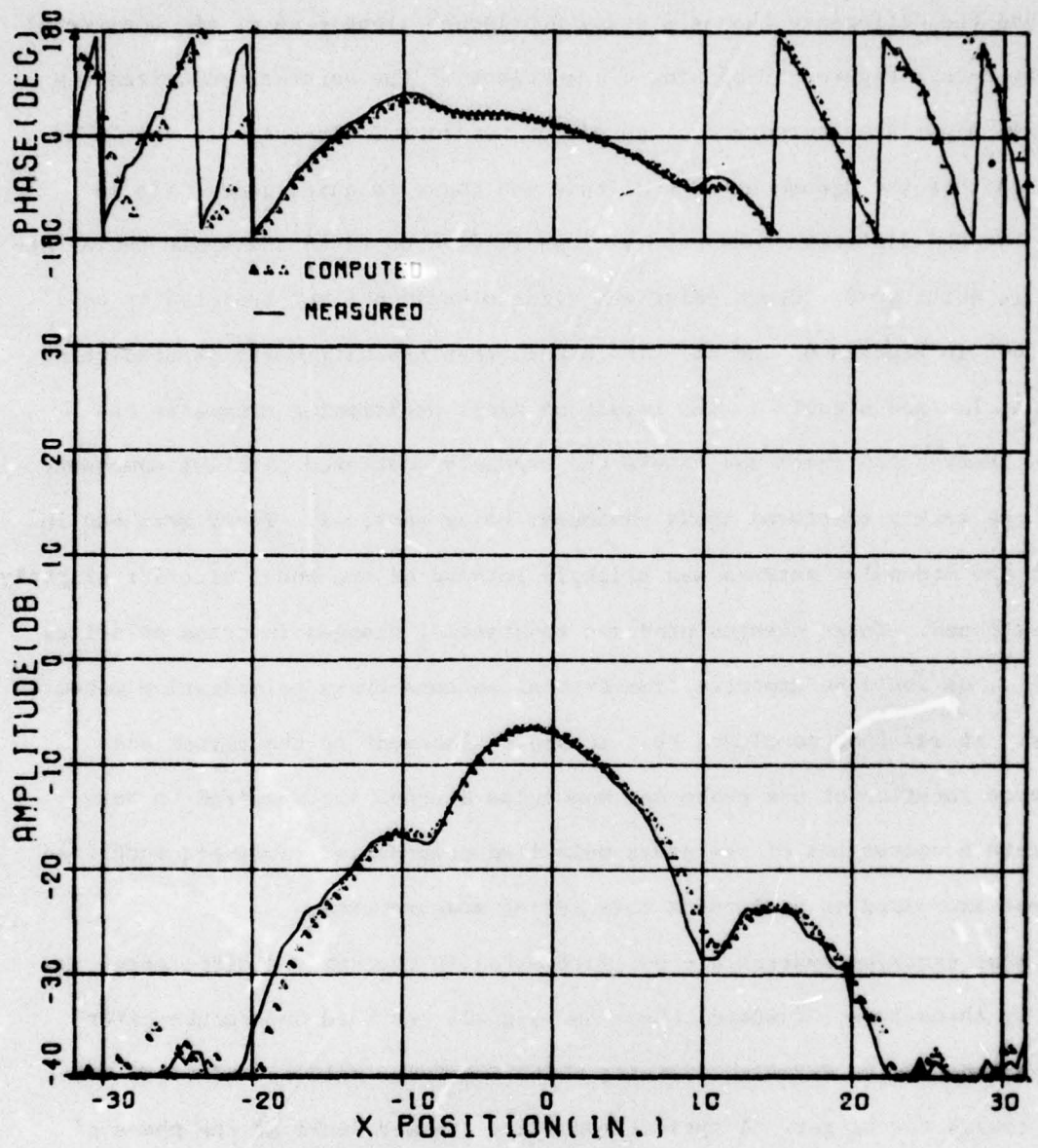


Figure 59. Comparison of measured and computed signal received by sum channel along line $y = -6$ inches on $z = 44.5$ inch plane for parallel polarization.

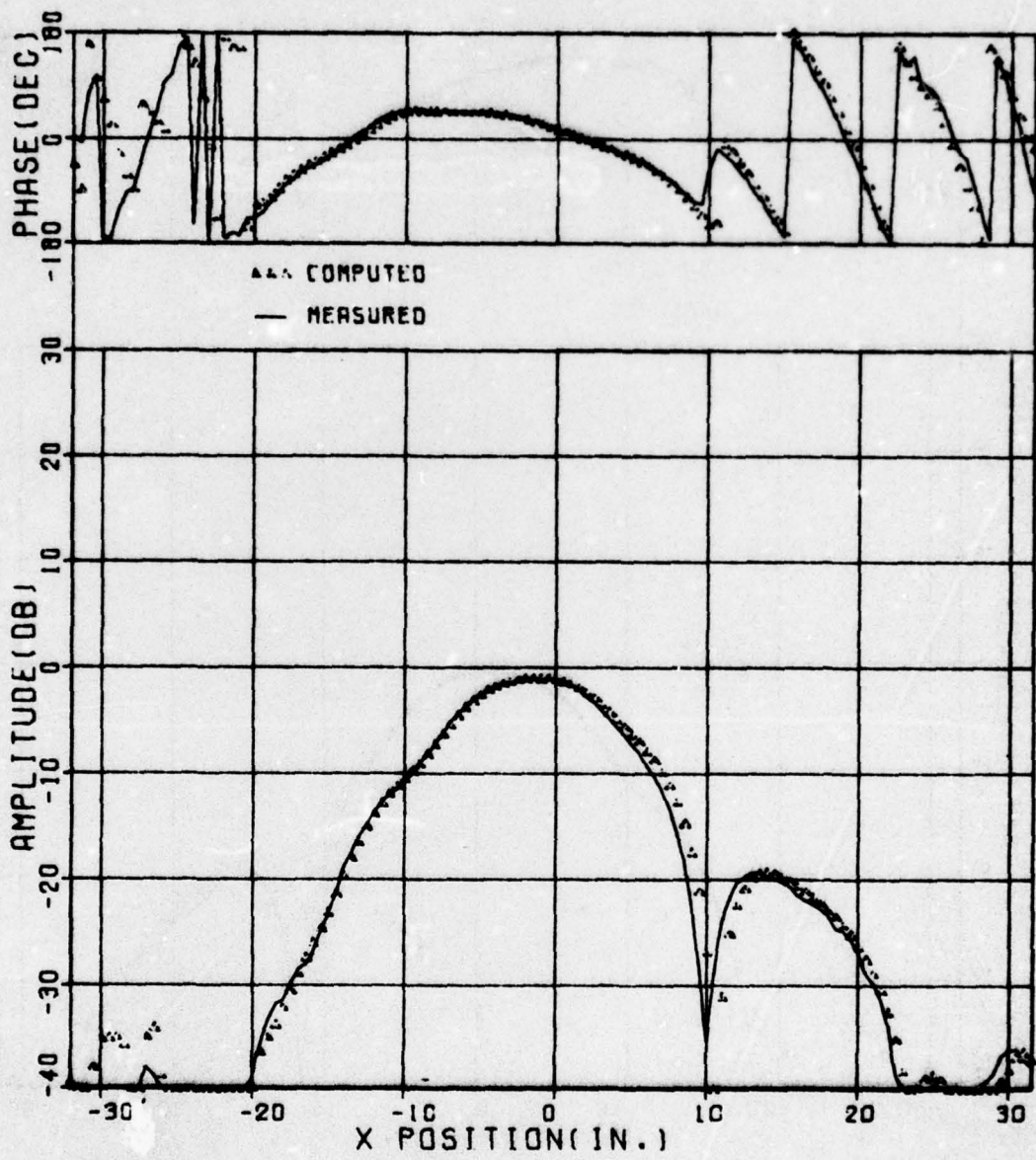


Figure 60. Comparison of measured and computed signal received by sum channel along line $y = 0$ inches on $z = 44.5$ inch plane for parallel polarization.

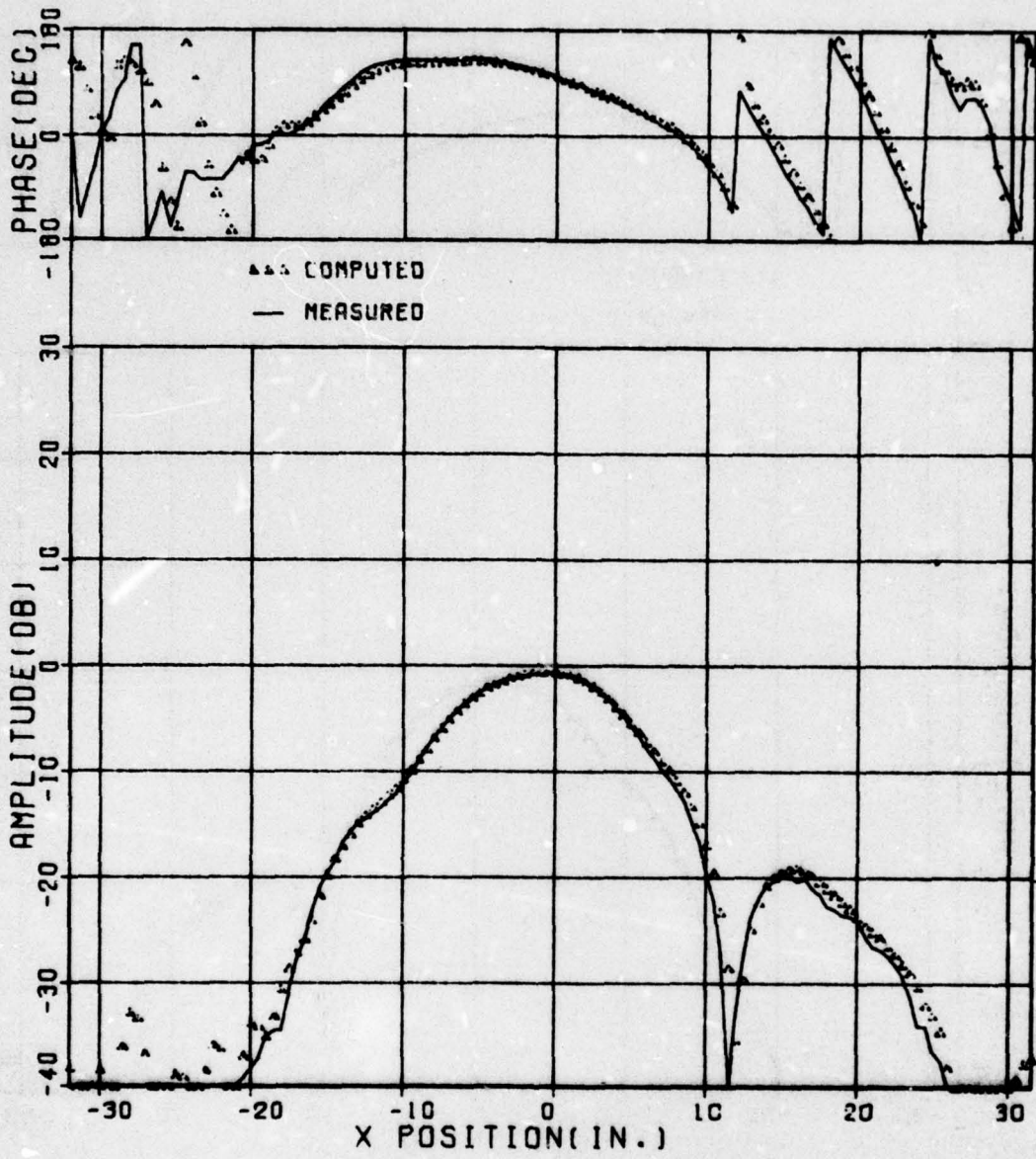


Figure 61. Comparison of measured and computed signal received by sum channel along line $y = 0$ inches on $z = 54.5$ inch plane for parallel polarization.

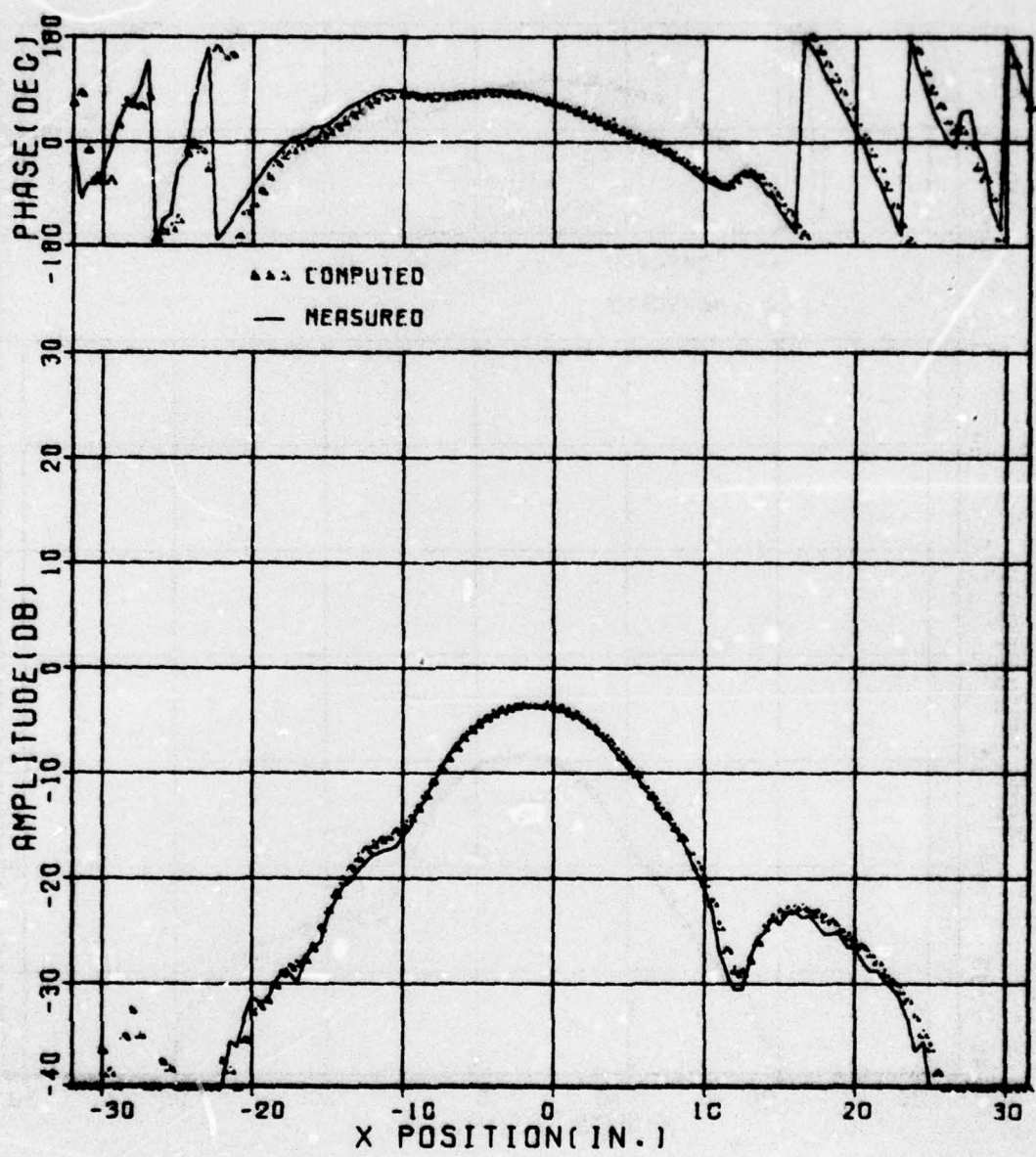


Figure 62. Comparison of measured and computed signal received by sum channel along line $y = 6$ inches on $z = 34.5$ inch plane for parallel polarization.

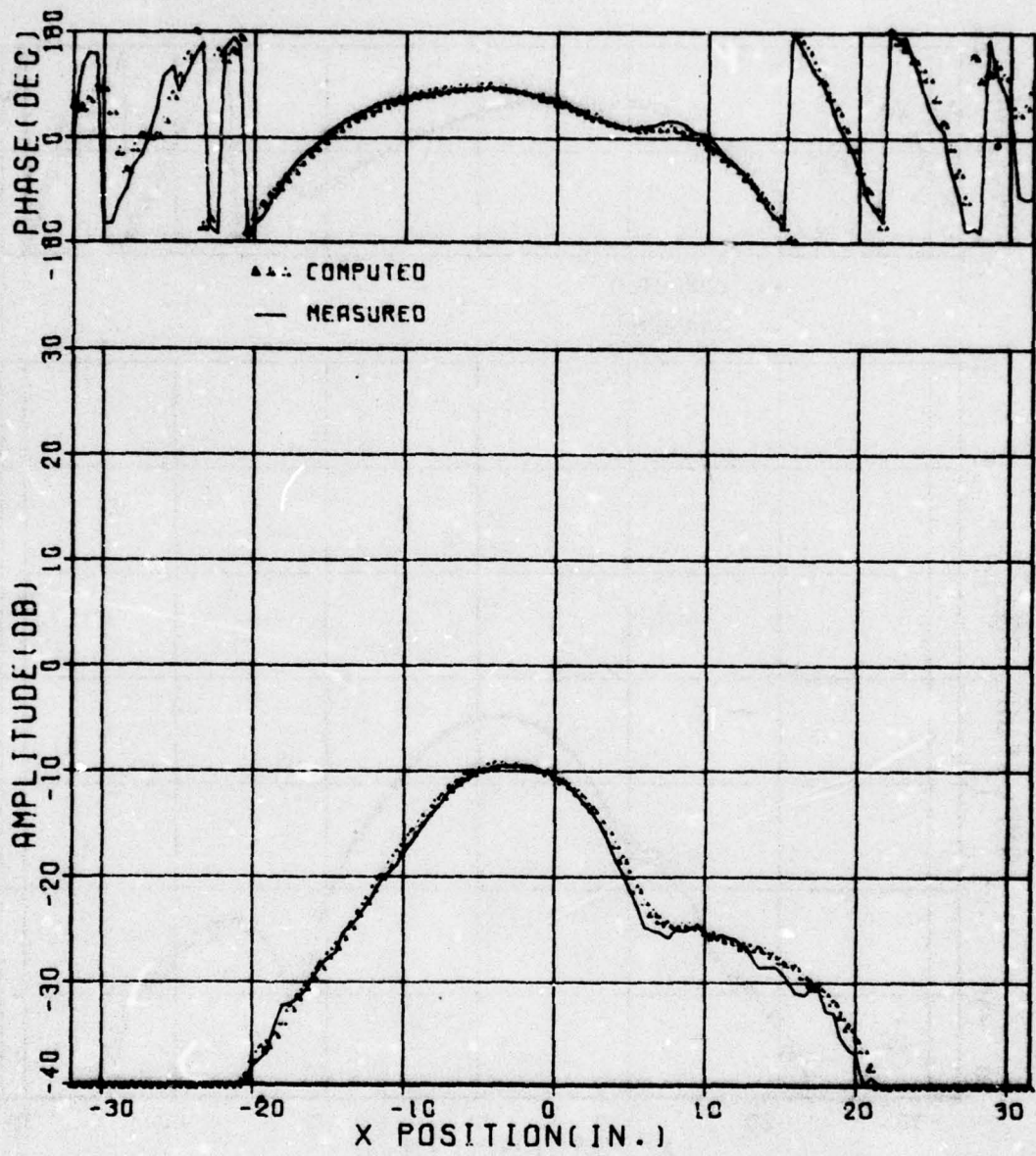


Figure 63. Comparison of measured and computed signal received by difference channel along line $y = -6$ inches on $z = 44.5$ inch plane for parallel polarization.

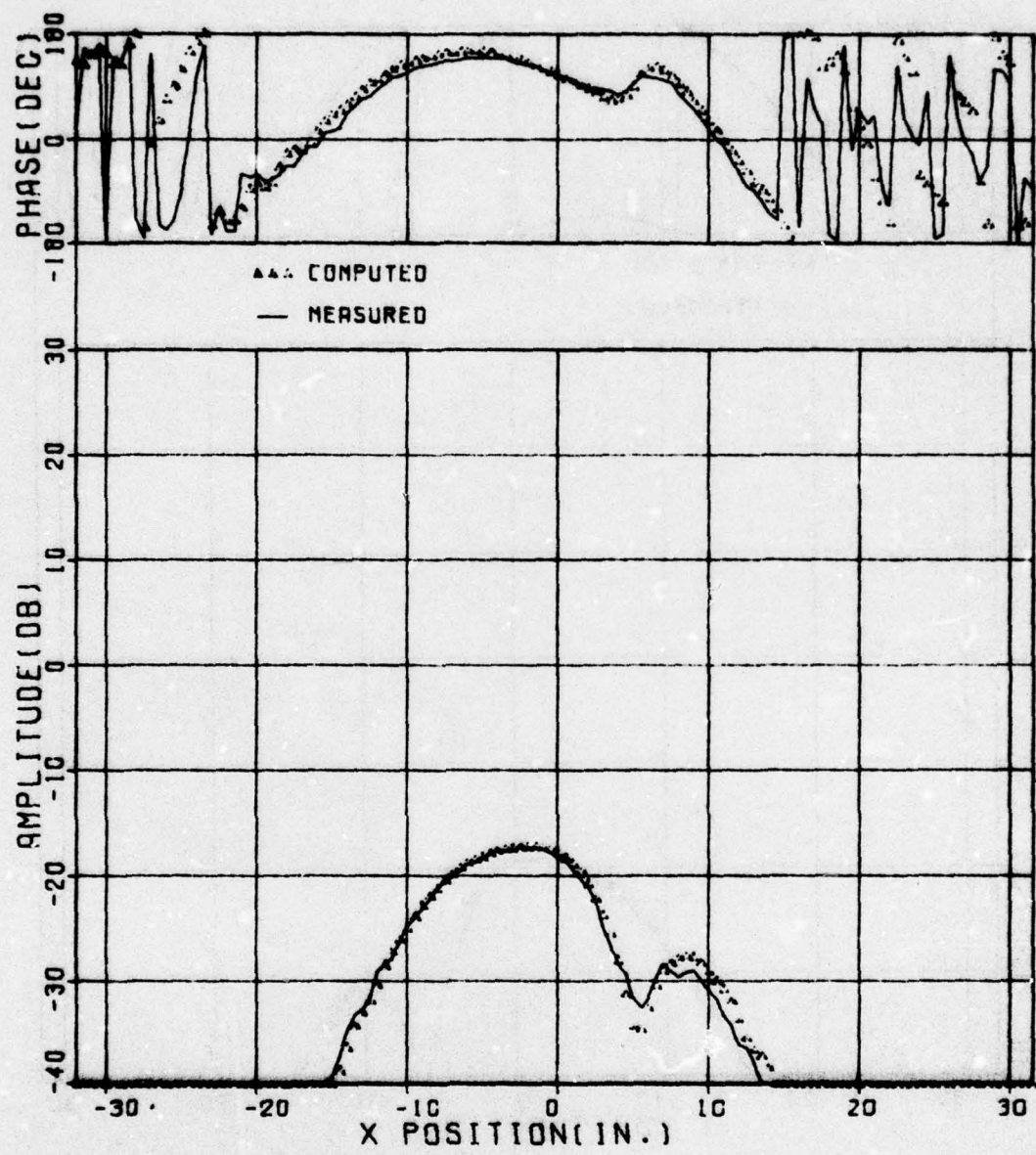


Figure 64. Comparison of measured and computed signal received by difference channel along line $y = 0$ inches on $z = 44.5$ inch plane for parallel polarization.

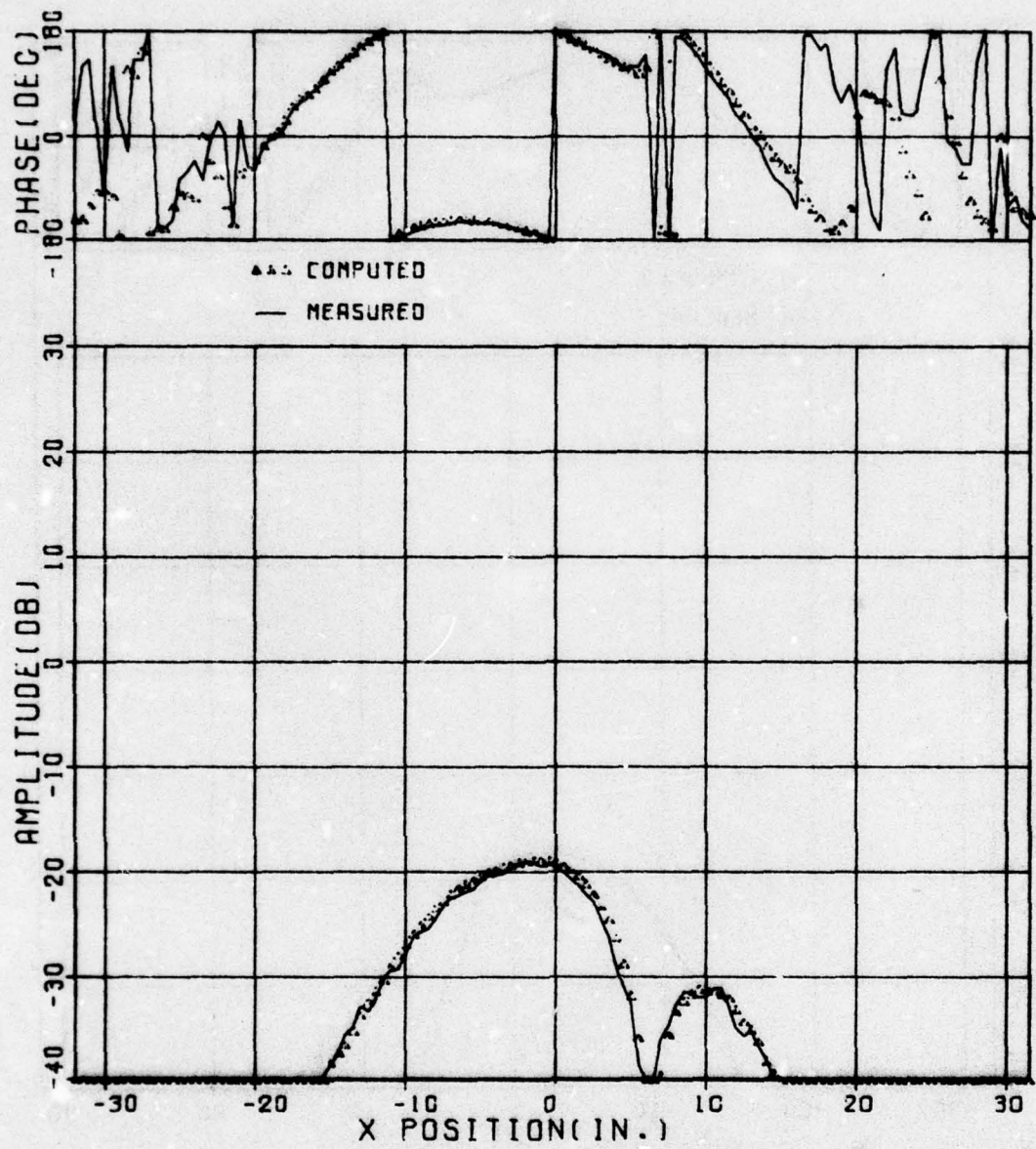


Figure 65. Comparison of measured and computed signal received by difference channel along line $y = 0$ inches on $z = 54.5$ inch plane for parallel polarization.

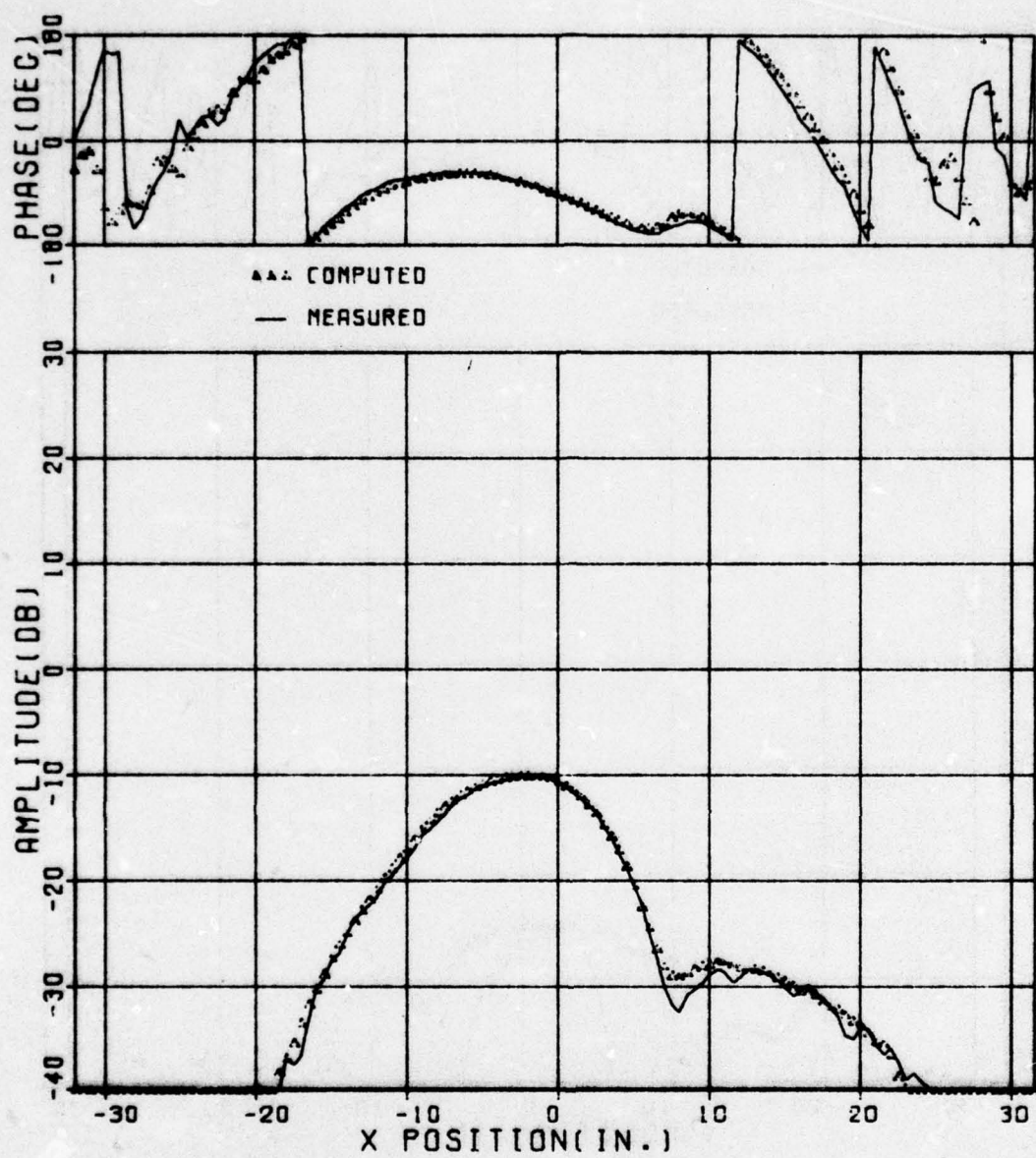


Figure 66. Comparison of measured and computed signal received by difference channel along line $y = 6$ inches on $z = 54.5$ inch plane for parallel polarization.

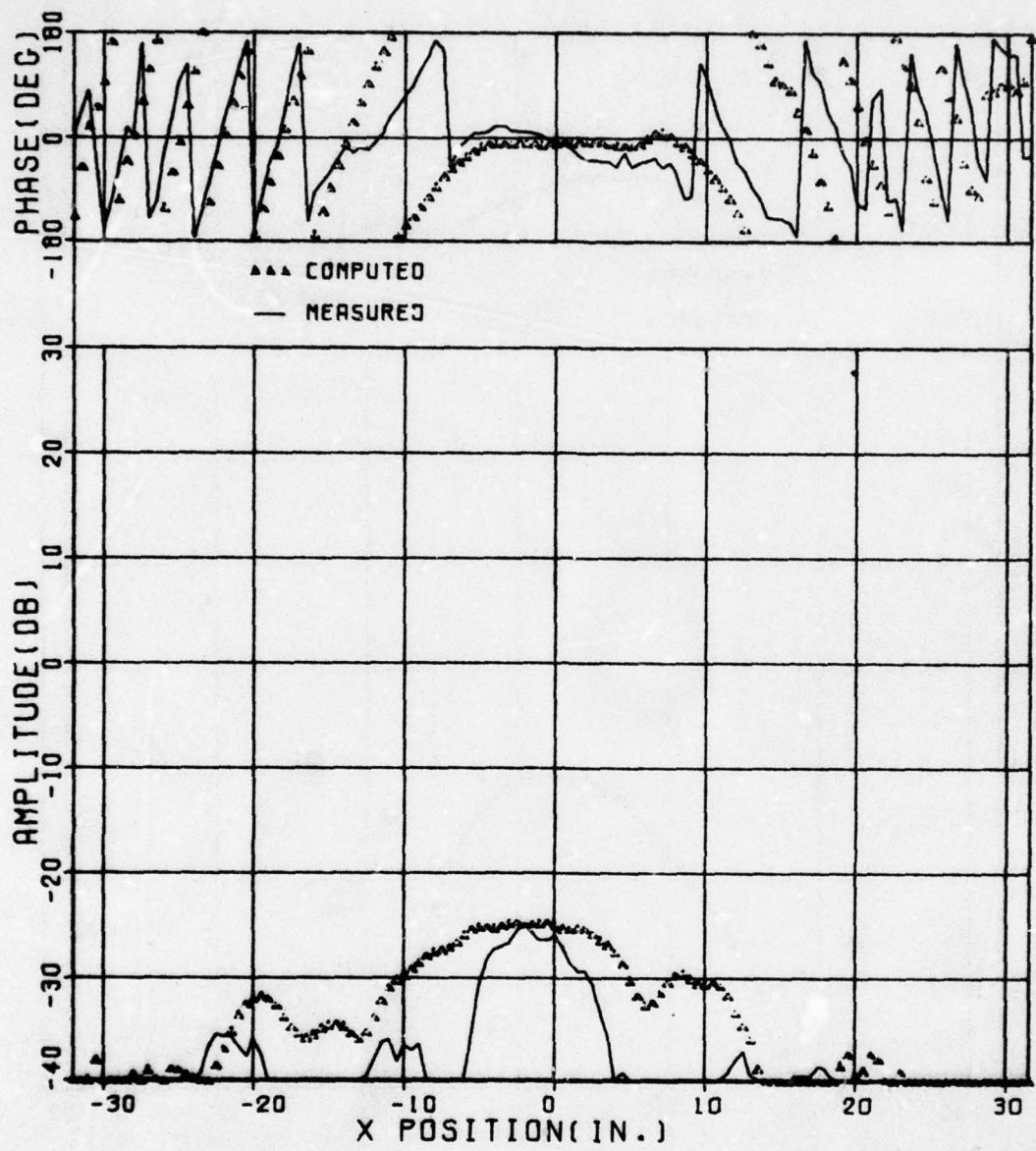


Figure 67. Comparison of measured and computed signal received by sum channel along line $y = 0$ inches on $z = 44.5$ inch plane for cross polarization.

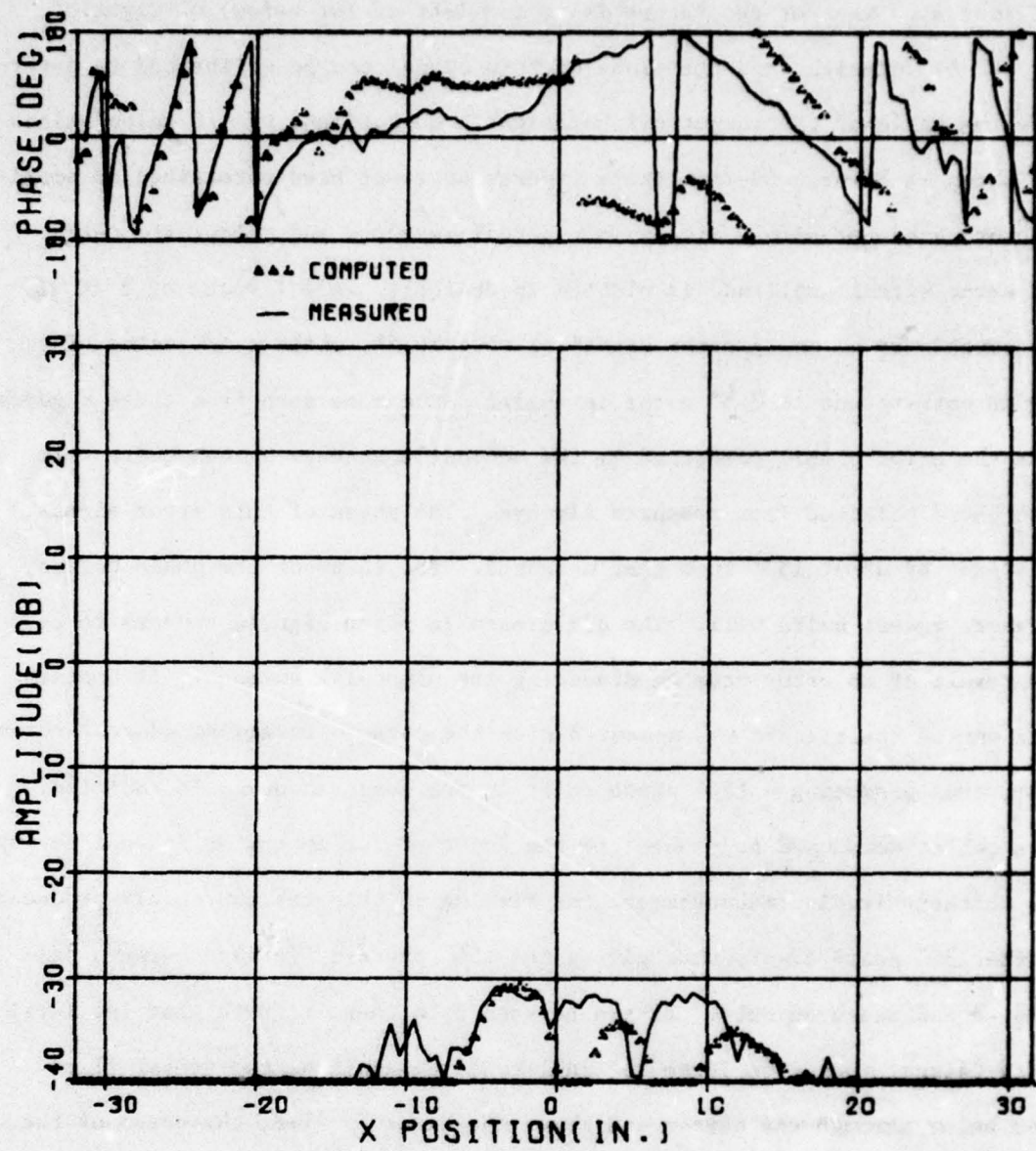


Figure 68. Comparison of measured and computed signal received by difference channel along line $y = -6$ inches on $z = 54.5$ inch plane for cross polarization.

Δ/Σ indicates whether the target is to the left of (or below) or right of (or above) boresight and the slope of this signal can be calibrated to determine the angle of the target off boresight. Comparisons of Δ/Σ calculations are shown in Figures 69-74. These figures have not been normalized in amplitude or phase but simply display the actual measured and calculated data. The error signal amplitude is plotted in decibels. A Δ/Σ value of 1 (0 dB) corresponds to an angle-error signal of roughly 5° , while a Δ/Σ value of -20 dB corresponds to 0.5° error in angle. It can be seen from these figures that the error signal predicted by the monopulse antenna agrees quite well with those obtained from measured fly-bys. The phase of this error signal is offset by about 150° from that measured. The shape of the phase curves, however, agrees quite well. The difference in phase signals appears to be the result of an error made in measuring the monopulse antenna. It appears that one of the signals was measured with the coax to waveguide adaptor rotated 180° , thus producing a 180° phase shift in the measurements. In addition, coax cables were used to connect to the input of the monopulse antenna during its characterization measurements and flexing in this cable probably produced another 30° phase error, thus giving the 150° phase difference between calculated and measured data. It can be seen from these figures that the level of the signal goes from large to small to large again as the seeker flies from below through the center and above the target. Also, the phase of the signal changes by 180° when going from below the target to above the target. Thus, the plane wave spectrum technique does produce the right sense of change in phase error and amplitude error for the monopulse tracking antenna.

Vertical fly-by calculations could be plotted although no measurements were made to compare with these vertical fly-bys. Figures 75-76 show vertical fly-by calculations. The error signal drops to a very low value as

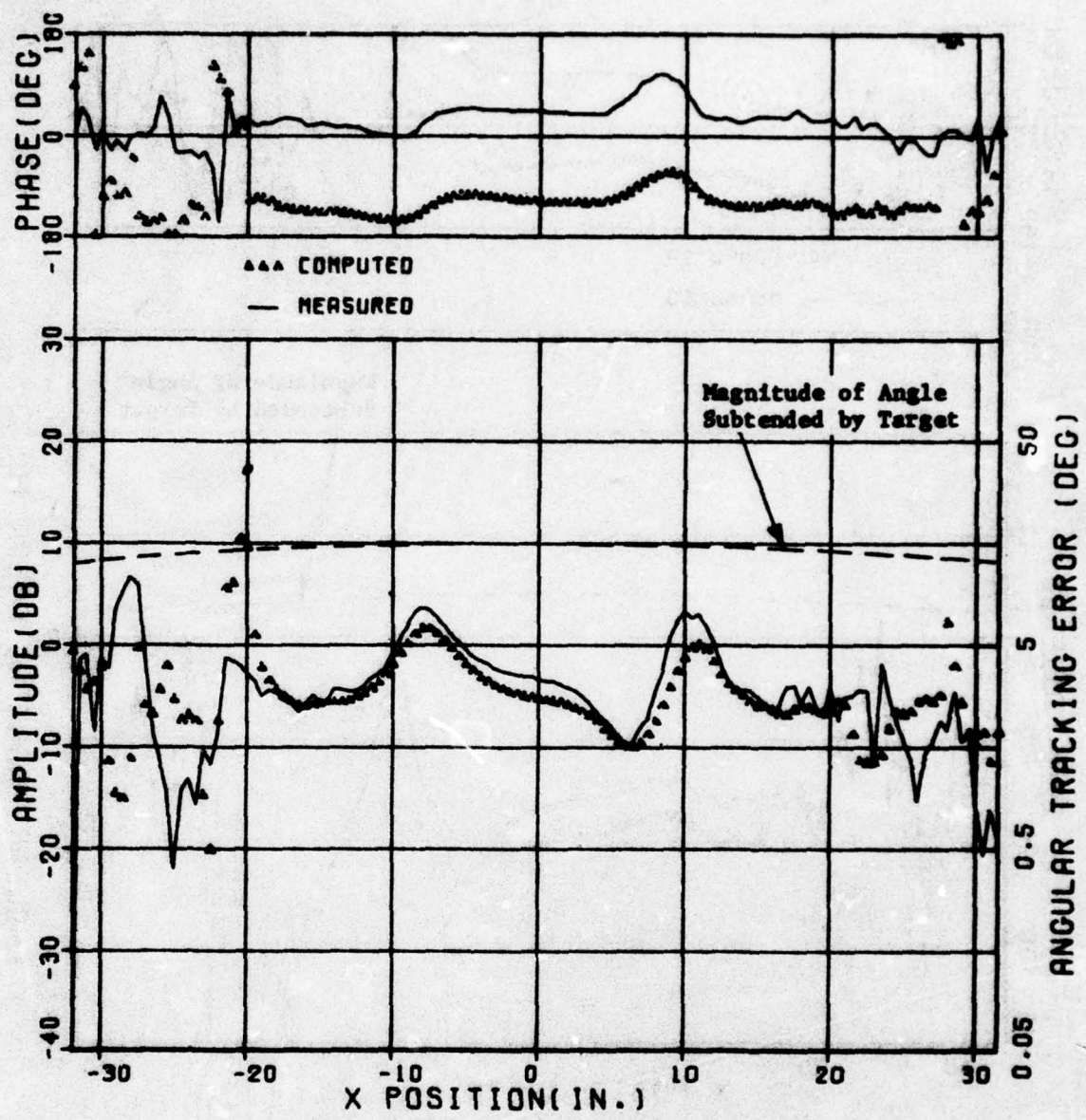


Figure 69. Measured and computed ratio of difference channel to sum channel along line $y = -6$ inches on $z = 44.5$ inch plane for parallel polarization.

BEST AVAILABLE COPY

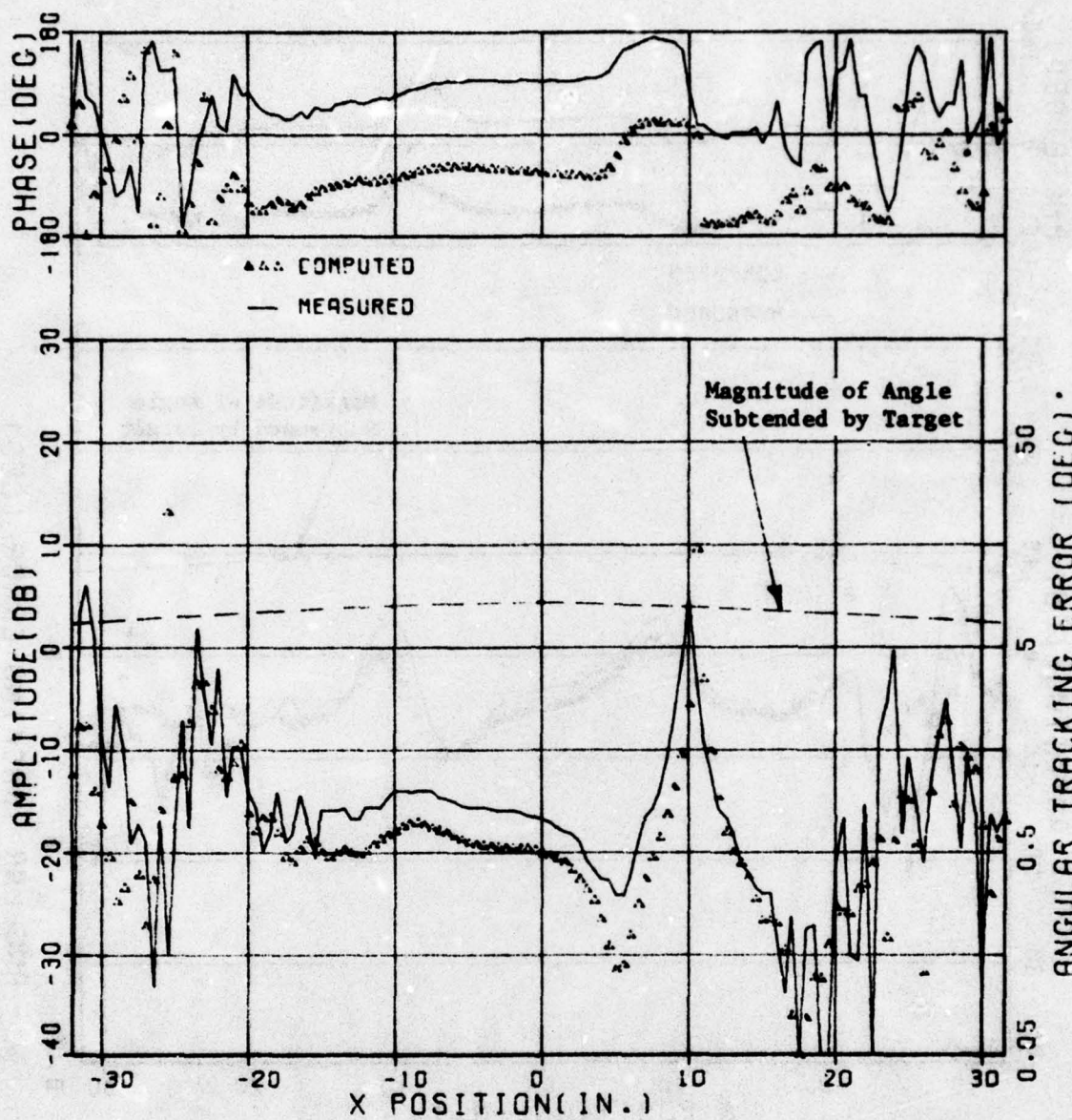


Figure 70. Measured and computed ratio of difference channel to sum channel along line $y = 0$ inches on $z = 44.5$ inch plane for parallel polarization.

BEST AVAILABLE COPY

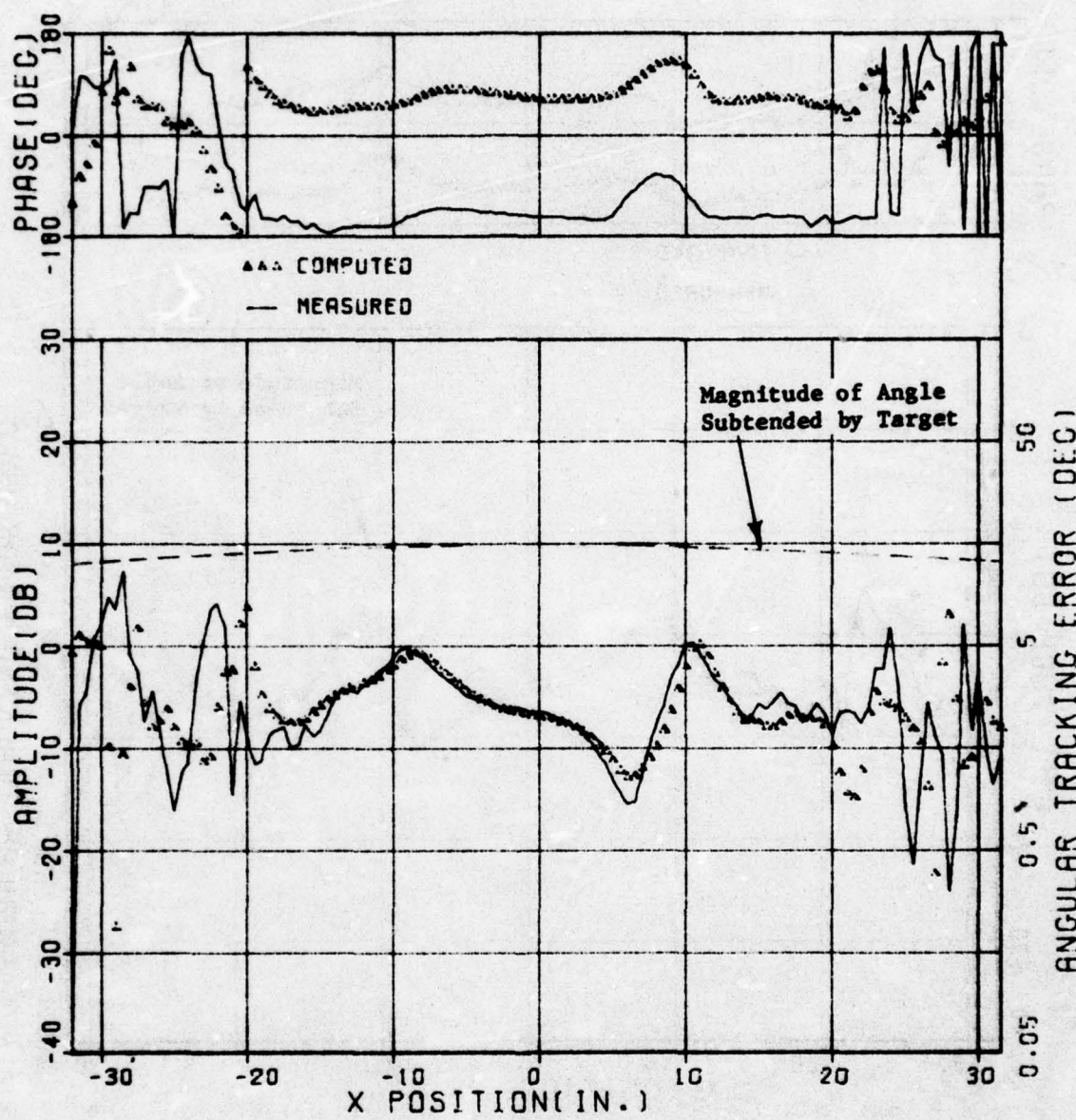


Figure 71. Measured and computed ratio of difference channel to sum channel along line $y = 6$ inches on $z = 44.5$ inch plane for parallel polarization.

BEST AVAILABLE COPY

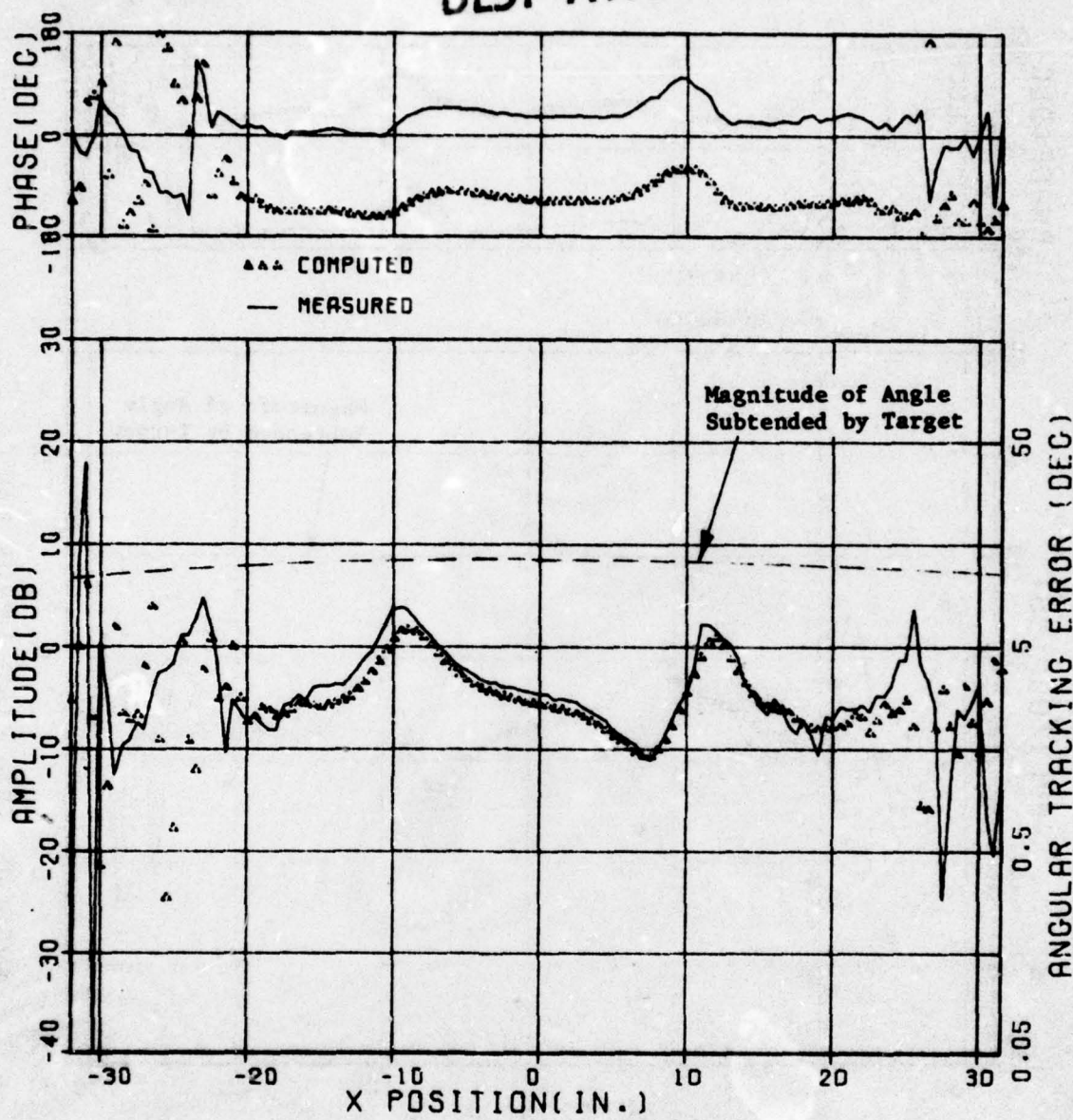


Figure 72. Measured and computed ratio of difference channel to sum channel along line $y = -6$ inches on $z = 54.5$ inch plane for parallel polarization.

BEST AVAILABLE COPY

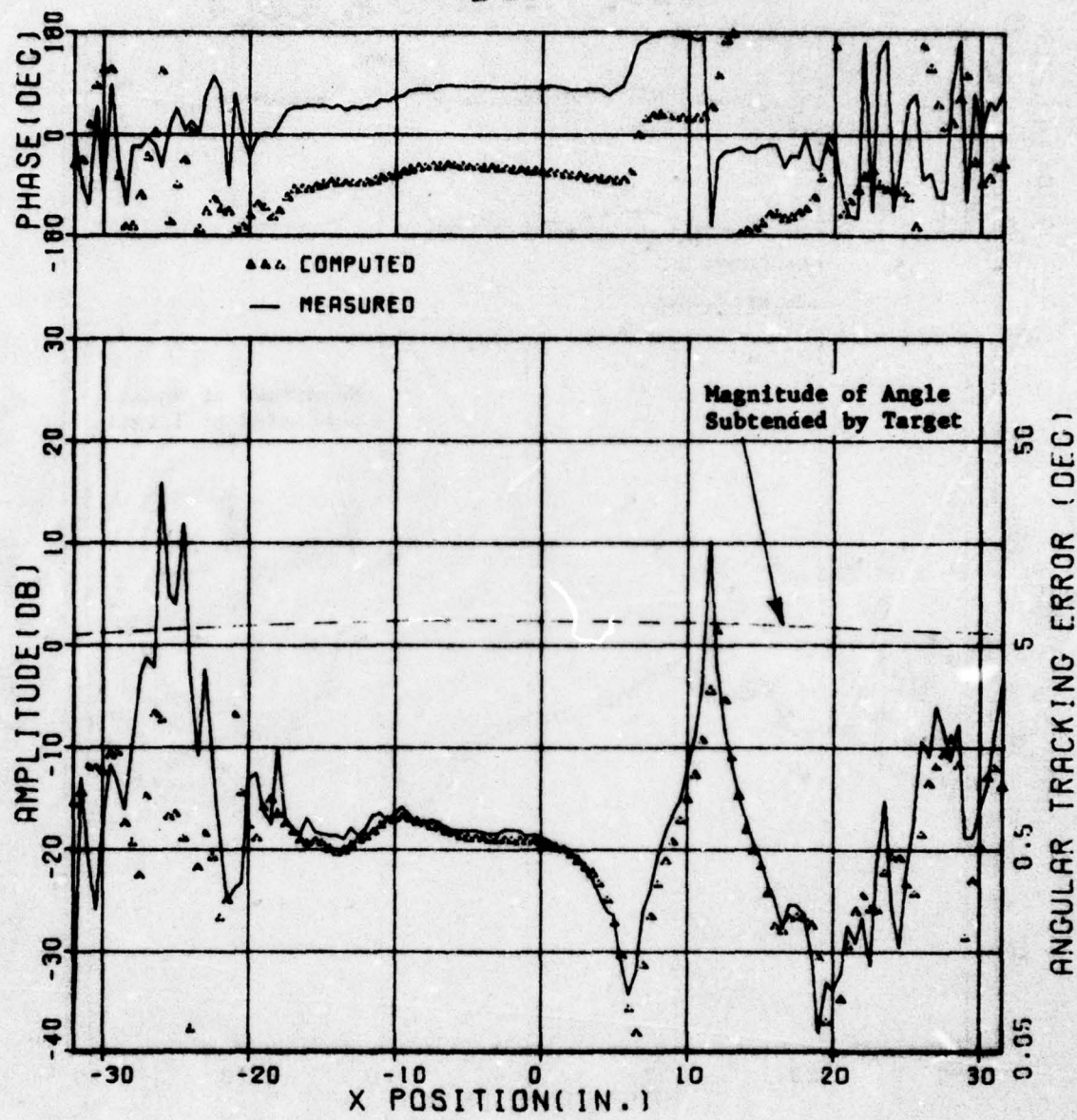


Figure 73. Measured and computed ratio of difference channel to sum channel along line $y = 0$ inches on $z = 34.5$ inch plane for parallel polarization.

BEST AVAILABLE COPY

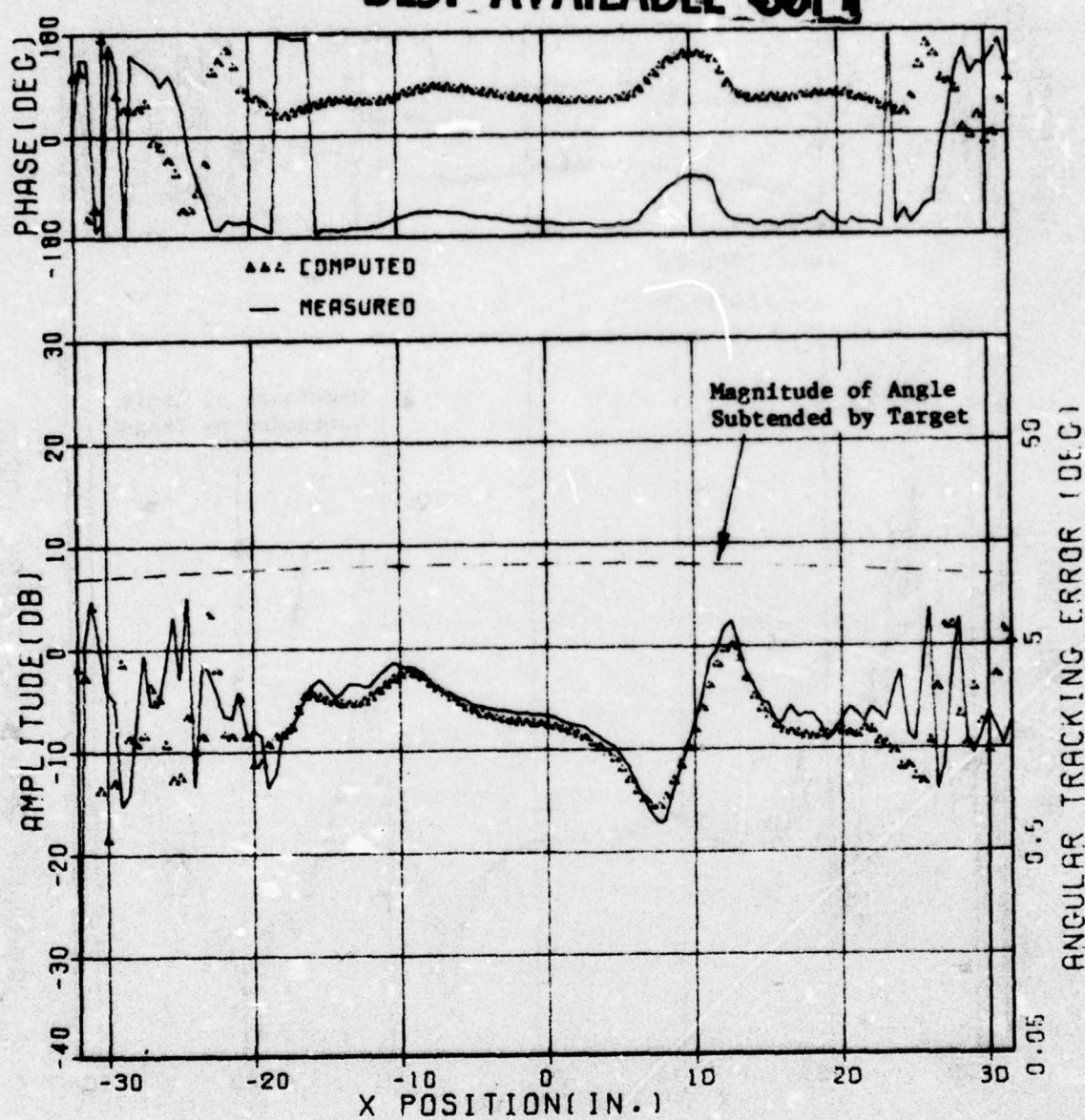


Figure 74. Measured and computed ratio of difference channel to sum channel along line $y = 6$ inches on $z = 54.5$ inch plane for parallel polarization.

BEST AVAILABLE COPY

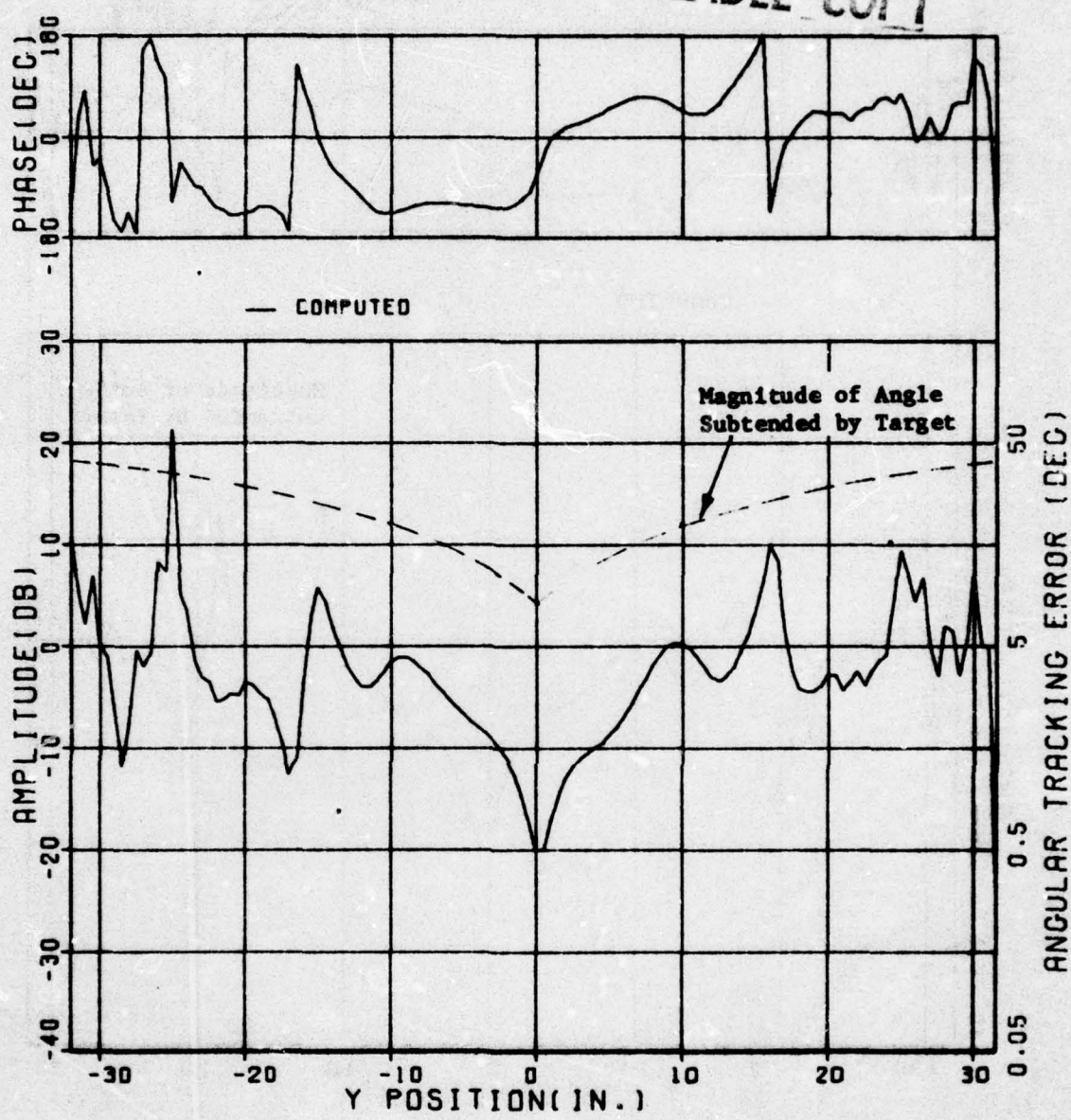


Figure 75. Calculated difference channel to sum channel ratio for parallel polarization along the vertical line $x=0$ inches on the $z = 44.5$ inch plane.

BEST AVAILABLE COPY

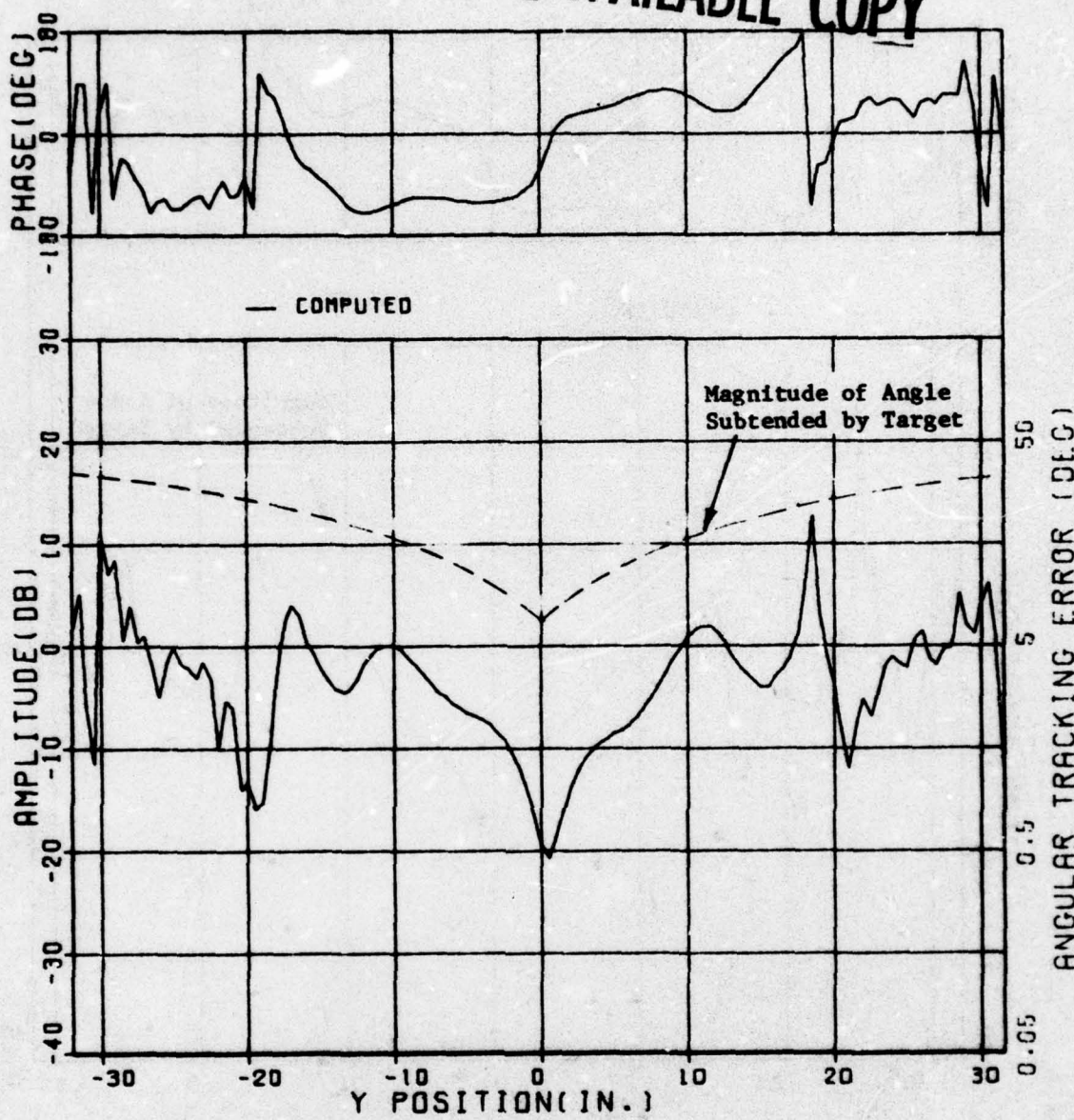


Figure 76. Calculated difference channel to sum channel ratio for parallel polarization along the vertical line $x=0$ inches on the $z = 34.5$ inch plane.

the tracker goes across the target and the phase angle changes by roughly 180° as it crosses the target as is expected for a monopulse antenna.

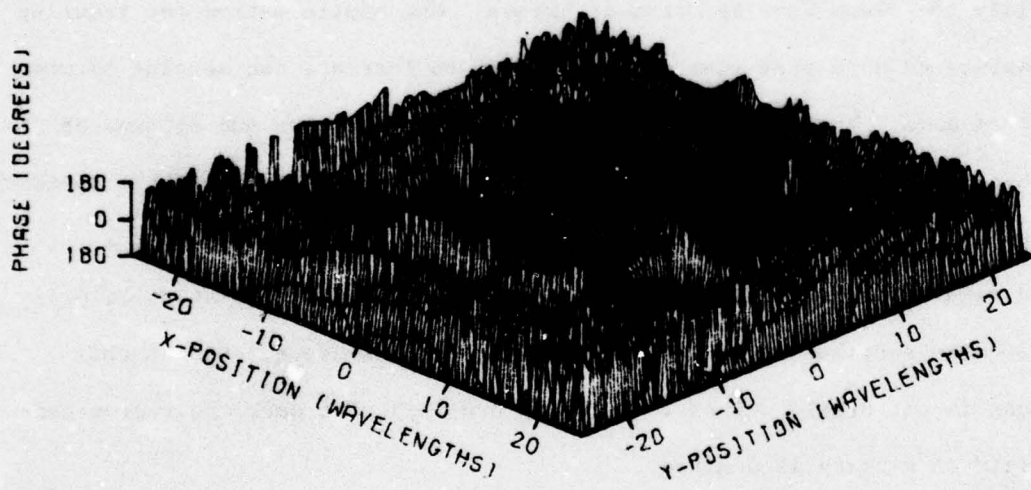
Figures 77 and 78 show the calculated phase of the error signal for parallel polarization over the two measurement planes. The 180° phase shift in going from above to below the target can clearly be seen in this figure. It can also be seen that this error signal applies mainly to the central region where the target is located.

C. Data Reduction Techniques

A number of techniques were considered for reducing the quantity of data that must be measured or the quantity of data that must be processed in order to utilize the Plane Wave Spectrum technique. One simple method for reducing the quantity of data that must be measured is to increase the spacing between samples of data. This process decreases the number of rows and columns of data that must be measured. A conventional size probe is used in this approach. The measured spectrum obtained using this approach is valid only over a limited angular sector near the origin of k-space. Aliasing distortion produces a false spectrum beyond the central region of k-space. Hence, this technique is not usable unless it is known a priori that only the region near the origin of k-space is desired.

The false spectrum may be eliminated by using a large measurement probe. The spectrum of the probe acts like a low pass filter and limits the spectrum to points near the origin of k-space. Thus, the spacing between the samples may be increased and consequently the quantity of data that must be measured can be decreased. However, the measured spectrum is, again, valid only over the central region of k-space. The size of this region depends on the spectrum of the large measurement probe.

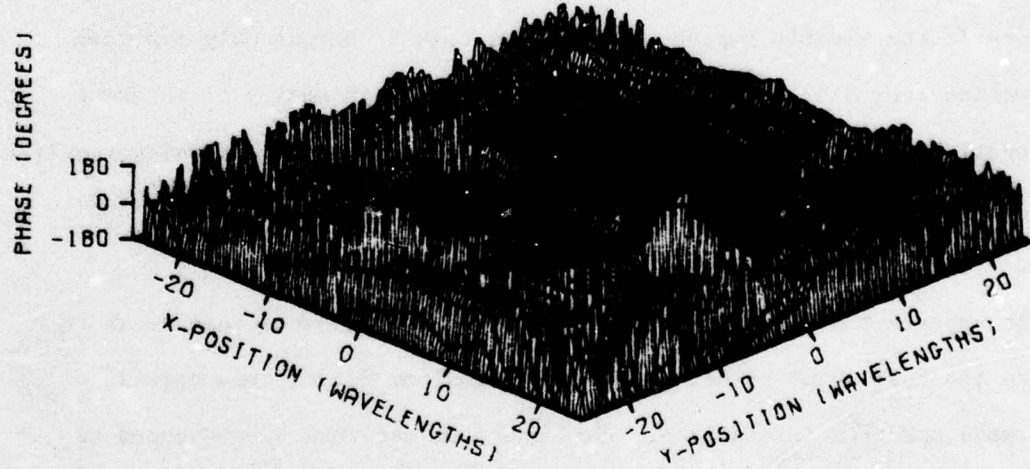
BEST AVAILABLE COPY



FILE 101. TRACKER ERROR VOLTAGE. PARALLEL POL., AT 3/4 IN.

Figure 77. Computed phase of error signal Δ/Σ for parallel polarization
for F-105 model as seen by monopulse tracker at $z = 44.5$ inches.

BEST AVAILABLE COPY



FILE 103. TRACKER ERROR VOLTAGE, PARALLEL POL., AT 10 3/4

Figure 78. Computed phase of error signal Δ/Δ for parallel polarization
for F-105 model as seen by monopulse tracker at $z = 54.5$ inches.

An alternate technique for reducing the quantity of data involves various filtering schemes. Analog filtering may be performed on the measured data directly as it is measured or after it has been recorded on magnetic tape. This approach requires a large number of measurement points, but the data is subsequently reduced in quantity. Consequently, a much smaller array must be Fourier transformed and a small array is then used for subsequent data processing. The technique may also be implemented using digital filtering on a computer. All of the measured data is recorded on magnetic tape and this data is filtered digitally in a fashion similar to the analog filtering process described above. This technique has been described by Joy [2] and can be used to obtain the field over an angular region of space located anywhere in the visible region. Typically, this technique only provides information over a limited region of space which is normally of interest for pencil-beam antennas. However, for RCS problems data is usually required over a large region of space, and so this type of processing is not applicable.

It appears that the most useful technique for RCS measurements is to measure the full quantity of data and to transform all of this data into plane wave spectrum information. This spectrum can then be processed to reduce its quantity but still provide a spectrum that is applicable over all of k-space.

SECTION VI
CONCLUSIONS AND RECOMMENDATIONS

The modal expansion technique using the plane wave spectrum representation has been used to obtain glint characteristics of aerospace targets. This technique allows one set of measurements of the field scattered by a target to be used with the radiation patterns of a variety of antennas to determine the tracking error signal produced from each of these antennas. The technique has been demonstrated with a model F-105 aircraft and a single plane monopulse antenna at X-band. Computed and measured signals have been compared for both the sum channel and the difference channel. The measured ratio of the difference to sum channel signals (which is a function of the angular error) has also been compared with the calculated value. The excellent agreement obtained in both amplitude and phase for measurements of the parallel polarized component of the scattered field shows the basic accuracy of the technique. This good agreement between measurement and predictions has been shown for sum channel signal, difference channel signal and their ratio even at distances very close to the target. The agreement for cross polarized reception has not been as accurate as that for parallel polarization. Measurements performed under this contract have shown that accurate positioning and rotation of the seeker and accurate positioning of the target are required in order to make accurate cross-polarization predictions.

Several techniques for data reduction have been examined under this program. Most of these techniques are applicable when data is required only over a limited angular sector of space, the position of which is known a priori. This approach is often acceptable for antenna measurements. However, for RCS measurements the data is usually required over a wide cone of viewing

angles since the missile's look-direction to the target may change substantially during flight. It is thus recommended that a complete set of data be measured and this data processed to reduce its quantity after its plane wave spectrum has been obtained.

Also presented in this report is a new technique for characterizing near-field measurement probes. This technique permits the same planar scanner to be used for making the probe characterization measurements as is used for making the RCS measurements. Current probe characterization techniques require a separate spherical positioning system for making the probe characterization measurements. Thus, a substantial savings in facility cost can be realized using this new probe characterization technique. Corrections are also presented in this report to errors that have appeared in the literature in the probe correction equations.

Several tasks remain to be undertaken in order to complete the development of the near-field RCS measurement technique described in this report. The measurements presented in this report were made at X-band on a 1/33 scale model, corresponding to full scale measurements at VHF frequencies. To obtain data on this model applicable to microwave frequencies, the measurement wavelength needs to be in the millimeter range. Antenna measurements have been made at 70 GHz on the Georgia Tech near-field range, and it is anticipated that model RCS measurements can also be performed at millimeter wavelengths. The need exists to reduce the size of the target illuminator. A smaller illuminator would simplify its positioning and would permit smaller bistatic angles to be measured. Current near-zone RCS measurements have been relative in nature. A calibration technique needs to be established to obtain absolute RCS data from the near-zone measurements. Processing of the near-field data is currently performed on a large, general purpose computer. A number

of disadvantages have resulted from this approach including slow turn around time and extra manpower required to transfer data. Improved operation would be obtained by using a dedicated minicomputer with a disc system. This would permit on-site data reduction and processing and would reduce the data turn-around problem. A substantial amount of software must be developed in order to permit such operation on a minicomputer. In addition, data reduction techniques must be developed and implemented on a minicomputer system for electrically large targets. Techniques are available for doing each of the above tasks and have been evaluated by Georgia Tech.

APPENDIX

NEAR-FIELD COMPUTATION USING BANDPASS FILTERED DATA

A theoretical investigation of the number of plane waves required to describe a small region of a scattering pattern was undertaken and a summary of this investigation is given below. Between the extremes of all visible wavenumbers at close-in near fields (and even invisible wavenumbers corresponding to evanescent waves in the very close-in near field) and a single wavenumber at infinity, there exists a wavenumber bandwidth which describes the significant field contributions for most scatterers. This will now be briefly explained. The field at an observation point is given by the integral of a plane wave spectrum. The major contribution from the integrand comes from its stationary phase point. At this point the integrand is slowly oscillating and a net contribution to the value of the integral is made. At increasing angles from the observation point direction, the integrand varies more and more rapidly, but with equal and opposing values, so now there is no net contribution to the integral. Therefore, what this says is that although a particular region of the PWS may have an integrand resulting in significant contribution, such as the main beam or first sidelobe, the wavenumbers outside that region have an integrand result with little or no net contribution.

An expression will now be developed for the number of plane waves required to describe the significant field contributions to a particular major lobe based on the 3 dB width of the lobe and on the value k_m of the largest visible wavenumber. Recall the uncertainty principle

$$\Delta x \Delta p_x \geq \frac{1}{2} \hbar \quad (32)$$

where

$$p_x = \hbar k_x \text{ and Equation (32) becomes}$$

$$\Delta x \Delta k_x \geq \frac{1}{2} \quad (33)$$

where Δx is the standard deviation or half the 3 dB width of the lobe. Therefore, we define

$$\Delta X = 2\Delta x \quad (34)$$

and Equation (33) becomes

$$\Delta X \Delta k_x \geq 1 \quad (35)$$

where the 3 dB width ΔX is as shown in Figure 79. The number of plane waves, n , required to describe the lobe is

$$n = \frac{\Delta k_x}{\delta k_x} \quad (36)$$

where δk_x is the wavenumber-space sample increment given by

$$\delta k_x = \frac{2k_m}{N} \quad (37)$$

where N is the total number of wavenumber-space samples and

$$k_m = k_o \sin \theta_m \quad (38)$$

where θ_m is the angular width of the pattern. Rewriting Equation (35) as

$$\Delta k_x \approx \frac{1}{\Delta X} \quad (39)$$

and substituting into Equation (36), one obtains the expression for n :

$$n = \frac{1}{\delta k_x \Delta X} \quad (40)$$

which is in terms of the 3 dB lobe width and wavenumber-space increment.

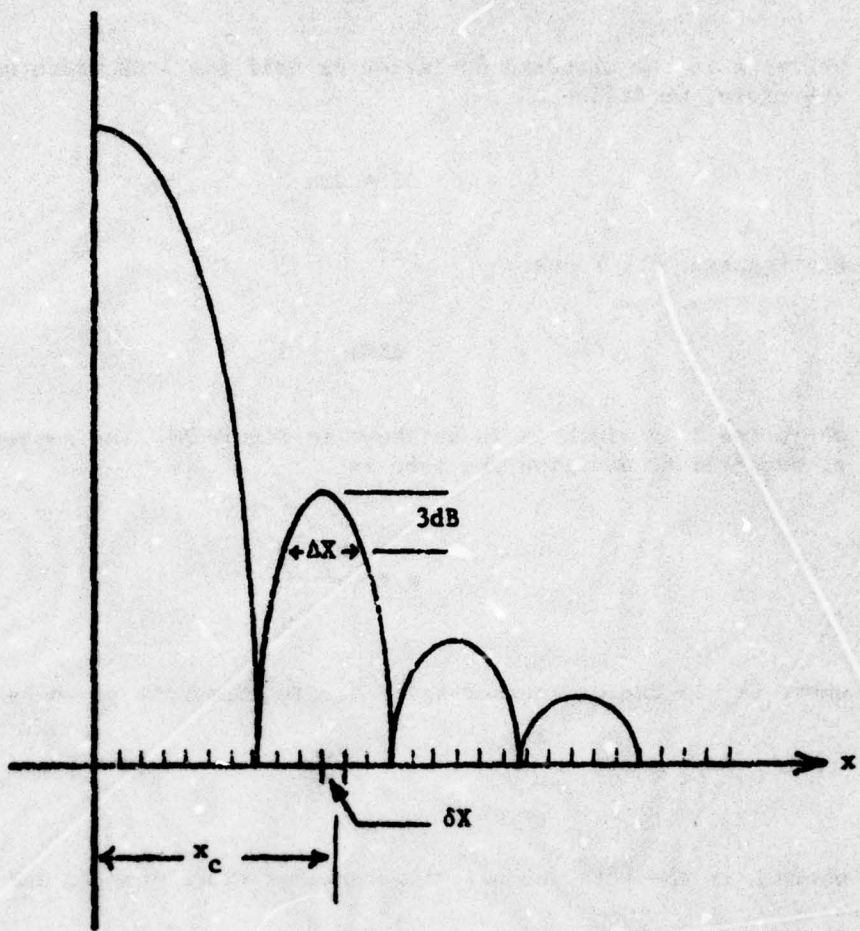


Figure 79. Diagram of the relation between the near-field sidelobe location x_c , the lobe 3-dB width ΔX , and the sample spacing δX .

At this point, an expression which determines the center of the desired wavenumber region is needed. Referring to Figure 80, we express the relationship between the 3 dB lobe widths, ΔX_0 , ΔX_1 , and the distance of the measurement plane Z_0 and the computed plane Z_1 as

$$\frac{\Delta X_1}{\Delta X_0} = \frac{Z_1}{Z_0} \quad (41)$$

and solving for ΔX_1 , we obtain

$$\Delta X_1 = \Delta X_0 \frac{Z_1}{Z_0} . \quad (42)$$

The center of the region ΔX is

$$x_c = Z_1 \tan \theta_c \quad (43)$$

where θ_c is as defined in Figure 81. Changing to wavenumber-space coordinates, the center of the wavenumber region of interest is expressed as

$$(k_x)_{center} = k_0 \sin \theta_c . \quad (44)$$

Thus, Equations (40) and (44) are first order expressions for the size and location of a wavenumber bandpass filter that includes the significant field contributions which describe a particular near-field angular sector (main beam or sidelobe).

The bandpass filtered data approach to data reduction was tested on a uniformly illuminated 8λ square aperture as indicated in Figure 82. The amplitude and phase over a 32λ by 32λ region of the near-field plane was obtained by using a sample spacing of $\Delta x = \Delta y = \lambda/2$, thus obtaining a 64×64 array of simulated near-field data points. The center line of the plane-wave

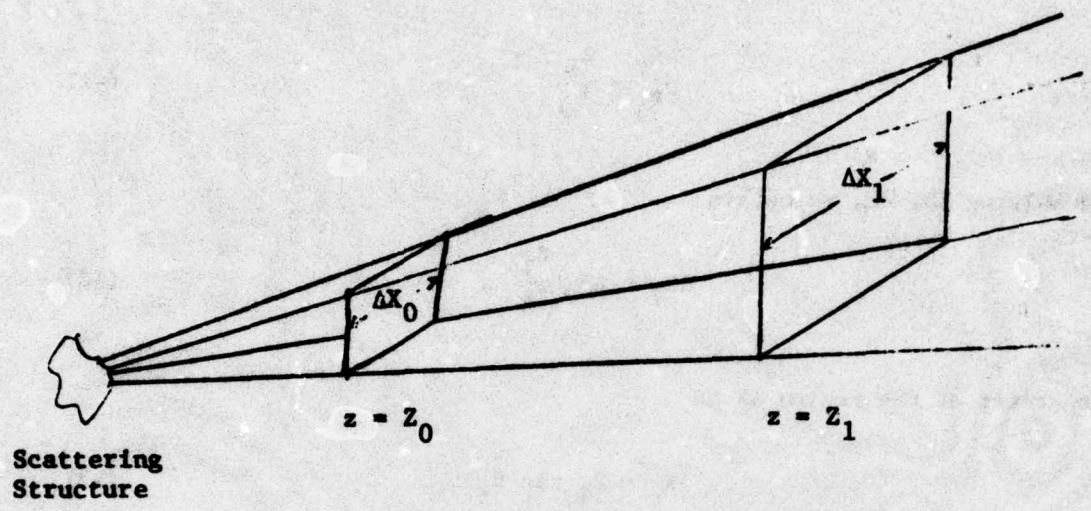


Figure 80. Location of measurement plane ($z = Z_0$) and computed plane ($z = Z_1$) with respect to the scattering structure.

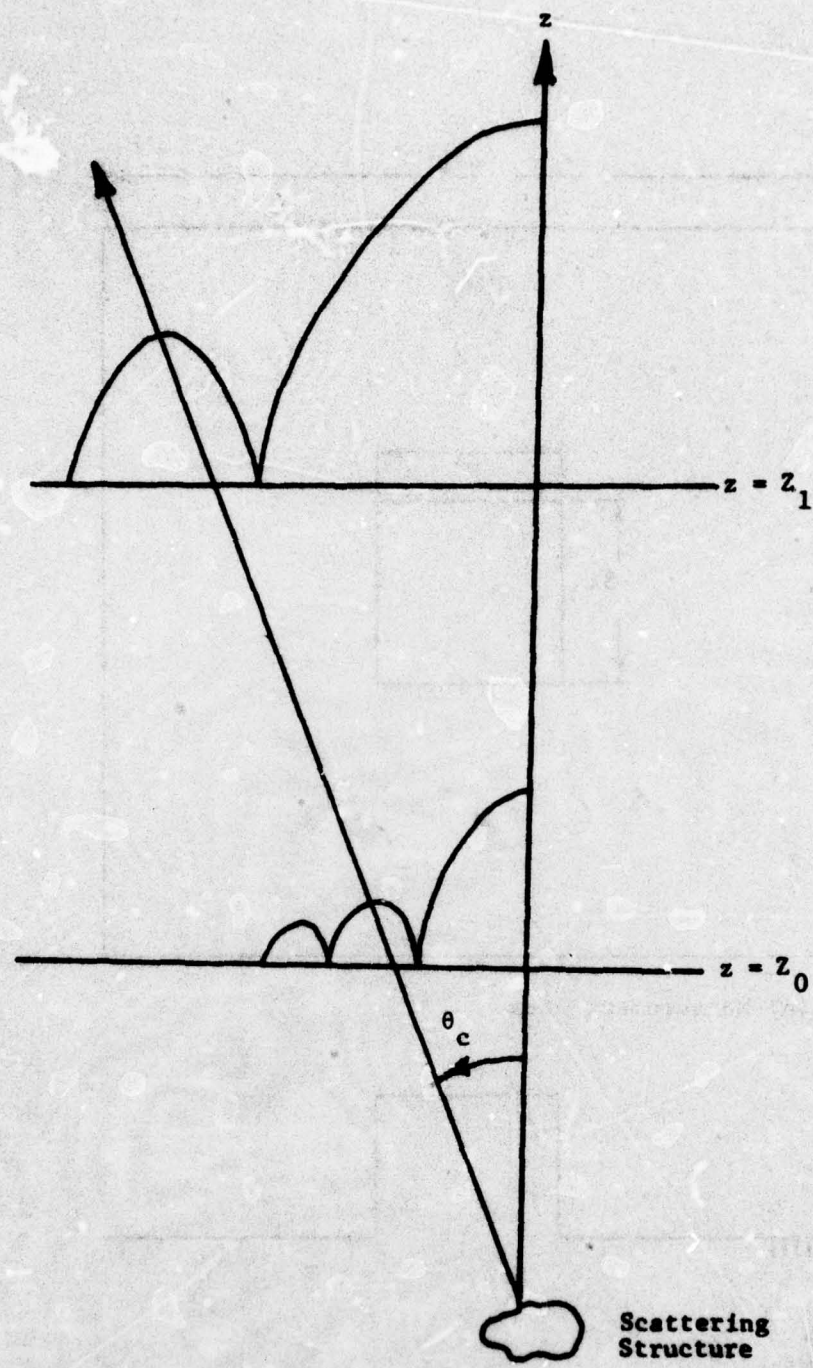
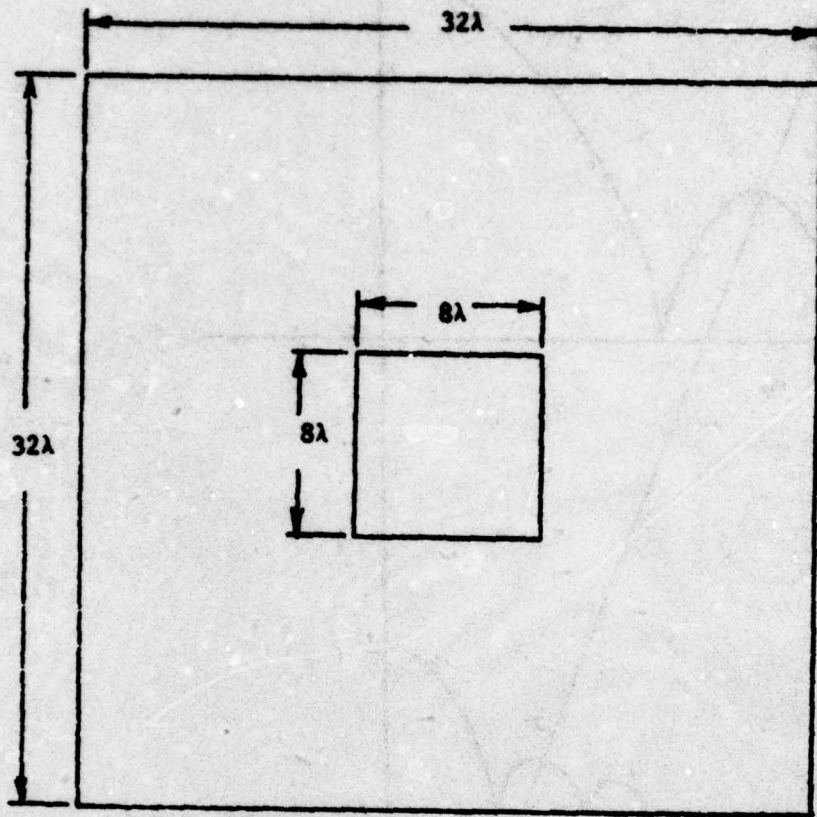
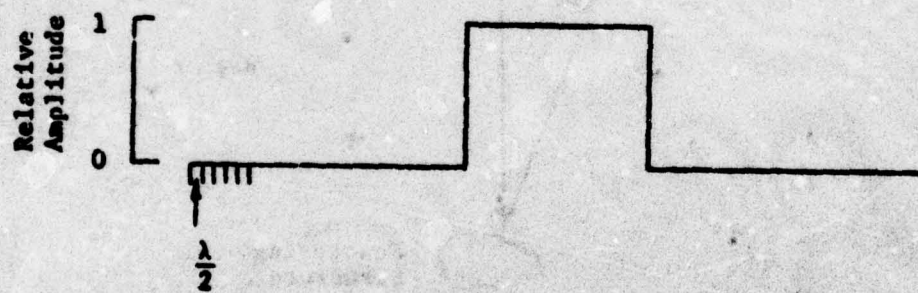


Figure 81. Location of center of the region of interest.



(a) Measurement Area



(b) Illumination Function and Sample Spacing

Figure 82. Location of eight wavelength square aperture in the measurement area and its respective illumination function.

spectrum computed using the discrete FFT from this sampled near-field on the $z=0$ plane of the uniformly illuminated 8λ square aperture is shown in Figure 83. Integration of the PWS was performed over the entire 64×64 array of spectral data using the Bivariate Integration Algorithm. This effectively corresponded to integration over all visible wavenumbers (from $-k_o$ to $+k_o$). The integration was again performed employing a wavenumber bandpass filter from minus .25 k_o to plus .25 k_o in both k_x and k_y , which corresponded to a 16×16 array centered in the wavenumber spectrum. The results of the integration performed over the wavenumber limited region are compared to integration over the entire PWS array in Figure 83. Only the center-line data representing a single near-field "cut" is plotted.

Integration over a 16×16 wavenumber array results in good agreement in the first sidelobe region as well as the main beam. Integration over smaller wavenumber widths was also performed to numerically verify the results of Equation 44. The results of low-pass filtering the wavenumber region to .125 k_o , which corresponds to integration over an 8×8 wavenumber array, are shown in Figure 84. Here, the near field computed from the low-pass filtered PWS is compared to the near field computed using the unfiltered PWS. Again, very good agreement is exhibited in the main beam region with only minor discrepancies appearing the first sidelobe. Therefore, it could be said that Equation 44 provides a conservative estimate of the number of plane waves required to describe a particular sector of interest, at least in the main beam region. Because of the good agreement for the case of an 8×8 wavenumber array, further low-pass filtering of the spectral data was performed to determine that a lower limit on the number of plane waves which would adequately describe the main beam did exist for this particular near-field distance ($0.1 D^2/\lambda$). Figure 85 presents the results of integration

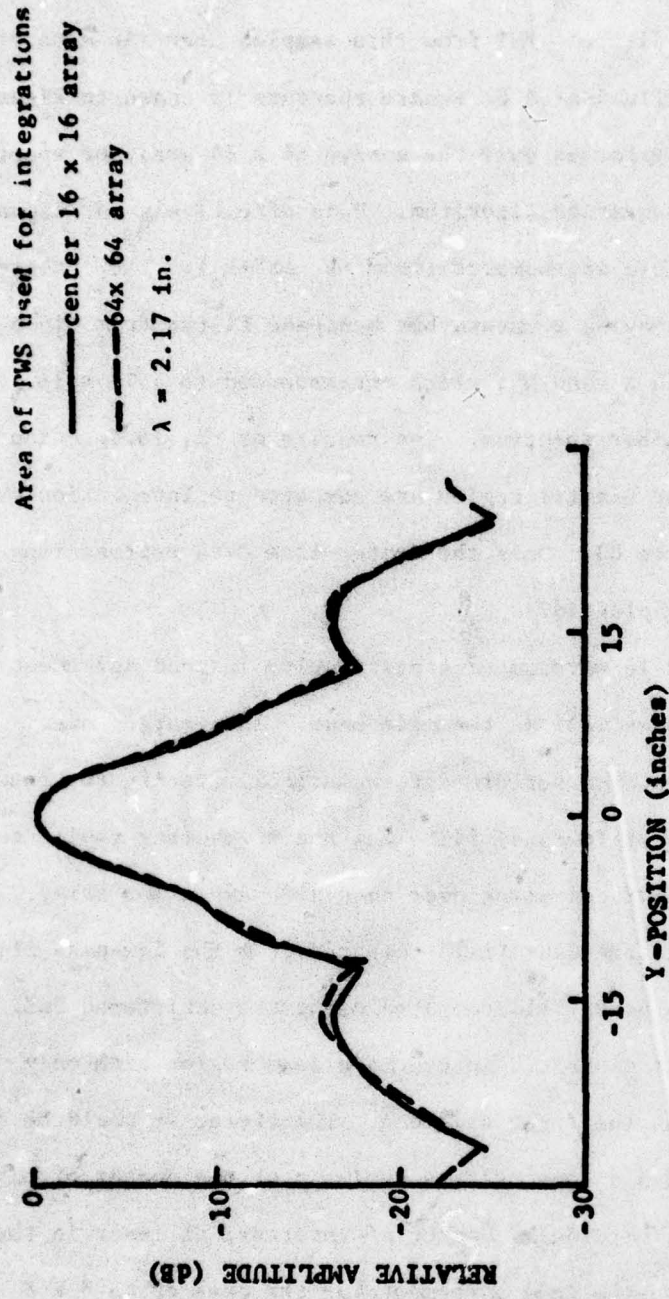


Figure 83. Comparison of the calculated near field of a uniformly illuminated 8-wavelength square aperture using a 16x16 low-pass filtered and a 64x64 unfiltered plane wave spectrum at a near field distance of 6.44 wavelengths.

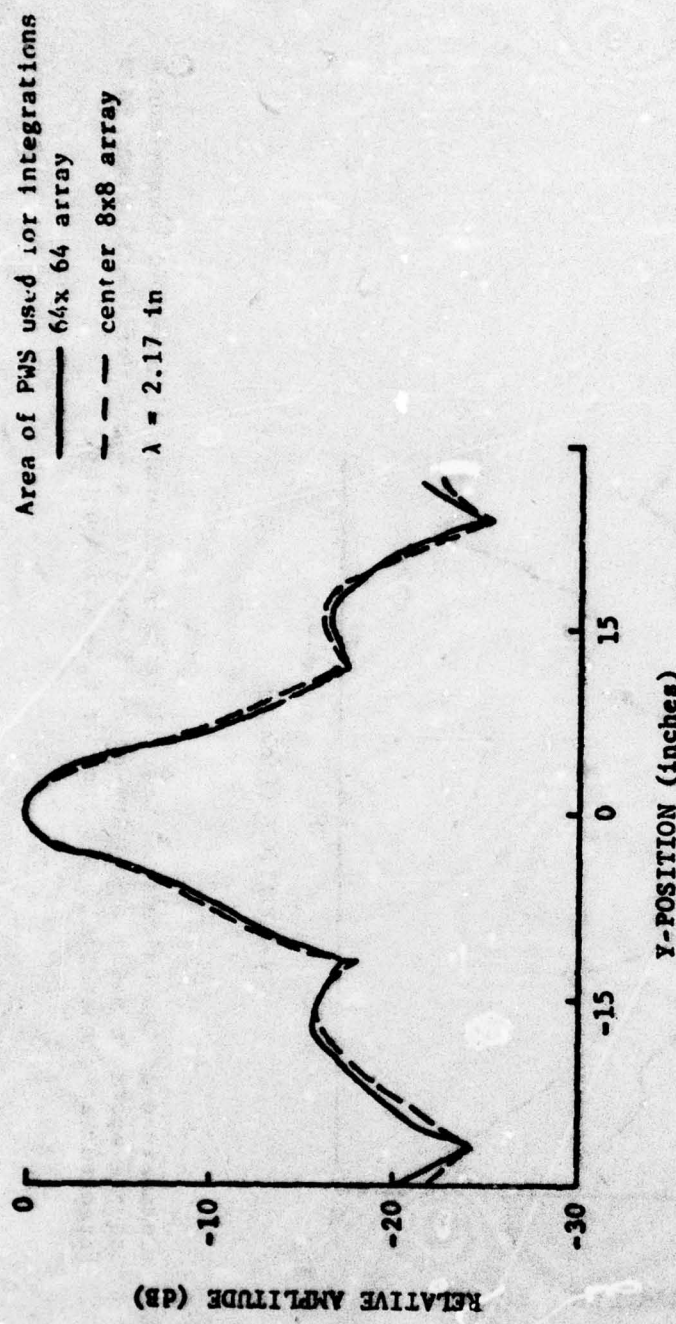


Figure 84. Comparison of the calculated near field of a uniformly illuminated 8-wavelength square aperture using a 8x8 low-pass filtered and a 64x64 unfiltered plane wave spectrum at a near field distance of 6.44 wavelengths.

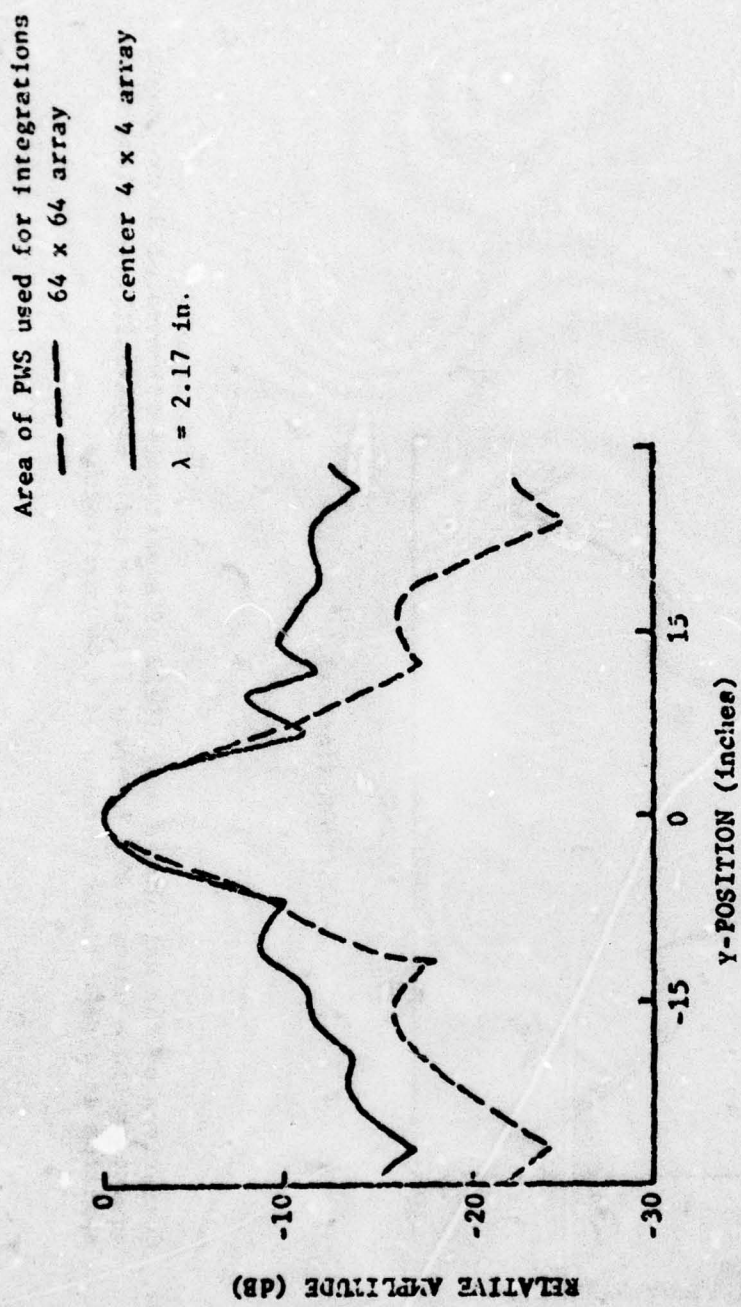


Figure 85. Comparison of the calculated near field of a uniformly illuminated 8-wavelength square aperture using a 4x4 low-pass filtered and a 64x64 unfiltered plane wave spectrum at a near field distance of 6.44 wavelengths.

over a 4×4 wavenumber array compared to integration over the unfiltered PWS. In this case, the size of the wavenumber limited region was not large enough to describe the main beam, but good agreement with the maximum amplitude was maintained. These results thus support earlier assertions concerning Equation 44. Figures 86 and 87 present similar results for a near-field distance of $0.05 D^2/\lambda$.

Because of the wavenumber limiting, if the region of interest happened to be in a region other than the center, bandpass filtering can be used to describe the significant field contributions in that region. Figure 88a indicates the spectral region used to calculate the field in the first sidelobe using a 16×16 wavenumber array ($.25 k_0$). The results of the wavenumber limiting in the sidelobe region are presented in Figure 89 for calculations along the center-line path indicated in Figure 88b. The good agreement of the results in the first sidelobe region indicate that the number of plane waves used to describe the near-field region of interest can be significantly reduced and still provide an accurate description of the field in that region. Figure 90 presents the results of integration over a $.125 k_0$ wavenumber bandwidth.

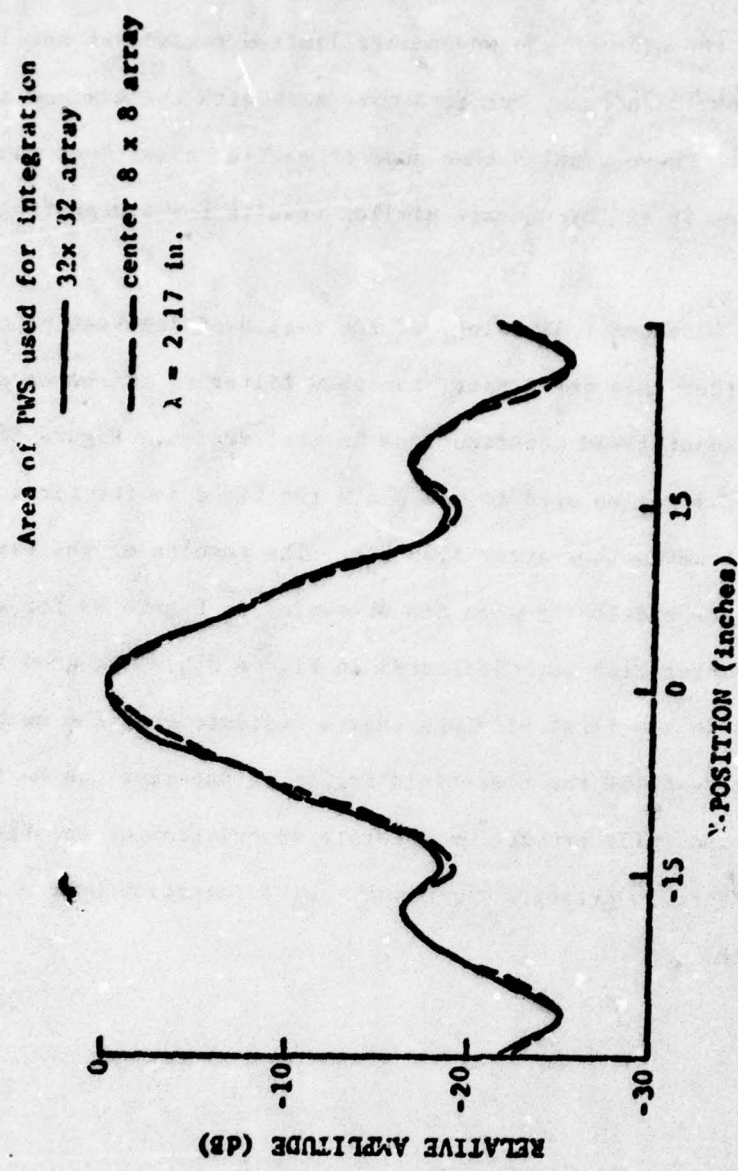


Figure 86. Comparison of the calculated near field of a uniformly illuminated δ -wavelength square square aperture using a 8x8 low-pass filtered and a 32x32 unfiltered plane wave spectrum at a near field distance of 3.22 wavelengths.

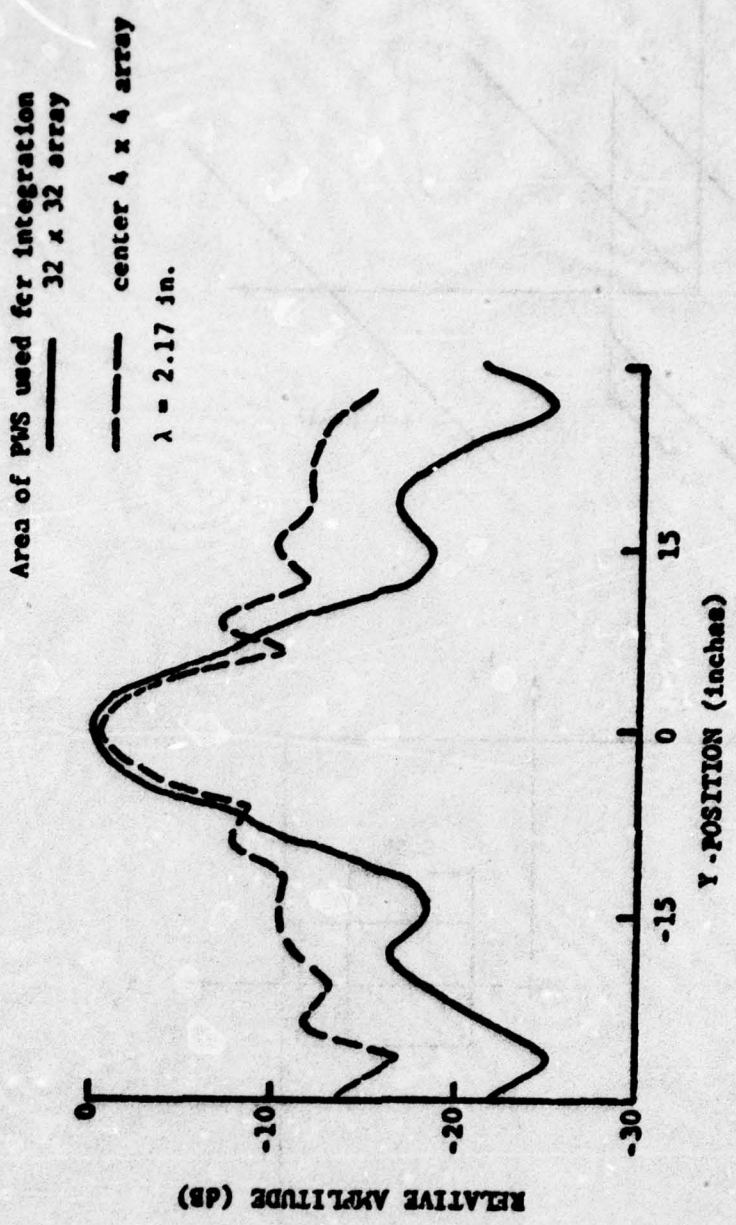


Figure 87. Comparison of the calculated near field of a uniformly illuminated 8-wavelength square aperture using a 4x4 low-pass filtered and a 32x32 unfiltered plane wave spectrum at a near field distance of 3.22 wavelengths.

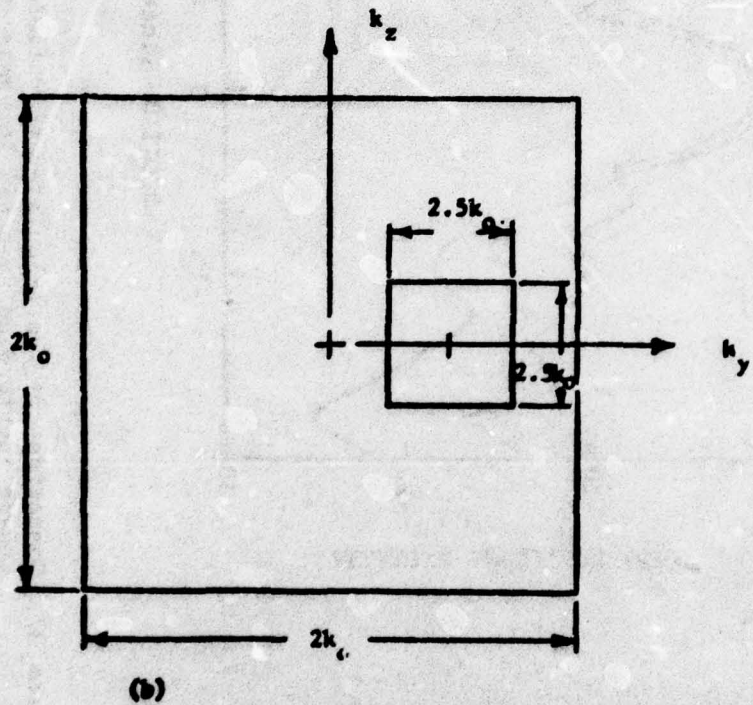
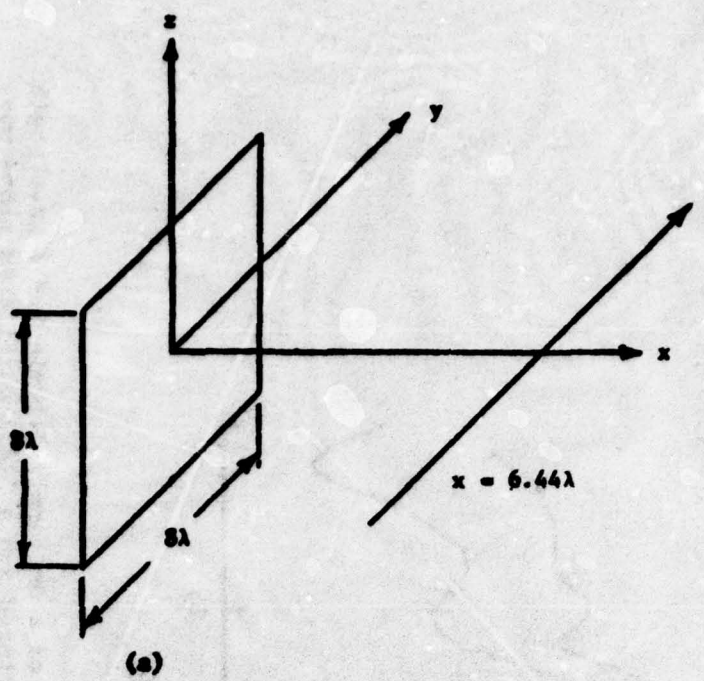


Figure 88. (a) Illustration of path used for near-field "flyby" calculations at a measurement distance of 6.44λ and
(b) Bandpass filtered wavenumber region of spectral data used for calculation of 1st sidelobe.

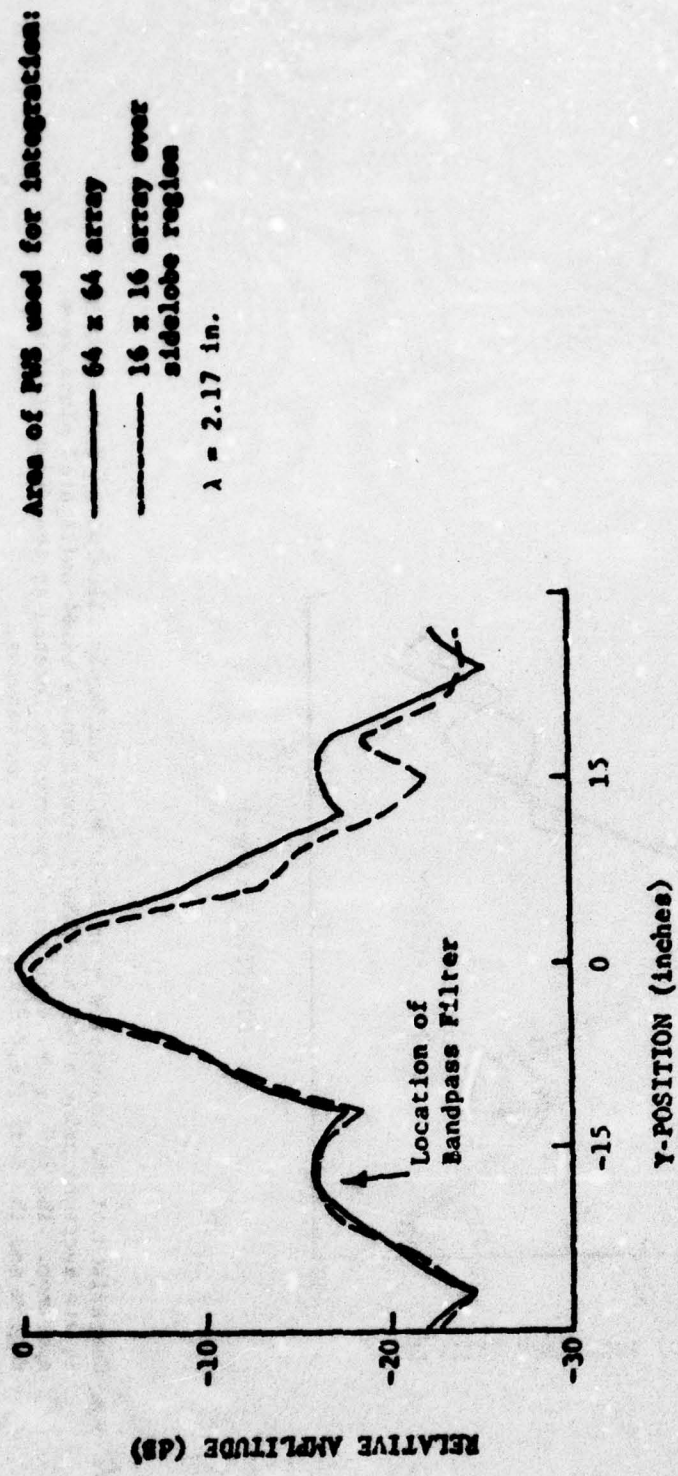


Figure 89. Comparison of the calculated near field of a uniformly illuminated 8-wavelength \times 8-wavelength square aperture using a 16x16 bandpass filtered and a 64x64 unfiltered plane wave spectrum. The 16x16 bandpass filtered spectrum is located at the first sidelobe region and the near field distance is 6.44 wavelengths.

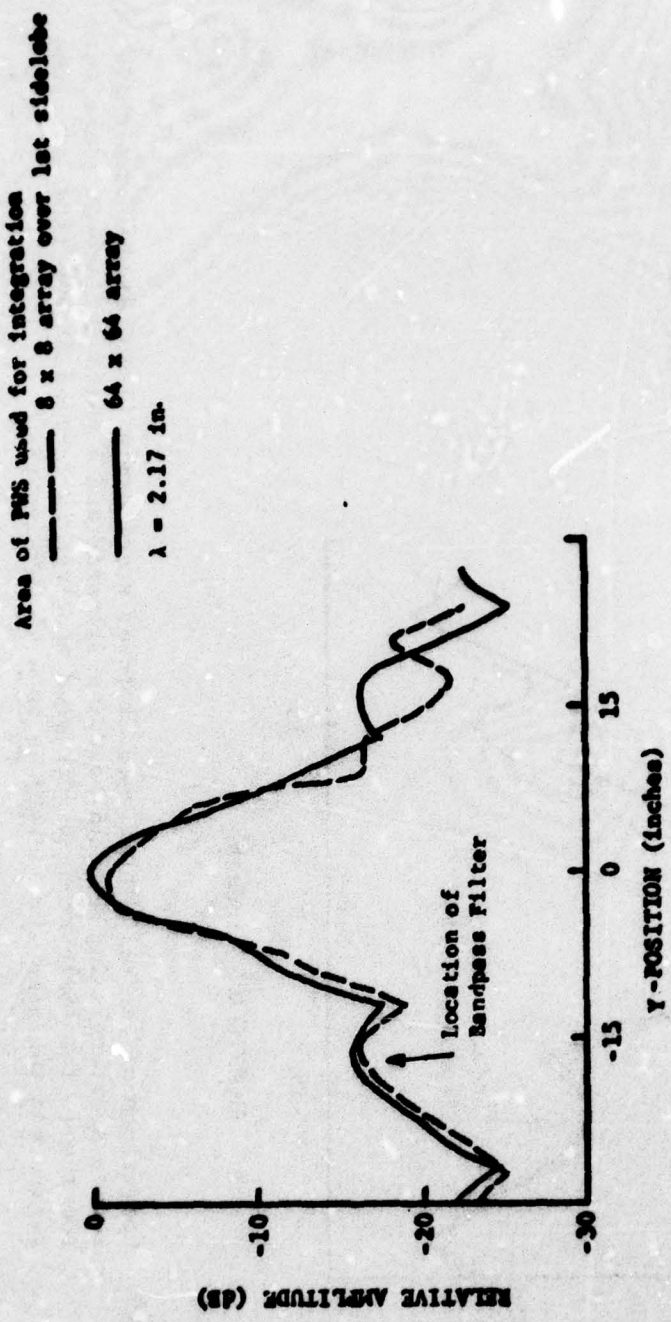


Figure 90. Comparison of the calculated near field of a uniformly illuminated 3-wavelength square aperture using a 8x8 bandpass filtered and a 64x64 unfiltered plane wave spectrum. The 8x8 bandpass filtered spectrum is located at the first sidelobe region and the near field distance is 6.44 wavelengths.

Figure 90.
Comparison of the calculated near field of a uniformly illuminated 3-wavelength square aperture using a 8x8 bandpass filtered and a 64x64 unfiltered plane wave spectrum. The 8x8 bandpass filtered spectrum is located at the first sidelobe region and the near field distance is 6.44 wavelengths.

REFERENCES

1. G. Borgiotti, "Fourier Transforms Method in Aperture Antennas Problems," Alta Frequenza, Vol. 32, pp. 809-816, November 1963.
2. E. B. Joy and D. T. Paris, "Spatial Sampling and Filtering in Near-Field Measurements," IEEE Transactions on Antennas and Propagation, Vol. AP-20, pp. 253-261, May 1972.
3. G. P. Rodriguez, E. B. Joy, G. K. Huddleston, C. P. Burns, E. C. Burdette, and J. Hanfling, "A Study of Phased Array Antennas Patterns Determined by Measurements on a Near-Field Range," Final Technical Report, Contract DAAH02-74-C-0367, MICOM, Project A-1588, March 1975, pp. 71-76.
4. R. F. Harrington, Time-Harmonic Electromagnetic Fields, McGraw Hill, New York, 1961, pp. 116-117.
5. R. E. Collin and F. J. Zucker, Antenna Theory, Part 1, McGraw Hill, New York, 1969, pp. 100-101.
6. J. D. Jackson, Classical Electrodynamics, John Wiley, New York, 1963, p. 47.
7. K. Levenberg, "A Method for the Solution of Certain Non-Linear Problems in Least Squares," Quarterly of Applied Mathematics, Vol. 2, pp. 164-168, 1944.
8. D. W. Marquardt, "An Algorithm for Least-Squares Estimation of Non-Linear Parameters," Journal of the Society for Industrial and Applied Mathematics, Vol. II, No. 2, June 1963.
9. J. L. Edwards, C. E. Ryan, Jr., W. M. Leach, Jr., and W. J. Storey, "Near-Zone Radar Cross-Section Technique Development," Georgia Institute of Technology, Technical Report AFAL-TR-74-227, November 1974.
10. M. I. Skolnik, Radar Handbook, McGraw-Hill, New York, 1970, Chapter 21.